Design and Fabrication of PZT-Actuated Silicon Suspensions for Hard Disk Drives

by

Tsung-Lin Chen

M.S., Tsing-Hua University (1992)
B.S., Tsing-Hua University (1990)

A dissertation submitted in partial satisfaction of the
requirements for the degree of
Doctor of Philosophy

in

Engineering — Mechanical Engineering

in the

GRADUATE DIVISION
of the
UNIVERSITY of CALIFORNIA at BERKELEY

Committee in charge:

Professor Roberto Horowitz, Chair
Professor Roger T. Howe
Professor Albert P. Pisano

Fall 2001

The dissertation of Tsung-Lin Chen is approved:

Chair Date

Date

Date

University of California at Berkeley

Fall 2001

Design and Fabrication of PZT-Actuated Silicon Suspensions for Hard Disk Drives

by

Tsung-Lin Chen

Abstract

Design and Fabrication of PZT-Actuated Silicon Suspensions for Hard Disk Drives

by

Tsung-Lin Chen

Doctor of Philosophy in Engineering — Mechanical Engineering

University of California at Berkeley

Professor Roberto Horowitz, Chair

Piezoelectrically actuated suspensions are currently being considered by the magnetic recording industry, as a means of achieving dual-stage actuation in magnetic Hard Disk Drives. In most designs, piezoelectric actuators are placed behind the suspension, and only the position-error-signal obtained from the magnetic head, is utilized as the feedback signal to construct the dual-stage servo. In general, this approach achieves a relatively low operating voltage for piezoelectric actuation and low frequency runout attenuation. However, it may be susceptible to instabilities due to the excitation of suspension resonance modes.

In this dissertation, a silicon suspension, suitable for use in a piezoelectrically actuated dual-stage servo system for magnetic Hard Disk Drives, has been designed, fabricated and tested. The new suspension design incorporates a piezoresistive sensor that measures the position of magnetic head relative to the voice coil motor. The availability of this position signal enables a more compliant suspension design and allows the piezoelectric actuators to be placed closer to the magnetic head. This arrangement not only achieves a similar driving voltage and runout attenuation to other piezoelectrically actuated suspensions but, in addition, it is able to measure and attenuate runout induced by suspension vibration.

An integrated-gimbal structure is another unique feature for this silicon suspension. This gimbal design features two adjacent flexures as the torsion bar, which differs from previous gimbal designs. This new torsion bar design successfully produces the necessary gimbal pitch and roll flexibility, while providing very high in-plane and out-of-plane bending stiffness in a very limited design parameter space. Other features of the silicon suspension design presented in this dissertation , which enable piezoelectric actuation, include: a stretch area, a leverage mechanism and electrical interconnects. All these features were implemented on a single piece of single crystal silicon.

A simple and reliable SOI-like process has been developed to fabricate this new silicon suspension. The most challenging aspect of this process is the lithography that takes place after the deep-reactive-ion-etch (DRIE). By fabricating the proposed silicon suspension, we demonstrated that this newly developed process is capable of making structures with an aspect-ratio of 20 and 3 μm lithography precision on the topography of post DRIE.

A fabricated silicon suspension was tested on a rotating disk. The experimental results indicate that this silicon suspension has a dynamic performance that is compatible with current metal suspensions found in the commercial products.

Professor Roberto Horowitz
Dissertation Committee Chair

To my family, uncle Eugene and Andrew Tam

Contents

List of Figures

List of Tables

Chapter 1

Introduction

The magnetic data storage industry so far has relied on the notion that mechanically scanned magnetic media can be used to store data at a higher density and lower cost than competing technologies. In the past decade, solid-state technologies experienced tremendous advances, and as a consequence the solid-state memory industry was able to double areal density every 3 years, and recently even every 2 years. To stay competitive, the magnetic recording storage industry has had to advance its technologies at a even higher rate, in order to stay ahead in terms of higher areal density and lower cost.

The most used magnetic data storage device in a computer system, and the apparatus that has experienced the most technological development is the hard disk drive (HDD). In HDDs, data is stored on concentric data tracks in rotating disks and is read by a radially-traversing, mechanically positioned magnetic head. The continued increase in areal data storage density depends on the feasibility of continuing the miniaturization of data bits and the precise positioning of magnetic heads. During the past years, the HDD industry has been able to increase the areal storage density at an average of 60% per year, and this trend has been accelerated to approximate 100% per year during the last 18 months. This astonishing results were achieved largely through component miniaturization, without altering much the conventional HDD configuration. However, it is generally believed that, in order to maintain this growth rate, some fundamental configurations may have to change [15]. In the past six years, the use of dual-stage servos in HDDs has attracted significant attention and has been deemed to be one of the most promising technologies to achieve higher data track densities. The key idea of constructing a dual-stage servo mechanism is to mount a small piggy back actuator, capable of positioning the magnetic head with great accuracy and speed, on a voice-coil-motor.

The field of micro-electromechanical systems (MEMS) is growing rapidly. Micromechanical structures are currently being investigated for a wide variety of applications because they are generally several orders of magnitude smaller than their conventional counterparts and can easily be integrated with electronic circuits. Moreover, current deep reactive ion etch (DRIE) processes are able to achieve high aspect ratio ($>$ 25:1) silicon mechanical structures, which can hardly be achieved by conventional machining techniques. These high precision fabrication techniques present the possibilities of achieving high performance and multiple functionality in mechanical structures, with low fabrication cost. Thus, MEMS is considered to be among the most promising technologies, to keep up or even accelerate the miniaturization trend in the HDD industry.

The main focus of this dissertation is to design and construct a novel instrumented and actuated silicon suspension with an integrated gimbal structure, which can serve as a piggy back actuator in a HDD dual-stage servo system. Thanks to MEMS fabrication techniques, many key features in a dual-stage servo mechanism can be integrated into such a one-piece silicon suspension.

1.1 Basic Hard Disk Drive Mechanics

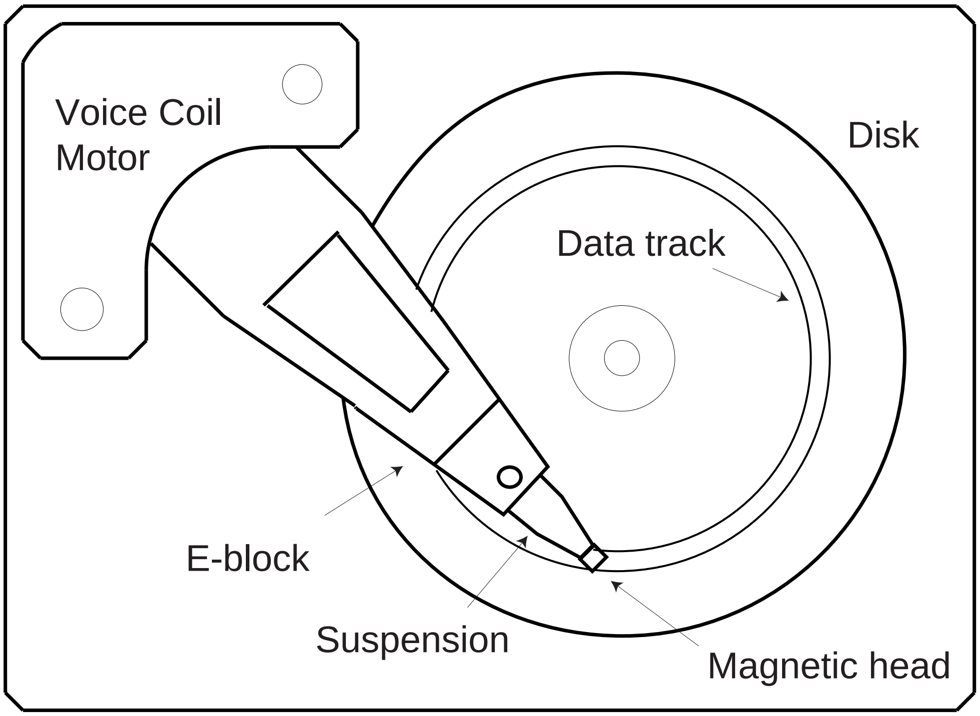

Figure 1.1: The schematic of a conventional hard disk drive

Fig. 1.1 shows the schematic of a conventional HDD. The magnetic heads consist of a thin-film inductive head and a magnetoresistive (MR) head; and are embedded in a ceramic block named ”slider” which flies on top of a rotating disk. The slider air bearing surface (ABS), the surface which faces the media disk, has special aerodynamic patterns on it. These patterns maneuver the air flow, generated by the rotating disk, resulting in the air-bearing effect. With the assistance of the air-bearing, which is created between the slider surface and disk, the slider slides smoothly several nano-meters above the rotating disk. The voice-coil-motor (VCM) positions the slider in the radial direction of the disk to access data bits which are stored on concentric data tracks on the disk. When the slider is positioned at the target location, the inductive head performs the "write" action to record data on the disk and/or the MR head reads out the data from the disk. The whole arm assembly, including E-block, suspension and slider, rotates around a bearing which is fixed to the case of a HDD.

1.2 Data Storage Density

Typically, data bits are arranged in almost concentric radial tracks, as shown in Fig. 1.1. The storage capacity of a HDD is measured by the data bit areal density, Maximum-Areal-Density (MAD), which is the multiplication of the "track density" in the radial direction, measured in numbers of tracks per inch (TPI), and "linear density", which is the bit density in the tangential direction, measured in number of bits per inch (BPI). To date, commercially available products have an areal storage density of 20 Gbit/in ^{2}, and are expected to reach 100 Gbit/in ^{2} in the next $2-3$ years. Meanwhile, research work has begun to explore the possibility of achieving a one-Terra bit per inch square areal density. Table 1.1 shows the approximate data density of some typical commercial products of recent years, as well as the projected data density for the next few years. The prediction was made on the assumption of a continuing 60% annual areal density growth rate.

In the recent years, the MAD growth rate was mainly due to the increase in linear density, without much increase in track density. Thus, the radial to linear dimensions aspect ratio of a data bit has continued to slenderized. As we move towards to the next generation of HDD (100 Gbit/in ^{2}), continuing on the old scaling rules (ie. increasing BPI rather than TPI) would result in a areal data bit that would be too small to retain its magnetization in light of thermal decay [15]. Studies estimate that if the aspect ratio of a data bit can be reduced to 4:1, it is possible to achieve 100 Gbit/in ^{2} while maintaining the current storage lifetime [34]. This leads to a linear bit density of 672K BPI and a radial track density of 168K TPI for the specification of 100 Gbit/in ^{2}.

	MAD	TPI	BPI	Bit Aspect Ratio
1971	1	200	5,000	25
1981	10	800	12,500	15.6
1991	100	2,000	50,000	25
1995	600	5,000	120,000	24
2001	20,000	40,000	500,000	12.5
2004	100,000	168,000	672,000	4

Table 1.1: HDDs data density. MAD is measured in Mbits/in^2

1.3 Suspension Assembly

Fig. 1.2 shows the schematic diagram of a conventional HDD suspension assembly. The suspension assembly consists of a suspension, flexure/ gimbal and slider/ magnetic heads. In general, the suspension is designed to be soft in the vertical direction (its resonance frequency is around 200 Hz) and as rigid as possible in the in-plane direction. The compliance in the vertical direction enables the slider to follow the air bearing terrain on the rotating disk; while the rigidity in the in-plane direction reduces the off-track error in the HDD servo operation. It is difficult to design a suspension that achieves both stiffness requirements simultaneously. Therefore, the suspension design indeed is a compromise

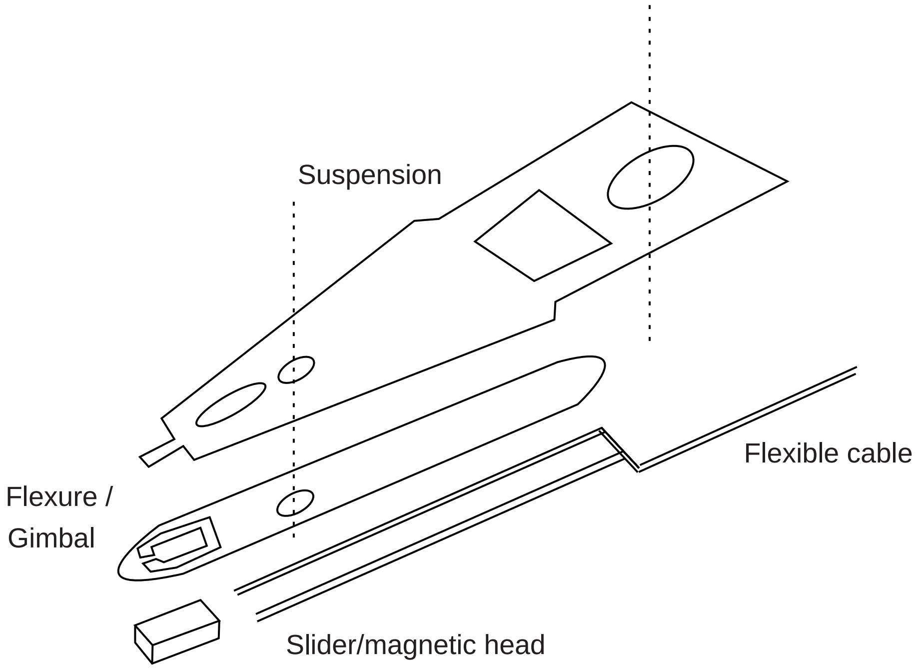

Figure 1.2: The schematic of a HDD suspension

between compliance in the z-direction versus rigidity in the in-plane direction. Moreover, because the suspension in-plane stiffness can not be arbitrary increased as may be required, the suspension resonances in the in-plane direction become the most significant factor that limits servo performance.

1.3.1 Gimbal structure

The gimbal structure is located at the tip of the suspension and holds the slider in its center coupon. The requirements for the dynamic characteristics of gimbal structures are that they be flexible in the pitch and roll motion but stiff in in-plane and out-of-plane bending motion. The compliance of the roll and pitch motion, in conjunction with the vertical compliance provided by the suspension, allows the slider to follow the air bearing terrain without crashing into the disk. The rigidity of in-plane bending reduces the tracking error of the servo positioning system by the same rationale as for the suspension in-plane stiffness. The rigidity of out-of-plane bending prevents the slider from deflecting away should it hit on bumps of the disk topography, obstructing the vertical compliance set by the suspension. It is not easy to meet all these requirements using only one piece of metal. For this reason, most commercially available suspension/gimbal designs consist of 2 – 3 pieces of steel, each with different thickness, as shown in Fig. 1.2.

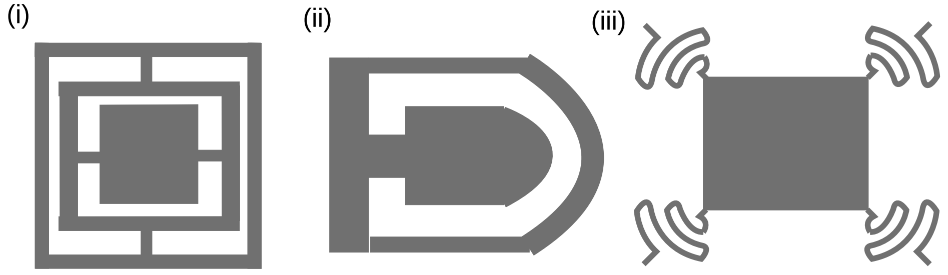

Figure 1.3: The schematic of gimbal structures. (I) Orthogonal sets of torsion bar. (II) One torsion bar with dimple structure (III) Serpentine gimbal torsion bars

Fig. 1.3 shows three types of gimbal design. The first two designs were widely adopted in the commercial HDDs during different periods of time. The older gimbal design (design (I)) utilized orthogonal sets of torsion bars. The advantage of this design is its high out-of-plane bending stiffness [38]. The second design utilizes a single torsion bar and a pivot point provided by the suspension (dimple structure) to match the performance requirements. The rotation of the single torsion bar initiates the roll motion for the slider; and the bending motion of the torsion bar initiates the pitch motion. Typically, the flexure/gimbal structure is fabricated on a thin steel piece (~ 25 μm), in order to have high in-plane bending stiffness, while maintaining the necessary torsional motion compliance. The dimple structure from the suspension provides a path, bypassing the torsion bar, to transfer the vertical direction force from the slider back to the suspension. The second design is currently being used in the majority of commercial products. The third design, shown in Fig. 1.3, is made of single crystal silicon instead of steel as in the previous two designs. Although the pitch and roll motion stiffness of this design are in the range of the requirements, this complicated design suffers for multiple coupled resonances [38].

1.3.2 Electrical interconnects

After the slider is placed at the center coupon of the gimbal structure, wires are attached to the magnetic heads to transfer data. It is a well known fact that these wires interfered with the slider flying stability and suspension resonance. Ever since the MR heads were introduced to HDDs and became the standard head assembly, the number of wires doubled from 2 to 4 and the electrical interconnects became an important issue again, due to the fact that extra wires result in an unbalanced slider flight. To improve slider flying stability, two types of ”wireless suspension” have been proposed [48]: (1) Flexible cable: cable is glued to the suspension (example, TSA series from Hutchinson Technology Inc). (2) In-situ metal leads: metal is deposited and patterned on the suspension (example, pico-CAPS Cable Patterned Suspension from Fujisu Ltd) [48] [47]. These two approaches have their own advantages and disadvantages and are difficult to compare. However, as the size of suspensions decreases, it becomes more difficult to handle and attach a flexible cable to the suspension at an exact location, as required in the first approach mentioned above.

1.4 Dual-stage Servo System

As pointed out in section 1.2, that the tack density TPI has to be increased to effectively enlarge the MAD factor. The immediate challenge is how to attain an acceptable reduction in track misregistration (TMR)[12][15][31]. TMR is the deviation between the magnetic head position and the center of the data track. Based on the HDD industry servo practices, the acceptable 3–σ TMR is approximate 12 % of the track-to-track pitch. Unfortunately, the disturbances that cause TMR do not all scale down with track pitch. Therefore, the effect of disturbances that affect the servo loop become percentage-wise more important as track pitch decreases. Since the source of TMR does not diminish, the reduction of TMR has to be enforced by a better tracking servo system.

From the servo system viewpoint, the attenuation provided by the servo loop at the low frequency range is a strong function of the servo bandwidth. Based on this assertion and without changing the positioning servo configuration, one needs to use a "high-gain" servo system, by feeding more power to the VCM, in order to increase the open-loop gain crossover frequency. However, VCM resonances, multiple resonances in the suspension, friction from the bearing and other factors, limit the servo bandwidth that can be attained by this strategy. Studies has shown that attaining a 50 K TPI and beyond will require major enhancements in the servo system [15]. The most promising solution to this challenge is to incorporate dual-stage actuation to the current servo system. By having a smaller mass to move and by being capable to bypass some of the resonances and hysteresis inherent from the conventional VCM, the secondary actuator is thus capable of providing more servo bandwidth.

1.4.1 Secondary actuation

Much research work has been dedicated to the exploration of suitable secondary actuators for constructing dual-stage servo systems for HDDs in the past six years. Different types of secondary actuation force, as well as dual-stage configurations, have been proposed. These dual-stage configurations can be categorized into three groups.

Actuated suspension: In this approach, the suspension is re-designed to accommodate an active component, typically a piezoelectric material. This piezoelectric material stretches the suspension to position the slider/magnetic heads. Piezoelectric material is known to be an active actuation element that produces a large actuation force but small actuation stroke. Therefore, in the "actuated-suspension " configuration, the piezoelectric actuators usually are implemented in conjunction with a leverage mechanism that can convert small actuation displacements into large effective head displacements. Typically, the piezoelectric actuators are placed away from the magnetic heads (between the E-block and suspension) so that they can have a long leverage arm to produce a sufficient amount of the magnetic-head motion. The advantage of this approach is that the suspension can be fabricated by a conventional suspension-making process, and its dual-stage servo configuration is effective in attaining low frequency runout attenuation in the positioning servo loop. The major drawback of this approach is that the system is still susceptible to instabilities due to the excitation of suspension resonance modes. Thus, TPI servo performance can be increased, but remains limited, when compared to the next two approaches. However, this approach is expected to be the first to be deployed in commercial HDDs.

Actuated slider: In this approach, a microactuator is placed between the slider and gimbal to position the slider/magnetic heads. The resulting servo bandwidth of this approach can be higher than the previous approach because the secondary actuation bypasses the mechanical resonances of the suspension. This approach uses existing sliders and microactuators that can both be batch fabricated, and thus could be cost effective. The size and mass of the microactuator is almost the same as the current slider and may interfere with the slider flying stability. Therefore, current suspensions need to be re-designed to adopt this secondary actuator. Suitable driving forces in this approach include electrostatic, electromagnetic and piezoelectric [14] [38] [27] [12]. To further reduce the assembly task of placing the microactuator in between gimbal structure and slider, some researcher have proposed microactuators that are either integrated with the gimbal structure [38] or the slider [20].

Actuated head: In this approach, the slider is re-designed so that the microactuators can be placed inside the slider block and actuate the magnetic heads with respect to the rest of the slider body. As this type of microactuators are very small, they only slightly increase the slider weight, and are thus capable of working with the current suspension assembly. Researchers have successfully demonstrated the integrated fabrication process for fabricating the electrostatic microactuators and magnetic heads within one piece of ceramic block (slider). The embedded electrostatic microactuator has its resonance close to 30 KHz and was able to position the magnetic heads relative to the rest of the slider body by 0.5 μm [19] [40].

1.4.2 Relative position error signal

Most of the proposed dual-stage servo controllers utilize only the position of the magnetic head relative to the center of data track, known in the industry as the PES, for close-loop track following control. These systems have a single-input-multi-output (SIMO) control architecture. However, in some instances, it is also possible to measure the relative position error signal (RPES) of the magnetic head relative to the VCM. In this case, the control architecture is multi-input-multi-output (MIMO). As shown in [31], the RPES can be used in a MIMO controller to damp out the second stage actuator's resonance mode and enhance the overall robustness of the servo system.

Among the three types of secondary-actuation configurations discussed above, the Actuated-suspensions usually do not have a sensing mechanism for the RPES signal, while electrostatic microactuators utilize the variation in capacitance to obtain the RPES signal for dual-stage servo configuration.

1.5 PZT Actuators

Piezoelectricity refers to the phenomenon in which forces applied to a segment of material result in the appearance of electron charges on the surfaces of that segment. If the surfaces/electrodes of the segment are not short-circuited, a electric field across two surfaces appears and so does the voltage associated with the electric field. This mechanical–electrical property also applies in the reversed way. When the piezoelectric material is stressed electrically by a voltage, its dimensions change. A piezoelectric material is capable of acting as either a sensing or active actuation element, or both.

The following equation describes the relations between forces, electric field and material deformation for a piezoelectric material.

$$\delta E = \frac{1}{d}(\frac{-1}{c}\delta T + S)$$

where E denotes the electric field, d the piezoelectric constant, c the Young's modulus, T the stress and S the strain.

It is useful to remember that a large "d constant" implies a large mechanical deformation under the same applied electric field/voltage, which is usually sought for in active actuation devices. In the equation above, subscripts on the material properties can be seen frequently to further identify the directions of the input excitation and material responses. For example d_{ij} implies that the electric field is applied along the "i" direction and the output strain is along the "j" direction.

Lead zirconate titanate (PZT) ceramics are the most popular piezoelectric actuators mainly because of their large piezoelectric constants. When used in actuators, the performance of the PZT depends on its material properties as well as the way in which it is stretched. Typically, PZT actuators are arranged so that they are stretched in either the axial motion or bending motion. PZT actuator performance in each motion is listed in Table 1.2 for comparison.

Most HDD actuated suspension dual-stage servo system designs utilized the d_{31} properties of "single-layer" PZT, to actuate the suspension assembly [45] [1] [36] [10]. In these designs, a high voltage is applied to the PZT actuators ($\sim$ 40 Volts) to produce sufficient magnetic-head displacement ($\sim 1\ \mu$m), even though normally the PZT stroke is enlarged 10 times by an associated leverage mechanism to move the head. The high applying voltage requires costly circuitry and raises safety concerns in HDDs. One alternative is to replace single-layer PZT with multiple-layers PZT. Researches have reported that in a multiple layer PZT actuator, the actuation voltage can be drop to 5 V to produce the same amount of head displacement as with a single-layer PZT [41] [72]. The major drawback of multiple-layers PZT is its costly fabrication process and the nonlinearity associated with its material properties.

	Axial motion	Bending motion
Strain	$10^{-4} \sim 10^{-2}$	
Hysteresis	Large, depends on the material	
Aging(life cycle)	10^{11}	10^{8}
Response	10 μ sec	1 m sec
Critical Electrical Field	10^{6} V/m	

Table 1.2: PZT actuators characteristics

1.6 MEMS Technology in HDDs

1.6.1 Silicon suspension

As mentioned before, components miniaturization has been an important technology trend in the HDD industry. The demands on mechanics miniaturization come from both small/portable HDDs development (for example, a one inch diameter HDD) and the necessity of high stiffness-to-mass ratio mechanical components for improving servo bandwidth. As the matter of fact, the increase of servo bandwidth in HDDs in recent years has largely been due to new compact suspension design [15].

Conventional suspensions are fabricated by chemical etching and steel stamping processes on the stainless steel piece with uniform thickness. In this fabrication process, not only the dimension accuracy is vague due to the steel stamping process; but also the plastic deformation can easily occur during the suspension and flexure/gimbal assembly [42].

The use of silicon gimbals and silicon suspensions has been proposed mainly for the capability of MEMS fabrication technologies to achieve a significant dimensional scaling down of the suspension components. Typically, one thinks of silicon as a brittle material and would not normally use it to construct flexible structures. However, brittle materials are also elastic, and the difference between the brittle material and ductile material is that the brittle material fractures when the stress reaches the ultimate strength, while the ductile material yields. It is a well known fact that the ultimate strength of silicon microstructures (7 GPa) is much higher than the steel yielding strength (0.25 GPa), making its use possible as a structure material in HDD suspensions.

There are several advantages offered by silicon suspensions. (1) In the case that defective suspensions occurred during the fabrication and/or assembly process, silicon suspensions would break instead of yielding to the plastic deformation. This allows the assembler to discard the defective suspensions before the suspensions are loaded into a HDD. (2) Thanks to the fact that precise and high-aspect-ratio structures can be fabricated by advanced silicon fabrication technology, less design–fabrication constraints must be imposed and thus more compact suspension designs are feasible. With the advantages gained from these enhanced fabrication capability, instead of implementing the suspension/gimbal assembly on two pieces of steel, Miu and Narbutovskih proposed a one-piece silicon suspension/gimbal for miniaturized HDDs [42] [35]. (3) It is relatively easy to add electrical functionalities to silicon suspensions. These functionalities could potentially improve HDD performance dramatically. The functionality that have been explored include in-situ electrical interconnects (as discussed before), vibration sensors (in next sections), the use of an in-situ pre-amplifier on the suspension [57], etc.

1.6.2 Piezoresistive sensors

Piezoresistive film has been widely used in the variety of applications, including pressure sensors and vibration sensors. Generally speaking, piezoresistive sensing techniques require less complicated sensing circuitry and perform better in a severe environment as compared to other sensing techniques. When a piezoresistive film is subjected to stress, the film dimensions change as well as the film resistivity. The fractional change of resistance is proportional to the deformation of the piezoresistive film. For a small change of resistance, this relation can be expressed as,

$$\frac{\Delta R}{R} = K \cdot \epsilon \tag{1.1}$$

where R is resistance, K is gauge factor and ϵ is strain.

As shown in the equation, a material with higher gauge factor produces larger resistance variation under the same amount of deformation, and is thus more sensitive to the deformation. Many materials have the piezoresistivity property, however only the materials that have a large gauge-factor are considered in the stain-sensing applications. For example, the gauge factor of steel is 2, while that of single crystal silicon is around 100 and polysilicon is around 30.

Piezoresistive film fabrication using single-crystal-silicon or polysilicon has been a standard process in MEMS technology. As mentioned before, the RPES availability significantly enhances the robustness of the servo system. Thus, it is promising to use MEMS fabrication techniques to attain an RPES signal to improve HDD performance.

Although the gauge factor of single-crystal-silicon is about 10 times higher than of polysilicon [13], the piezoresistive single-crystal-silicon film needs to be electrically isolated from the rest of the silicon structure [13]. As a consequence, it is more difficult to incorporate it to the silicon-suspension fabrication process. In this project, the boron doped polysilicon film was utilized in a piezoresistive sensor for obtaining the RPES.

1.7 Outline of this thesis

This thesis deals with the design, fabrication and testing of a piezoelectrically actuated silicon suspension. The features of this suspension include: integrated silicon gimbal structure, piezoresistive RPES sensors and motion components for enabling PZT actuation and in-situ electrical interconnects. All these features were implemented on a one-piece of silicon suspension. The following chapters address the details of our proposed silicon suspension design.

In Chapter 2, general formulas for calculating bending and torsion stiffness of a rectangular bar are discussed. At the end of this chapter, a new equation is developed that can precisely predict the torsional stiffness of a rectangular bar with a non-warping end plane. These equations were used in the design of the integrated gimbal structure in Chapter 3 and other lever arm structures through this dissertation.

In Chapter 3, we discuss all of the important features of the proposed silicon suspension. Design considerations and strategies are discussed in detail. Simulation results are presented which demonstrate the feasibility of the proposed design.

In Chapter 4, we discuss the techniques that were utilized to fabricate the silicon suspension described in this dissertation. In particular, a new fabrication process is developed to fabricate three dimensional structures without the use of costly SOI (Silicon-On-Insulator) wafers, as well as a new planarization technique to perform post-DRIE lithography.

In Chapter 5, we detail the experiments that were performed to test on the fabricated silicon suspension. Experimental data and a discussion of important results are included.

Conclusions and recommendations for future work are presented in Chapter 6.

Chapter 2

Linear Beam Deflection

This chapter sets forth some general formulas for calculating the bending and torsion stiffnesses of a rectangular bar. These equations will be used to design the gimbal torsional bars in the one-piece silicon suspension which is subsequently designed in Chapter 3. For the bending stiffness, the case of interest is usually referred as "fixed-guided bending" and the corresponding expressions can be found in various textbooks. For the torsion stiffness, the case of interest is the torsional motion of a rectangular bar with no warping at its end plane. The expressions found in textbooks are not applicable to this case. Therefore, it was necessary to develop an easily-applied expression for the torsional deflection of a beam with no warping at the end plane.

2.1 Fixed-guided Bending

With regard to the bending stiffness, we consider the example of the rectangular beam shown in Fig. 2.1. When an external force acts on the beam, the beam will deform in a way such that its curvature gradient at the two ends is equal to zero. This motion is

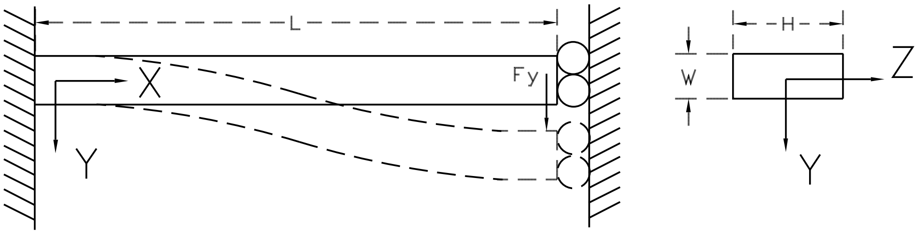

Figure 2.1: Fixed-guided beam subjects to a point load in y direction

often referred to as "fixed-guided bending" and usually takes place in structures that are symmetric. Various textbooks and references (e.g., [14][60]) give equations for calculating the bending stiffness in the y-direction and z-direction.

For the bending stiffness in the y-direction, k_y, the expression is

$$\frac{1}{k_y} = \frac{1}{k_{yb}} + \frac{1}{k_{ys}} \tag{2.1a}$$

where $\mathrm{k_{yb}}$ and $\mathrm{k_{ys}}$ represent the stiffness contribution from bending and shear stress, respectively.

$$k_{yb} = \frac{12EI_z}{l^3} \tag{2.1b}$$

$$k_{ys} = \frac{2Ghw}{3l} \tag{2.1c}$$

$$I_z = \frac{hw^3}{12} \tag{2.1d}$$

where

E	Young's modulus
G	Shear modulus
I_z	Moment of inertia about the z-axis
I_y	Moment of inertia about the y-axis
l	Beam length
w	Beam width
h	Beam height

An analogous result can be derived for the out-of-plane bending stiffness (z-direction) k_z,

$$\frac{1}{k_z} = \frac{1}{k_{zb}} + \frac{1}{k_{zs}} \tag{2.2a}$$

$$k_{zb} = \frac{12EI_y}{l^3} \tag{2.2b}$$

$$k_{zs} = \frac{2Ghw}{3l} \tag{2.2c}$$

$$I_y = \frac{h^3 w}{12} \tag{2.2d}$$

The expressions for the bending stiffness above were derived assuming that the bending beam undergoes no axial deflection. This assumption is valid only when the vertical deflection of the beam is less than 10% of its length.

2.2 Torsional Stiffness of a Rectangular Bar

This section presents expressions for predicting the torsional stiffness of a rectangular bar. The particular case that we are interested in analyzing is that in which, due to some constraint applied to the end plane, the end plane rotates but does not warp. This type of deformation often takes place in an object that has mirrored configuration and boundary conditions. Equations for the torsional stiffness of a twisted rectangular bar can be found in many textbooks and references (e.g., [59] [60] [71]). Most of these expressions presume that either the rectangular bar has a narrow cross section or that the plane at the free end is warping, and thus are not applicable to our design.

In this chapter, we will derive a new formula that can predict the torsional stiffness of a rectangular bar that has arbitrary cross section aspect ratio and no warping at the end plane. The derivation is an extension of Timoshenko's work on torsional stiffness of a narrow-cross-section rectangular bar [59] [60].

The first part of this section sets forth the theorems for deriving the torsional stiffness of an object in three dimensions. The second part of this section treats a rectangular bar subject to torsional motion and its end plane is warping. The materials presented in these two sections can mostly be found in the textbook by Timoshenko [59]. The third part of this section is our derivation for the case of a non-warping end plane.

2.2.1 Elasticity in three dimensions

Compatibility Conditions: To describe the deformation of a three dimensional object, three displacements, along the three orthogonal directions, are necessary and sufficient. Based on the object's deformation, six strain components (three normal strains and three shear strains) are defined to re-formulate the three dimensional deformation problem into a stress–strain problem. Since the six strain components are defined based on three displacement components, these strain components can not be independent; furthermore, three mathematic relations among them can be found. These three equations are the

"Compatibility Conditions" and are listed below.

$$\begin{aligned}\frac{\partial^2\epsilon_x}{\partial y^2}+\frac{\partial^2\epsilon_y}{\partial x^2} &= \frac{\partial^2\gamma_{xy}}{\partial x\partial y}\\ \frac{\partial^2\epsilon_y}{\partial z^2}+\frac{\partial^2\epsilon_x}{\partial y^2} &= \frac{\partial^2\gamma_{yz}}{\partial y\partial z}\\ \frac{\partial^2\epsilon_z}{\partial x^2}+\frac{\partial^2\epsilon_x}{\partial z^2} &= \frac{\partial^2\gamma_{xz}}{\partial x\partial z}\end{aligned} \tag{2.3}$$

where, ϵ_x, ϵ_y, ϵ_z are the three normal strains and γ_{xy}, γ_{yz}, γ_{xy} are the three shear strains.

Hook's Law: "Hook's Law" describes the linear relations between stress and strain components. According to "Hook's Law", the normal strain subjected to the normal force (for example, σ_x), up to the proportional limit, is given by the following equation.

$$\epsilon_x = \frac{\sigma_x}{E}$$

Furthermore, the deformation (e.g., elongation) of the object in one direction (x-direction) results in the contrary deformation (e.g., contraction) in the other two directions (y-direction and z-direction). The relation of the normal stress and two lateral strain components can be described as

$$\epsilon_y = -\nu\frac{\sigma_x}{E} \qquad \epsilon_z = -\nu\frac{\sigma_x}{E}$$

where, ν is a constant and named "Poisson's ratio". In the case that the object is simultaneously subjected to the normal stresses $\sigma_x, \sigma_y, \sigma_z$, we have the following equations.

$$\begin{aligned}\epsilon_x &= \frac{1}{E}(\sigma_x-\nu(\sigma_y+\sigma_z))\\ \epsilon_y &= \frac{1}{E}(\sigma_y-\nu(\sigma_x+\sigma_z))\\ \epsilon_z &= \frac{1}{E}(\sigma_z-\nu(\sigma_x+\sigma_y))\end{aligned} \tag{2.4}$$

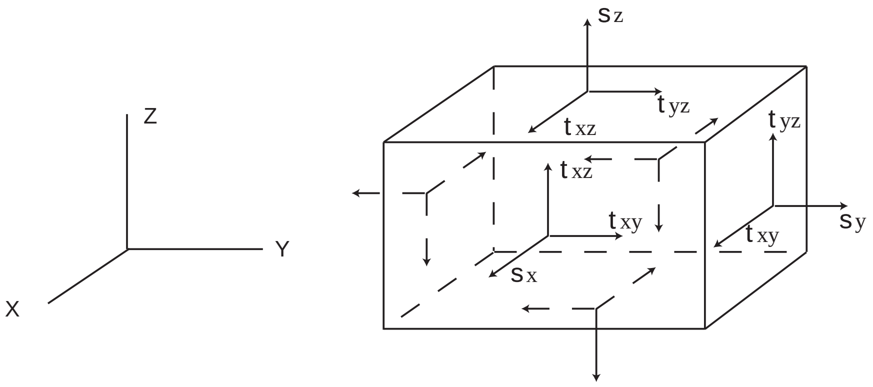

Figure 2.2: Stress components

Differential equations of equilibrium: This theorem describes the relations between the stress components and external force imposed on the object. These equations are applicable to the stress occurring in all kinds of continuous medium, for instance, plastic, fluid, etc.

Fig. 2.2 shows the stress components acting on an infinitesimal cube. X, Y, Z denote the components of the force per unit volume acting on this cube in each direction. The "equations of equilibrium" are obtained by force balancing in x, y and z directions.

$$\begin{aligned}
\frac{\partial \sigma_x}{\partial x} + \frac{\partial \tau_{xy}}{\partial y} + \frac{\partial \tau_{xz}}{\partial z} + X &= 0 \\
\frac{\partial \sigma_y}{\partial y} + \frac{\partial \tau_{xy}}{\partial x} + \frac{\partial \tau_{yz}}{\partial z} + Y &= 0 \\
\frac{\partial \sigma_z}{\partial z} + \frac{\partial \tau_{xz}}{\partial x} + \frac{\partial \tau_{yz}}{\partial y} + Z &= 0
\end{aligned} \tag{2.5}$$

Eqs. (2.5) are applicable only to the small volume in the interior of the object. For a small elements located at the surface of the object, the external force acting on the surface of the object has to be taken into consideration. Let $\overline{X}, \overline{Y}$ and $\overline{Z}$ be the components of the surface force per unit area. Due to the fact that the volume in this surface element case is relatively small, the force per unit volume terms vanish. Thus, the "Equations of equilibrium" are re-written as follows

$$\begin{aligned} \overline{X} &= \sigma_x l + \tau_{xy} m + \tau_{xz} n \\ \overline{Y} &= \sigma_y m + \tau_{yz} n + \tau_{xy} l \\ \overline{Z} &= \sigma_z n + \tau_{xz} l + \tau_{yz} m \end{aligned} \tag{2.6}$$

where l, m and n are the cosines of the angle between the external force and normal direction of the surface of the body, at the point of interest.

The three theorems discussed above cover the basics of the elastic deformation in three-dimension. For any three-dimension deformation problem, by combining all equations above, the relations between external force and displacement can be solved. We will refer to these equations repeatedly in the next two sections. To further clarify the relations and roles of these theorems, we reiterate the statement of each theorem in the following.

1. Differential equations of equilibrium : Provided the relations between external force and stress components.
2. Hooks Law : Provided the relations between stress components and strain components
3. Compatibility Conditions : Provided the relations between strain components and displacements

2.2.2 Torsion stiffness: End plane warping

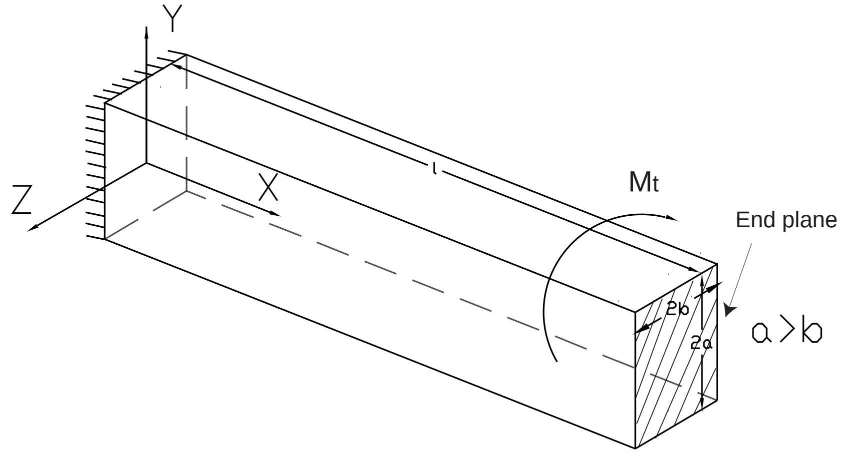

Figure 2.3: Torsion for a rectangular bar

For the torsional stiffness of a rectangular bar, we consider the example shown in Fig. 2.3. This rectangular bar is fixed at one end and is free at the other. When a torque acts on the bar, the plane on the free end appears to be rotated and warped, if no other constraint is imposed.

Based on the Saint-Venant's assumption, all stress components, except τ_{xz} and τ_{yz} vanish. Therefore, we need only to investigate the stress distribution of shear stress over the cross section of the bar. Applying this assumption to the "Differential Equation of Equilibrium" [59], the equations can be simplified to,

$$\frac{\partial \tau_{xz}}{\partial z} = 0 \qquad \frac{\partial \tau_{yz}}{\partial z} = 0 \qquad \frac{\partial \tau_{xz}}{\partial x} + \frac{\partial \tau_{yz}}{\partial y} = 0 \tag{2.7}$$

To satisfy the 3 equations above, we introduce the stress function $\phi(x, y)$ such that,

$$\tau_{xz} = \frac{\partial \phi}{\partial y} \qquad \tau_{yz} = -\frac{\partial \phi}{\partial x} \tag{2.8}$$

The shear force presented above is the consequence of the fact that a torque that was applied to the bar. Therefore, the relation between the applying torque M_t and the shear force can be established as follows:

$$M_t = \iint (\tau_{yz}x - \tau_{xz}y)dxdy = 2\iint \phi dxdy \tag{2.9}$$

Substituting these expressions (Eqs. (2.8), Eqs. (2.9)) into the "Compatibility Equations" Eqs. (2.3) and using "Hook's law" Eqs. (2.4), the characteristic equation of torsion for a prismatical bar is obtained.

$$-2G\theta = \frac{\partial^2\phi}{\partial y^2} + \frac{\partial^2\phi}{\partial x^2} \tag{2.10}$$

where

θ Angle of twist per unit length

G Shear modulus

The exact solution of the stress function ϕ can be solved using Eq. (2.10) and the boundary conditions, $\phi = 0|_{x=\pm a}$; $\phi = 0|_{y=\pm b}$.

$$\phi = \frac{32G\theta b^2}{\pi^3} \sum_{n=1,3,5,\ldots}^{\infty} \frac{1}{n^3}(-1)^{\frac{n-1}{2}} \left(1 - \frac{\cosh\frac{n\pi x}{2b}}{\cosh\frac{n\pi a}{2b}}\right) \sin\frac{n\pi y}{2b} \tag{2.11}$$

Applying the expression of ϕ to the Eq. (2.9) and Eqs. (2.8), the exact solutions for the torsion stiffness, moment and shear force are obtained:

$$\tau_{xz} = \frac{\partial\phi}{\partial y} = \frac{-16G\theta b}{\pi^2} \sum_{n=1,3,5,\ldots}^{\infty} \frac{1}{n^2}(-1)^{\frac{n-1}{2}} \left(1 - \frac{\cosh\frac{n\pi x}{2b}}{\cosh\frac{n\pi a}{2b}}\right) \sin\frac{n\pi y}{2b} \tag{2.12a}$$

$$\tau_{yz} = -\frac{\partial\phi}{\partial x} = \frac{16G\theta b}{\pi^2} \sum_{n=1,3,5,\ldots}^{\infty} \frac{1}{n^2}(-1)^{\frac{n-1}{2}} \left(\frac{\sinh\frac{n\pi x}{2b}}{\cosh\frac{n\pi a}{2b}}\right) \cos\frac{n\pi y}{2b} \tag{2.12b}$$

$$M_t = \frac{1}{3}G\theta(2a)(2b)^3\left(1 - \frac{192}{\pi^5}\frac{b}{a} \sum_{n=1,3,5,\ldots}^{\infty} \frac{1}{n^5}\tanh\frac{n\pi a}{2b}\right) \tag{2.12c}$$

$$K_t = \frac{M_t}{\varphi} = \frac{M_t}{l\theta} = \frac{G(2a)(2b)^3}{3l}\left(1 - \frac{192}{\pi^5}\frac{b}{a} \sum_{n=1,3,5,\ldots}^{\infty} \frac{1}{n^5}\tanh\frac{n\pi a}{2b}\right) \tag{2.12d}$$

where

φ Angle of the twisted rectangular bar

These exact solutions can predict the torsion stiffness well, but they are not easy to apply, nor to simplify in order to use them in an easily-applied approximate solution.

The better approach to obtain an easily-applied approximate solution is to solve this torsion problem by the "Energy Method". Details of the "Energy Method" can be found in the textbook by Timoshenko [59]. The strain energy of the twisted bar per unit length is

$$V = \frac{1}{2G}\iint(\tau_{yz}^2+\tau_{xz}^2)dxdy = \frac{1}{2G}\iint\left[\left(\frac{\partial\phi}{\partial x}\right)^2+\left(\frac{\partial\phi}{\partial y}\right)^2\right]dxdy$$

Therefore, the amount of the energy variation due to the variation of the stress function $\delta\phi$ is

$$\delta V = \frac{1}{2G}\cdot\delta\iint\left[\left(\frac{\partial\phi}{\partial x}\right)^2+\left(\frac{\partial\phi}{\partial y}\right)^2\right]dxdy$$

The same amount of the energy variation is produced by the applying torque. The variation of work done by the torque is $\delta(M_t\cdot\theta)$, where M_t is given in Eq. (2.9). Therefore,

$$\frac{1}{2G}\cdot\delta\iint\left[\left(\frac{\partial\phi}{\partial x}\right)^2+\left(\frac{\partial\phi}{\partial y}\right)^2\right]dxdy = 2\theta\iint\delta\phi dxdy$$

Thus, the true expression of the stress function ϕ must make the following integral U equal to zero

$$U = \iint\left[\frac{1}{2}\left[\left(\frac{\partial\phi}{\partial x}\right)^2+\left(\frac{\partial\phi}{\partial y}\right)^2\right]-G\theta\phi\right]dxdy \tag{2.13}$$

To obtain an approximate solution for the stress function, the stress function is assumed to have the following form

$$\phi = G\theta(b^2-y^2)(1-e^{-\beta(a-x)}) \tag{2.14}$$

where β is yet to be determined. Eq. (2.14), satisfies the boundary conditions at $x = \pm a; y = \pm b$. The value of β is determined so as to make the integral of Eqs (2.13) a minimum

$$\frac{\partial U}{\partial \beta} = 0 \qquad \Rightarrow \qquad \beta = \frac{1}{b}\sqrt{\frac{5}{2}}$$

Applying this expression of β to Eqs. (2.8) and Eq. (2.9), expressions for shear force, moment and torsional stiffness are obtained.

$$\tau_{xz} = -2G\theta y \left(1 - e^{-\beta(a-x)}\right) \tag{2.15a}$$

$$\tau_{yz} = G\theta\beta(b^2 - y^2)e^{-\beta(a-x)} \tag{2.15b}$$

$$\begin{aligned} M_t &= \frac{1}{3}G\theta(2a)(2b)^3(1 - \frac{1 - e^{-a\beta}}{a\beta}) \\ &\approx \frac{1}{3}G\theta(2a)(2b)^3(1 - \frac{1}{a\beta}) \end{aligned} \tag{2.15c}$$

$$K_t = \frac{M_t}{\theta} = \frac{1}{3}G(2a)(2b)^3(1 - \frac{1}{a\beta}) \tag{2.15d}$$

These expressions give a very good approximation to Eqs. (2.12). In the extreme case of $a : b = 1 : 1$, the error is 13%. In the case where $a : b \geq 1.2 : 1$, the error is less than 5%. We will derive our expressions for the non-warping end plane based on the expressions given in Eqs. (2.15) and the "Energy Method".

2.2.3 Torsion stiffness: End plane non-warping

In the case of the non-warping end plane of a twisted rectangular bar, it can be imagined that the imposed extra boundary condition tends to have less effect on the bar's angle of twist as the length of the bar increase. Therefore, the stress distribution near the end of the bar must be different from the stress distribution at other cross sections of the bar. In other words, a "local irregularity" appears at the end of the bar [59].

Consider the example shown in Fig. 2.4. The rectangular bar is fixed at two ends, and a moment is applied at the middle of the bar. The rectangular bar has the dimensions $2l \times 2a \times 2b$. Due to the symmetry of the structure layout and boundary conditions, the structure's middle plane (at z = 0) remains plane when the external torque is applied. We will use this example to derive the expression for torsional stiffness of a twisted rectangular bar (dimensions: $l \times 2a \times 2b$) with both ends remaining plane. In the references [59] [60], this problem is solved for the rectangular bar that has narrow cross section ($a/b \gg 1$). Here we will extend these results to the case of a rectangular bar that has an arbitrary cross section aspect ratio.

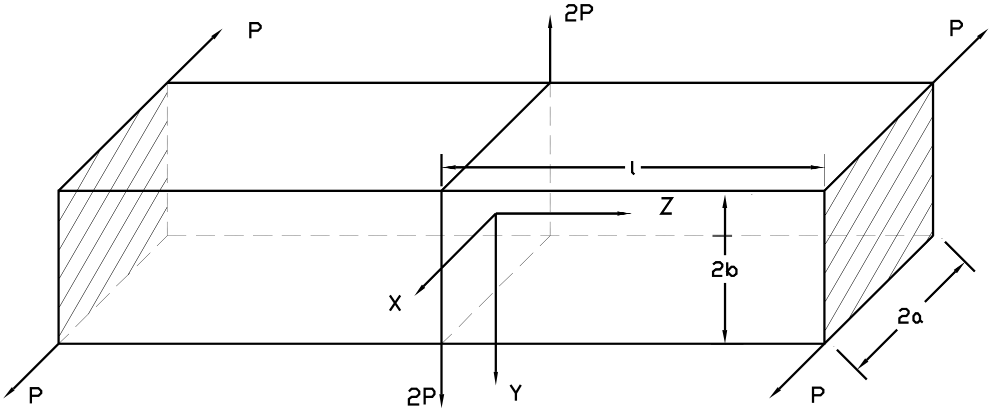

Figure 2.4: A twisted rectangular bar with no warping end plane

In the example shown in Fig. 2.4, in order to prevent the middle plane from warping, the normal stress along the z-direction, σ_z, was utilized to balance out the stress distribution. σ_z is a function of x and y; furthermore, it diminishes with the increase of distance (in z-direction) up to the middle plane. The remaining stress components are chosen in the manner so as to satisfy the "Differential Equations of Equilibrium", Eqs. (2.5), and boundary conditions. These are the extension of Eqs. (2.15). The factor m is yet to be determined.

$$\sigma_z = -mE\theta e^{-mz}xy \tag{2.16a}$$

$$\tau_{xy} = -\frac{1}{8}Em^3\theta e^{-mz}(a^2 - x^2)(b^2 - y^2) \tag{2.16b}$$

$$\tau_{xz} = \frac{1}{4}Em^2\theta e^{-mz}(a^2 - x^2)y - 2G\theta y\left(1 - e^{-\beta(a-x)}\right) \tag{2.16c}$$

$$\tau_{yz} = \frac{1}{4}Em^2\theta e^{-mz}(b^2 - y^2)x + G\theta\beta(b^2 - y^2)e^{-\beta(a-x)} \tag{2.16d}$$

The expressions above meet the boundary conditions at $x = \pm a; y = \pm b$; moreover, they approach the expressions in Eqs. (2.15), the case of warping end plane, as the value of z increases. As before, the "Energy Method" are utilized to acquire the approximate solution for the torsion stiffness. Due to the non-uniform stress distribution along the length of the bar ("local irregularity" effect), the derivation is proceeded on the full length of the bar, instead of only on the cross section, as done previously. The strain energy of a twisted rectangular bar is:

$$V = \frac{1}{2G}\int_{-l}^{l}\int_{-a}^{a}\int_{-b}^{b}\left[\tau_{xy}^2 + \tau_{xz}^2 + \tau_{yz}^2 + \frac{1}{2(1+\nu)}\sigma_z^2\right]dxdydz \tag{2.17}$$

Replace the stress terms by the expressions in Eqs. (2.16), and note that, for a long bar and with sufficient accuracy,

$$\int_0^l e^{-mz}dz \simeq \frac{1}{m}$$

The strain energy based on the Eqs (2.17) is obtained.

$$\begin{aligned} V \;=\; & \frac{1}{9}E\theta^2a^3b^3\left\{\frac{2}{25}(1+\nu)m^5a^2b^2+\frac{1}{5}(1+\nu)m^3(a^2+b^2)+\right.\\ & +m\left[-3+\frac{12}{a^2\beta^2}+\frac{-12}{a^3\beta^3}+\frac{-6}{a\beta}e^{-a\beta}+\frac{12}{a^3\beta^3}e^{-a\beta}+\frac{12}{5}\frac{b^2}{a^2}(2-\frac{2}{a\beta}+\frac{2e^{-a\beta}}{a\beta})\right]+\\ & \left.+\frac{12l}{(1+\nu)a^2}\left[1+\frac{-3+4e^{-a\beta}-e^{-2a\beta}}{2a\beta}+\frac{1}{5}\frac{b^2}{a^2}a\beta(1-e^{-2a\beta})\right]\Bigg]\right\} \end{aligned} \tag{2.18}$$

Meanwhile, the work done by the external torque that was applied to the bar is,

$$W=2\int_0^l\int_{-b}^b\int_{-a}^a\phi\theta dxdydz=\frac{12l}{(1+\nu)a^2}(2-\frac{2}{a\beta}+\frac{2e^{-a\beta}}{a\beta})$$

Again, the values of m and β are determined in the manner as to make potential energy $(V-W)$ a minimum. This minimum condition results in the following two equations for solving for m and β:

$$\frac{\partial(V-W)}{\partial m}=0$$

$$\frac{\partial(V-W)}{\partial\beta}=0$$

Therefore,

$$\begin{aligned} & \frac{2}{5}(1+\nu)a^2b^2m^4+\frac{3}{5}(1+\nu)(a^2+b^2)m^2-3+\frac{12}{a^2\beta^2}+\frac{-12}{a^3\beta^3}+\frac{-6}{a\beta}e^{-a\beta}+\\ & \quad+\frac{12}{a^3\beta^3}e^{-a\beta}+\frac{12}{5}\frac{b^2}{a^2}(2-\frac{2}{a\beta}+\frac{2e^{-a\beta}}{a\beta})=0 \end{aligned} \tag{2.19}$$

$$\begin{aligned} & -\frac{24}{a\beta}+\frac{36}{a^2\beta^2}+6(a\beta+1)e^{-a\beta}-\frac{12(a\beta+3)}{a^2\beta^2}e^{-a\beta}+\frac{24}{5}\frac{b^2}{a^2}\left[1-(a\beta+1)e^{-a\beta}\right]+\\ & \quad+\frac{12l}{(1+\nu)a^2m}\left[\frac{-1}{2a\beta^2}+\frac{b^2}{5a}+(\frac{-b^2}{5a}+\frac{2b^2\beta}{5}+\frac{2a\beta+1}{2a\beta^2})e^{-2a\beta}\right]=0 \end{aligned} \tag{2.20}$$

m and β can be obtained by solving Eq. (2.19) and Eq. (2.20) simultaneously.

To calculate the angle of the twisted bar φ, we set the potential energy V to be equal to the work done by the torque M_t. Thus,

$$\frac{M_t\varphi}{2}=V$$

The expression of K_t is obtained by the simple manipulation this equation equation

$$K_t = \frac{M_t}{\varphi} = \frac{M_t^2}{2V} \tag{2.21}$$

where the expression of V is given in Eq. (2.18) and the expression of M_t is given by Eqs. (2.15). Thus, K_t can be obtained by solving equations Eq. (2.21), Eq. (2.20), Eq. (2.19), Eq. (2.18) and Eqs. (2.15) simultaneously.

As it is obvious that it is not easy to solve the five above equations simultaneously, the approach that will be followed here is to obtain approximate solutions for β and m, and then apply the results to the expression for K_t. To obtain an approximate solution for β, Eq. (2.20) was solved first. Eliminating all the exponential and high order terms in Eq. (2.20), we are left with the following equation,

$$\frac{1}{a^2\beta^2}\left[\frac{l}{6(1+\nu)a^2m} - \frac{2}{15}\frac{b^2}{a^2}\right] - \frac{lb^2}{15(1+\nu)a^4m} = 0 \tag{2.22}$$

Assuming $l > a$ and ignoring the less significant term, β is obtained as,

$$\beta = \sqrt{\frac{5}{2}\frac{1}{b}}$$

An analogous approach is applied to Eq. (2.19) in order to solve for m:

$$\frac{2}{5}(1+\nu)a^2b^2m^4 + \frac{3}{5}(1+\nu)(a^2+b^2)m^2 - 3 + \frac{12}{a^2\beta^2} + \frac{-12}{a^3\beta^3} + \frac{12}{5}\frac{b^2}{a^2}(2 - \frac{2}{a\beta}) = 0$$

Resulting in

$$m = \sqrt{\frac{5\left[1 - (1 - \frac{1}{a\beta})(\frac{4}{a^2\beta^2} + \frac{8}{5}\frac{b^2}{a^2})\right]}{(1+\nu)(a^2+b^2)}} \tag{2.23}$$

Using the expression of β obtained above, we have

$$m = \begin{cases} 0 & \text{for} \quad 0.79 \leq \frac{b}{a} \leq 1.0 \\ \sqrt{\frac{5-16\frac{b^2}{a^2}(1-\sqrt{\frac{2}{5}}\frac{b}{a})}{(1+\nu)(a^2+b^2)}} & \text{for} \quad \frac{b}{a} \leq 0.79 \end{cases}$$

The above expressions for m and β will now be used in Eq. (2.18). Without losing much accuracy, we can eliminate the exponential terms $e^{-a\beta}$, $e^{-2a\beta}$ and high order aspect ratio (b/a) terms from Eqs (2.18). Thus, the new expression of the strain energy, in terms of the structure dimensions, is

$$V = \begin{cases} \frac{1}{2}\left[\frac{1}{3}G\theta^2(2a)(2b)^3(1-\sqrt{\frac{2}{5}\frac{b}{a}})\right] l & \text{for} \quad 0.79 \le \frac{b}{a} \le 1.0 \\ \frac{1}{2}\left[\frac{1}{3}G\theta^2(2a)(2b)^3(1-\sqrt{\frac{2}{5}\frac{b}{a}})\right] \left\{ l - a^2 \left(\frac{8}{15} - \frac{1}{6(1-\sqrt{\frac{2}{5}\frac{b}{a}})} \right) * \cdots \right. & \\ \qquad\qquad \left. * \cdots \sqrt{\frac{(1+\nu)(5-16\frac{b^2}{a^2})(1-\sqrt{\frac{2}{5}\frac{b}{a}})}{a^2+b^2}} \right\} & \text{for} \quad \frac{b}{a} \le 0.79 \end{cases}$$

Applying the expression of the strain energy above and the moment M_t in Eqs. (2.15) to the torsion stiffness K_t in Eq. (2.21), we obtain

$$K_t = \begin{cases} \frac{1}{3}G(2a)(2b)^3(1-\sqrt{\frac{2}{5}\frac{b}{a}})l^{-1} & \text{for} \quad 0.79 \le \frac{b}{a} \le 1.0 \\ \frac{1}{3}G(2a)(2b)^3(1-\sqrt{\frac{2}{5}\frac{b}{a}}) \left[l - a^2 \left(\frac{8}{15} - \frac{1}{6(1-\sqrt{\frac{2}{5}\frac{b}{a}})} \right) * \cdots \right. & \\ \qquad\qquad \left. * \cdots \sqrt{\frac{(1+\nu)(5-16\frac{b^2}{a^2})(1-\sqrt{\frac{2}{5}\frac{b}{a}})}{a^2+b^2}} \right]^{-1} & \text{for} \quad \frac{b}{a} \le 0.79 \end{cases} \tag{2.24}$$

During the process of derivation this approximate solution, we noticed that, in order for the new formula to have a result relatively close to the exact solution, not only must the aspect ratio of the cross section be large ($a/b \gg 1$) but also the ratio of the length of the rectangular bar to the larger dimension of the cross section must also be large ($l/a \gg 1$). We verified this new expression with the results obtained from finite element simulation. In order to demonstrate the importance of the two key factors discussed above ($a/b \gg 1$ and $l/a \gg 1$), several finite element simulations were performed in which the height of the torsion bar was varied while keeping the width and length of the torsion bar constant. Therefore, when the height is small, the small aspect ratio of the cross section dominates the prediction error; when the height is large, the small length over height ratio dominates the prediction error. In this set of simulations, the width $2b$ is 16 μm, the length l is 230 μm and the height varies from 16 to 160 μm. This corresponds to changing the aspect ratio of the cross section from 1 to 10 and the ratio between length and height from 14 to 1.4. Simulation results are shown in Fig. 2.5. For comparison, the torsional stiffness predicted by the equations based on the assumption of narrow cross section (derived by Timoshenko) is also shown in the same plot. As indicated in the plot, the equations that rely on the narrow cross section assumptions do not match the FEM results in the low aspect ratio regime nor the regime where the height is close to the length of the bar. In the extreme case in this simulation, the prediction error from the narrow-cross-section equation is about 20%, while it is just 1.1% when the equations derived in this chapter are used.

The torsional stiffness predicted by the new equations is fairly close to the results obtained from FEM simulation. Although the new formula is more complicated than Timoshenko's, the results predicted by the new formula are more accurate and applicable to a broader range of rectangular bar designs.

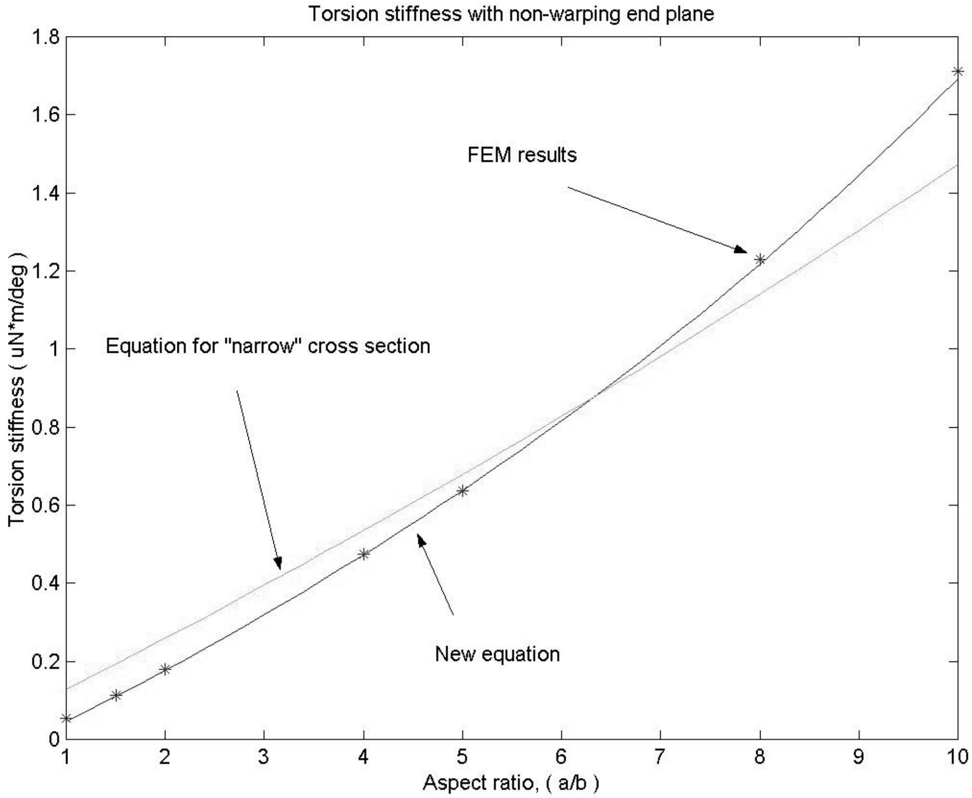

Figure 2.5: Torsion stiffness of a rectangular bar with non-warping end plane

Chapter 3

Design of PZT-Actuated Silicon Suspensions

Fig. 3.1 shows a photograph of our PZT-actuated silicon suspension prototype. The suspension was micro-fabricated using single crystal silicon as the structural material and has an in-situ piezoresistive film (piezoresistor) deposited upon it. Four pieces of bulk PZT strips are glued to the silicon suspension: one pair is glued on the top side, the other on the bottom. These PZT strips leverage through a push-pull scheme to move the magnetic head in the in-plane radial direction. When the PZT stretches the suspension to position the magnetic head, it also stretches the deposited piezoresistive film. This piezoresistor produces an electrical signal that is proportional to its deformation and can be used to determine the position of the magnetic head relative to the VCM (Voice Coil Motor); this signal is known as the RPES (Relative Position Error Signal). The silicon suspension is subsequently glued to a pre-cut steel portion, as shown in the figure. This pre-cut steel suspension is pre-bent and has a pivot which is attached to the E-block. The pre-bend in

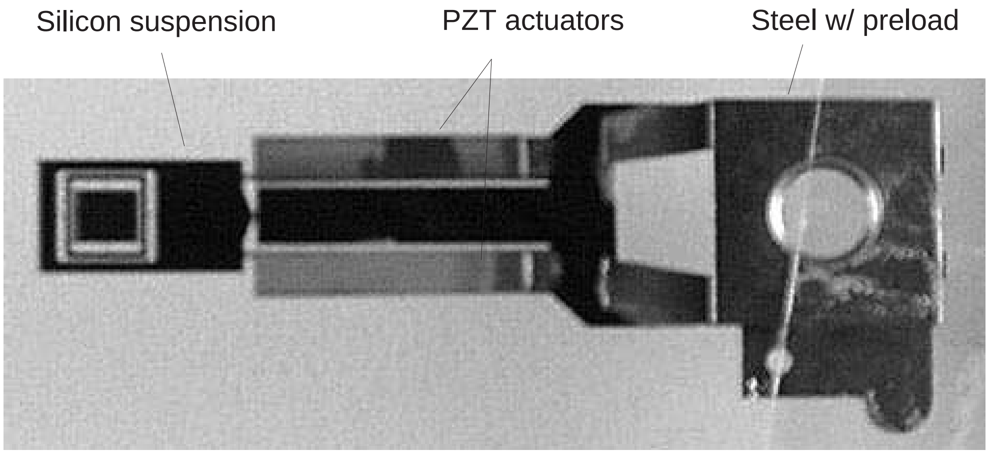

Figure 3.1: Prototype of PZT-actuated silicon suspension

the steel portion of the suspension is necessary to provide a downward preload force on the slider, which counteracts the air bearing forces that act on the slider when it flies on top of the rotating hard disk. The steel-silicon suspension assembly shown in Fig. 3.1 has the same boss-to-gimbal length as most commercial products.

The silicon suspension design incorporates several special features for enabling PZT actuation. These enhance the dual-stage servo performance and lower the required PZT driving voltage. Features on the silicon suspension include:

1. Integrated gimbal
2. Leverage
3. Stretch area
4. Piezoresistive RPES sensors

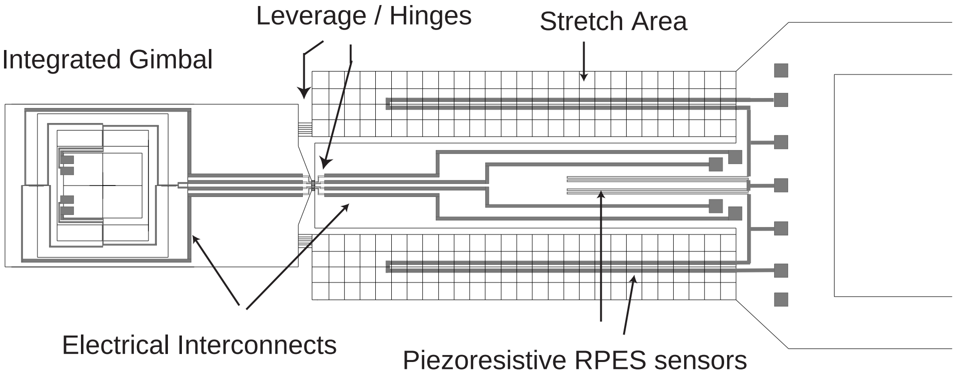

Figure 3.2: The schematic of silicon suspensions

5. Electrical interconnects

Fig. 3.2 shows the design features that were implemented on our proposed silicon suspension. The details of these features will be discussed in the following sections.

3.1 Integrated Gimbal Design

The design goal for the gimbal structure is to allow its seamless integration as part of a one-piece silicon suspension, which is fabricated using MEMS techniques. In addition, in order to simplify the fabrication process, both the gimbal structure and the suspension that houses it should possess the same structural height. As discussed in the previous chapter, the requirements of the dynamic characteristics of gimbal structures: large flexibility in the pitch and roll motion but relative large stiffness in in-plane and out-of-plane bending motion, make the design of gimbal structure difficult, if it is to be fabricated from a single piece of material. In this section, we first investigate the dynamic characteristics of a conventional gimbal structure, which has orthogonal sets of torsion bars, in order to disclose the difficulties of designing such a gimbal and its performance limitations. Based on these qualitative results, we then proposed new solutions to this gimbal design challenge. The orthogonal-torsion-bar gimbal structure is chosen because it offers more out-of-plane stiffness than other types of the gimbal structures discussed in the previous chapter.

3.1.1 Gimbal with one-flexure torsion bar

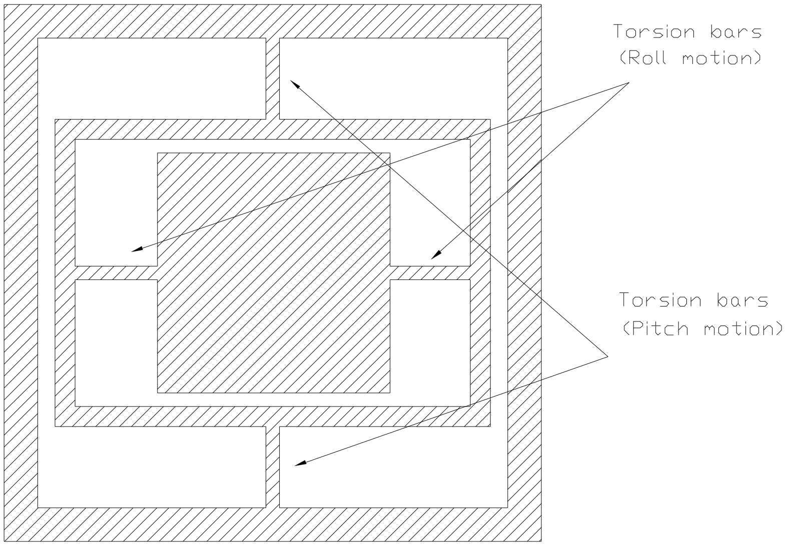

Figure 3.3: The schematic of the conventional gimbal structure

Fig. 3.3 shows the schematic of the conventional gimbal structure. Flexures on the top and bottom are designated for the pitch motion; flexures on the left and right are for the roll motion. The magnetic head sits in the central coupon of the structure. This configuration of torsion bar design is referred to as the "one-flexure" torsion bar in this dissertation. The major drawback of this design is that there exists a strong conflict between high in-plane bending stiffness and low torsion stiffness, which are the performance requirements of the gimbal structure.

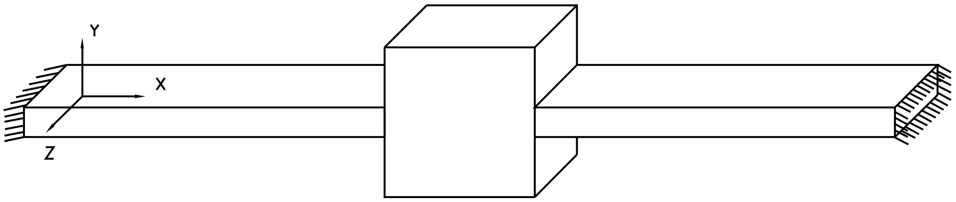

Figure 3.4: The schematic of the simplified one-degree-freedom gimbal structure

To understand this problem, the torsional stiffness and bending stiffness of the structure, shown in Fig. 3.4, are analyzed. This structure is the simplified version of a one-degree-of-freedom gimbal structure. It consists of a block in the middle and 2 rectangular bars on the left and right. Furthermore, the Young's modulus of the middle block is assumed to be 1000 times higher than the Young's modulus of rectangular bars on the left and right. Because the middle block is much stiffer than the rectangular bars, the deformation of the middle block can be ignored when the whole structure is subjected to external forces or torques. This structure is symmetric along the Y–Z plane, which preserves the property of symmetry of the original gimbal structure. Because of the symmetry of this structure, the bending and torsion stiffness of the overall structure can be obtained by calculating the stiffness of one rectangular bar with the extra symmetry constraint imposed on it. To calculate the bending stiffness, the situation is that of the "fixed-guided" rectangular bar

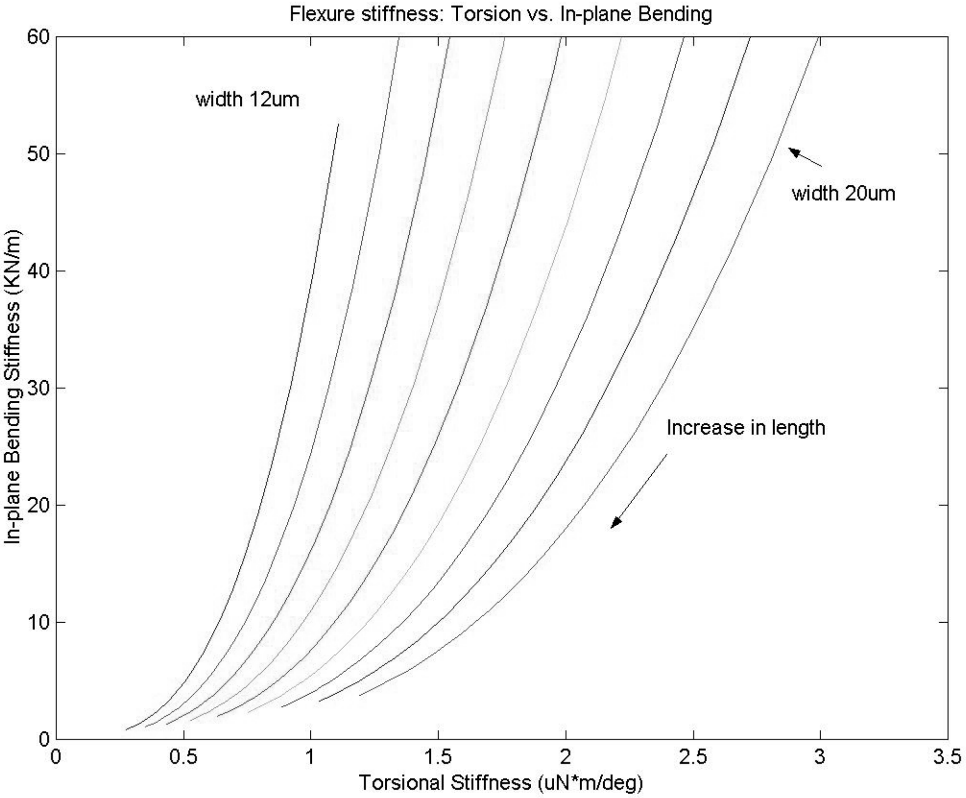

Figure 3.5: In-plane bending stiffness vs. Torsion stiffness of the simplified gimbal structure: various torsion bar width (I)

both in Y and Z direction; for the torsional stiffness, it is the "non-warping end plane" of a twisted rectangular bar. The formulas listed in Chapter 2. are utilized in the simulations that follow.

In this simulation, we intend to show the coherence between in-plane bending stiffness and torsional stiffness of the one-degree-freedom gimbal structure. The rectangular bars, responsible for the torsional motion have the following dimensions: the height is kept at 80 μm while the width is varied from 12 to 20 μm and the length is varied from 100 to 400 μm. The simulation result, as shown in the Fig. 3.5, indicates that the torsion stiffness increases monolithically with the bending stiffness. A flexible torsion stiffness design usually

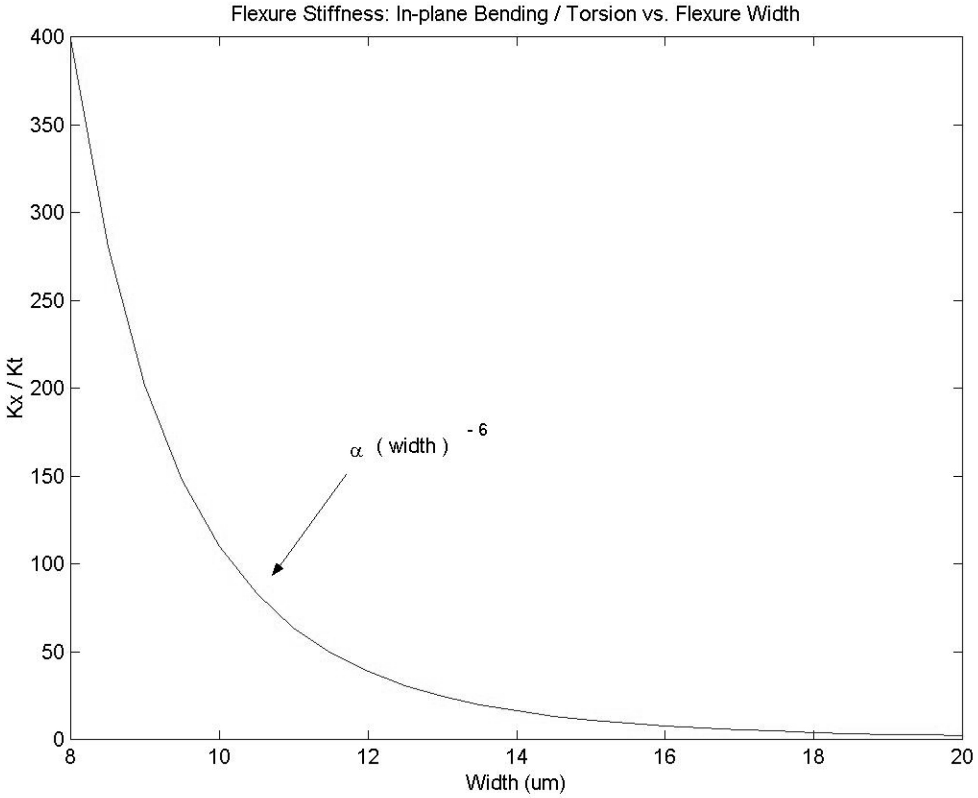

Figure 3.6: In-plane bending stiffness vs. torsion stiffness of the simplified gimbal structure: various torsion bar width (II)

comes with flexible in-plane bending stiffness. However, if the width of the rectangular bar can be designed as small as possible, it is possible to achieve the flexible torsion stiffness with the required rigidity of the in-plane bending stiffness.

Another simulation was done to enlighten the observation regarding narrowing the width of the torsion bar. In this simulation (Fig. 3.6), the height of the rectangular bar stays constant at 80 μm, while the width is varied from 8 to 20 μm and the length of the bar is varied accordingly to maintain the torsion stiffness at 1 μNm/deg. As indicated in the plot, the in-plane bending stiffness decreases roughly at the rate of $(width)^{-6}$ while the torsion stiffness is kept the same. From the simulation above, it can be concluded that the

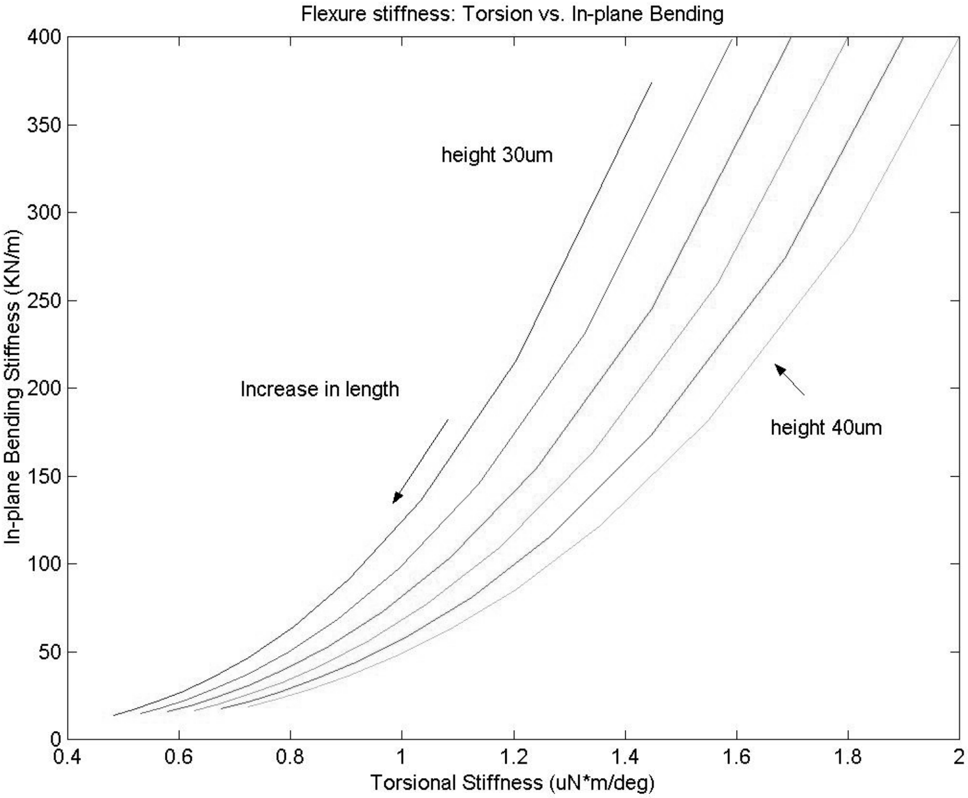

Figure 3.7: In-plane bending stiffness vs. torsion stiffness of the simplified gimbal structure: various torsion bar height

smaller the width of the torsion bars, the better the dynamic performance of the gimbal structure. However, a very narrow torsion bar is usually not practical. The manufacturing cost, process reliability and other constraints set limitations on scaling down the width of torsion bars.

An analogous simulation is done to explore the effectiveness of varying the height of the torsion bar. In this simulation, the width of the torsion bar is 16 μm, while the height is varied from 30 to 40 μm and the length is varied from 50 to 150 μm. The simulation result is shown in the Fig. 3.7. A similar result to the previous simulation is observed and an analogous remark can be made for the various heights of the torsion bar: The lower the height of the torsion bar, the better the dynamic performance of the gimbal structure. Although the trends in Fig. 3.5 and Fig. 3.7 look alike, the in-plane bending stiffness in Fig. 3.7 is about 20 times higher than that in Fig. 3.5. This observation indicates that lowering the height of the torsion bar is more effective in achieving the ”flexible torsion and rigid in-plane bending” performance requirement than reducing the width. The major shortcoming of this approach is the soft bending stiffness in the out-of-plane direction. This is not a problem in the conventional 2–3 piece steel suspension design. The gimbal structure can be made of 30 μm thick steel to have the excellent dynamic performance, while the load beam is made of 80 μm thick steel to hold the gimbal structure in place.

In our one-piece silicon suspension design, in order to keep the fabrication process of the overall suspension as simple as possible, the integrated gimbal cannot carry a dimple structure. Furthermore, all elements of the gimbal structure, including the torsion bars, were designed to have the same thickness as the rest of suspension. This rules out the possibility of using thin (in height) torsion bars to achieve performance requirement. Moreover, in order to leave sufficient space for running the necessary wires through the torsion bars to the end of the suspension (close to E-block), the minimum width of the torsion bars was pre-determined. Given the very limited design parameter space, it is difficult to match all gimbal and suspension dynamics requirements with the one-flexure gimbal structure.

3.1.2 Gimbal with double-flexured torsion bar

In this one-piece silicon suspension design, we propose a brand new torsion bar design to achieve the stringent gimbal performance requirements. The schematic of this new design is shown in Fig. 3.8. This new design has a similar structure as the conventional

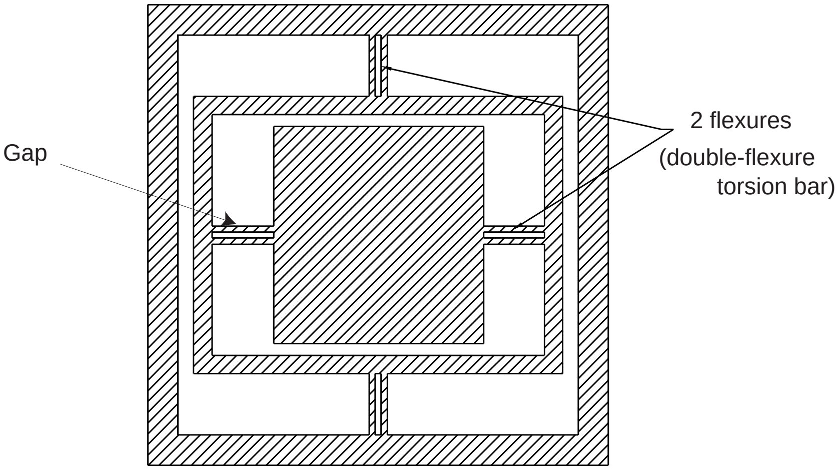

Figure 3.8: The schematic of the double-flexure gimbal structure

gimbal, except for the torsion bars. The new torsion bar consists of two rectangular bars situated very close to each other. This configuration of torsion bars is referred to as the ”double-flexure” torsion bar in this dissertation. Again, a simplified structure, as shown in Fig. 3.9, is analyzed to explain for the reasons why the double-flexure torsion bar surpasses the conventional one-flexure torsion bar design.

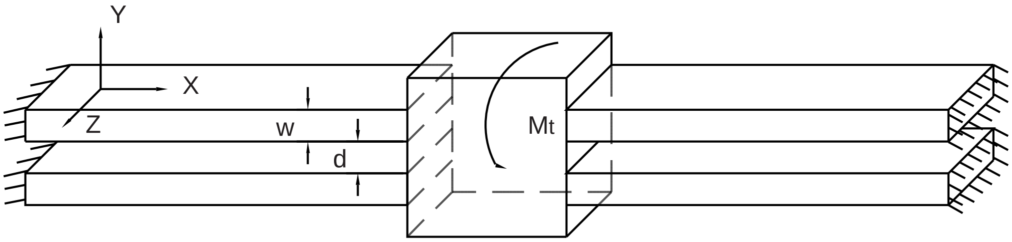

Figure 3.9: Schematic of the simplified one-degree-freedom, double-flexure gimbal structure

The simplified structure has a middle block and 2 rectangular bars on each side. The assumptions of this structure are the same as those of the simplified one-degree-freedom gimbal structure. The torsion motion of the double-flexure configuration involves the torsion motion and bending motion of each rectangular bar. Based on the "small angle" assumption, this motion can be simplified as the superposition of the torsion motion in X direction and bending motion in Z direction. The full derivation for torsion stiffness of the structure above is presented in Appendix A. For the torsion stiffness of the one-degree-freedom, double-flexure gimbal structure, K_t, is given by

$$K_t = 4K_{tr} + K_z(d + w)^2 \tag{3.1}$$

where,

K_t	Torsion stiffness of the overall structure
K_z	Bending stiffness in the Z-direction of one rectangular bar
K_{tr}	Torsion stiffness of one rectangular bar
d	Gap between two adjacent bars
w	Width of each rectangular bar

The expressions of K_{tr} and K_z can be found in the previous chapter.

The torsional stiffness of the double-flexure torsion bar, estimated by Eq. (A.4) and an FEM simulation, is shown in Fig. 3.10. In this simulation, the dimensions of each rectangular bar are 230 μm × 80 μm × 16 μm, and the gap (d) between two adjacent rectangular bars varies from 2 μm to 32 μm. As can be seen in the plot, the simplified formulation in Eq. (A.4) predicts the torsion stiffness of double-flexure torsion bar fairly accurately. The difference between the results obtained from Eq. (A.4) and the FEM simulation is less than 3% in the extreme case where the gap is 32 μm wide, twice the width

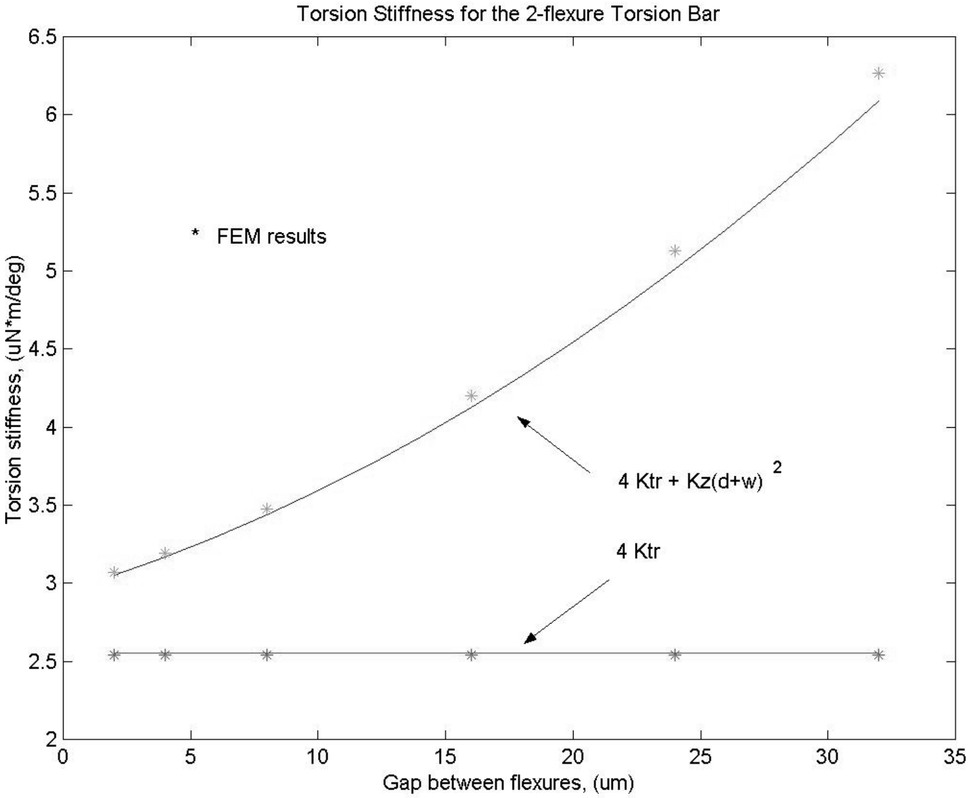

Figure 3.10: Torsion stiffness of the double-flexure torsion bar

of the rectangular bar. We also observe that the value of K_t approaches $4K_{tr}$ when the term $K_z(d+w)^2$ is negligible. In order to drop out the term $K_z(d+w)^2$ from Eq. (A.4) without losing much accuracy, the gap between the two adjacent bars has to be small and, for each rectangular bar, the length has to be greater than the height to a sufficient degree to sustain the relation, $4K_{tr} \gg K_z w^2$. The effect of the width (w) of the rectangular bar is left behind in this approximation due to the fact that the width has roughly the same amount of contribution to both K_{tr} and $K_z(d+w)^2$.

To explain how the double-flexure torsion bar design alleviates the conflict between flexible torsion stiffness and high in-plane bending stiffness, we assume a small gap (d) and

$K_t \simeq 4K_{tr}$. The overall structure has the in-plane bending stiffness of value $4K_y$, where K_y is the bending stiffness of one rectangular bar. The ratio of in-plane bending stiffness to torsion stiffness for double-flexure torsion bar is roughly equal to $4K_y/4K_{tr}$, which is the same formula as for the one-flexure torsion bar. However, with double-flexure torsion bar design, the width of each rectangular bar only needs to carry one metal lead, and thus can be narrower than the width of a one-flexure torsion bar design. With this narrower width, the ratio of in-plane bending stiffness vs. torsion stiffness increases dramatically at roughly the rate of $(width)^{-6}$ (as shown in Fig. 3.6).

In the one-flexure torsion bar design, each torsion bar must carry 2 metal leads. The design rule of the fabrication process dictates minimum space of 16 μm to lay out 2 adjacent metal leads. Thus the width of each torsion bar must be at least 16 μm. In the double-flexure torsion bar design, each rectangular bar carries only one wire. By applying the same design rule, 8 μm is needed for each wire and therefore, an 8 μm minimum width is necessary for each torsion bar in the double-flexure gimbal structure. Since the double-flexure gimbal has twice as many rectangular bars as the one-flexure gimbal, each rectangular bar in the double-flexure gimbal shares roughly one-half of the required stiffness of the one-flexure gimbal, based on the small gap between the flexures and the fact that $K_t \simeq 4K_{tr}$ is assumed. Therefore, the ratio of in-plane bending stiffness to torsion stiffness of the double-flexure gimbal can be increased as much as 32 times ($(16/8)^6 \div 2$), as compared with the one-flexure gimbal.

In the fabrication of one-piece silicon suspension design, the width of each rectangular bar in the double-flexure gimbal is designed to be 10 μm, instead of 8 μm, as discussed above. This approach increases the fabrication process reliability at the expense of minor loss in performance (width is wider than required). Furthermore, the gap between 2 adjacent rectangular bars is 4 μm and the height of each rectangular bar is 80 μm. To realize the small gap assumption, a more advanced fabrication technique is needed. In this case, a deep-trench etch that is 4 μm apart and 80 μm deep is needed to fabricate two adjacent torsional bars for the double-flexured gimbal. That corresponds to the fabrication capability of trenches etch with the etched profile that has the aspect ratio of 20.

3.1.3 FEM simulation

FEM simulation was done on two different gimbal structure designs: Design I and Design II. Design I is a one-flexure gimbal and the Design II is a double-flexure gimbal. In this FEM simulation, the slider (sized the same as a picoslider) and 50 μm of epoxy, located at the center coupon of the gimbal, are included in the model. Neither the dimple structure nor the air bearing are modeled. The dimensions of the torsion bars in each design are listed in the Table 3.1.

Unit:μm	Design I (one-flexure)	Design II (double-flexure)
Flexures for roll motion	230×16×80	150×10×80
Flexures for pitch motion	250×16×80	170×10×80

Table 3.1: Dimensions of gimbal torsion bars

Table 3.2 shows the FEM simulation results of the two silicon gimbal designs. For comparison purposes, the dynamic response characteristics of a commercial product (TSA series, manufactured by Hutchinson Technology Inc.) and a silicon gimbal design proposed by [64] are also listed. Both Design I and II have the torsion stiffness in the range of the TSA series and a higher in-plane stiffness (sway motion) than the TSA series. Design II is more rigid in in-plane bending and out-of-plane bending stiffness than Design I. Moreover, it has more space to run wires through the torsion bars. Design I and II are one-piece suspensions, while the TSA series are 2-piece suspensions (Load beam and Flexure). The gimbal structure thickness of the TSA series is 25 μm, and it uses a dimple structure from the load beam to produce enough out-of-plane bending stiffness. The silicon gimbal design proposed by Wu, etc. [64] has serpentine microsprings as the torsion bars, and its roll and pitch stiffnesses do not fall in the range of the TSA series.

	Design I	Design II	TSA series	Silicon gimbal (Wu)
Roll (μNm/deg)	1.14	1.4	0.85–1.5	1.9
Pitch (μNm/deg)	1.07	1.16	0.85–1.5	2.5
Sway (KHz)	9.4	11.3	6.8–10.5	9.7
Out-of-plane stiffness(KN/m)	8.24	11.5		0.198

Table 3.2: FEM of silicon gimbal design

3.2 Leverage Design

Fig. 3.11 shows the location and design of the leverage structure in our proposed silicon suspensions. As was discussed in the introduction, PZT material has a better performance when it stretches in the axial direction than producing bi-layer bending motion. In order to benefit from the linear motion of PZT actuation, a leverage structure which can transform the axial motion of the PZT strips into in-plane angular motion of the integrated gimbal structure was designed. Because the actuated displacement from the secondary actuator is sub-micron, the associated mechanism must be frictionless to ensure high posi-

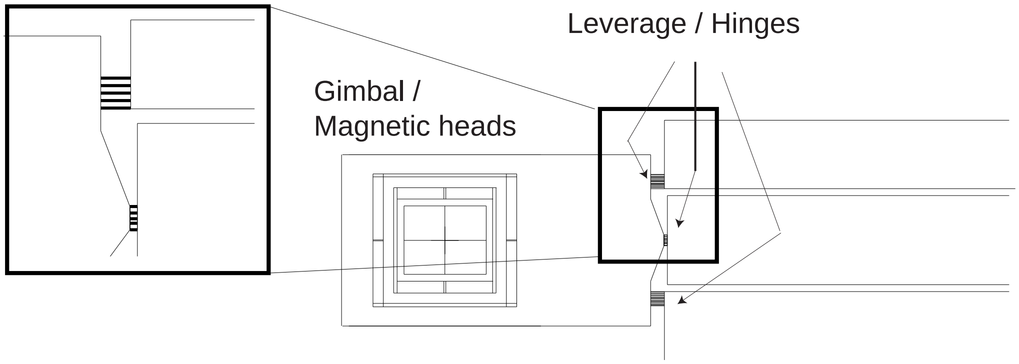

Figure 3.11: The leverage structure in silicon suspensions

tion accuracy. Monolithic flexures were chosen to implement this leverage structure mainly because of their frictionless motion.

The schematic of the leverage structure in this suspension design is shown in Fig. 3.12. The leverage structure consists of three hinges, two hinges are located at the end of PZT actuators and one hinge is located at the middle of the suspension. When the PZT actuators stretch in their axial direction, the two hinges located at the end of the PZT actuators move along with the PZT actuators; the hinge that is located at the middle of the suspension stays there, and the two strong connecting bars bend all the three hinges to convert the linear motion of PZT actuation into a radial motion of the magnetic head (where the "x" is located in Fig. 3.12). Hinges are made of flexible flexures and they direct the motion by their own bending movement.

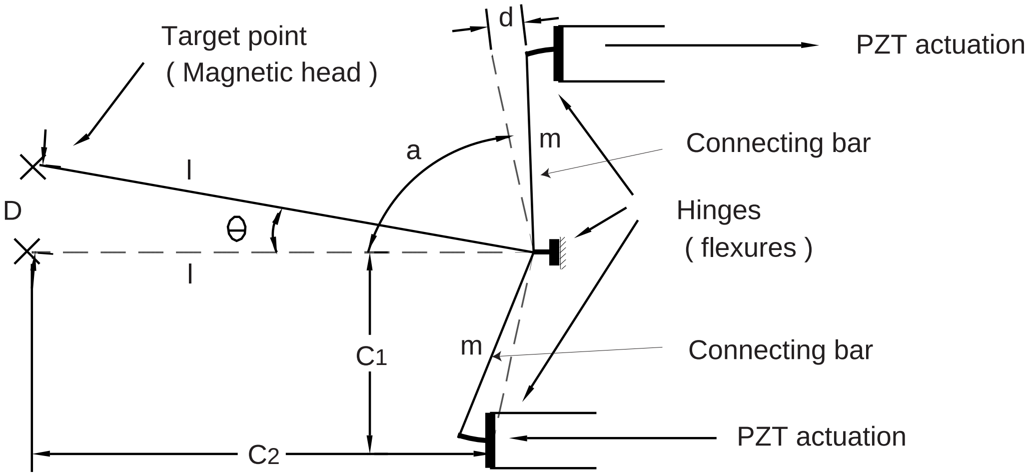

Figure 3.12: Schematics of the leverage structure

3.2.1 Displacement-amplification factor of the leverage

The displacement-amplification factor is defined as the ratio between the stroke of the target point (magnetic head) and the actuated distance at the input terminal (displacement of the PZT actuators). A high displacement-amplification factor implies that a small amount of stretch is needed from the PZT actuators, which in turn result in a lower PZT actuation voltage. The value of parameters c_1 and c_2, shown in the Fig. 3.12, are determined by the location of the leverage structure and the geometry of the overall suspension. Given c_1 and c_2, the optimal displacement-amplification factor and correlated angle α can be obtained.

Assume that θ is small,

$$\begin{aligned} D &= l\theta \\ d &= m\theta \\ c_1 &= m\sin\alpha \\ c_2 &= l - m\cos\alpha \end{aligned}$$

The displacement amplification factor S is then defined as follows,

$$\begin{aligned} S &= \tfrac{D}{d} = \tfrac{l}{m} \\ &= \cos\alpha + \tfrac{c_2}{c_1}\sin\alpha \\ &= \sqrt{1 + (\tfrac{c_2}{c_1})^2}\sin(\alpha + \phi) \qquad \phi = \tan^{-1}\tfrac{c_1}{c_2} \end{aligned}$$

$$\max_{\alpha} S = \sqrt{1 + (\frac{c_2}{c_1})^2} \qquad \alpha = \frac{\pi}{2} - \tan^{-1}\frac{c_1}{c_2} \tag{3.2}$$

3.2.2 Location of the leverage

Most PZT-actuated suspension designs place their PZT strips and leverage structure close to the E-block. In this case, $c_2 >> c_1$, and the displacement-amplification factor can be as high as 10 – 12 [36] [10]. The advantages and disadvantages of this configuration have been discussed in the introduction section. In this silicon suspension design, due to the design constraint that every mechanism has to be implemented onto one piece of silicon, it is difficult to place the leverage close to the E-block. The explanation for this follows: In order to have the slider (magnetic head) fly on top of the rotating disk properly, a preload is applied on the slider to counter act the air bearing lift. This is done by flexing the suspension with an angle ($\simeq 7^\circ$). Then, the angle is pushed back ($\simeq 1^\circ$) when the suspension is loaded on the disk. The stress distribution along the suspension, due to the preload, is proportional to the distance to the location where the air bearing responds to the preload.

Due to the very narrow width of the three hinges implemented on the suspension, the stress distribution reaches its highest point at the location of the leverage structure. This stress concentration could rip off the silicon suspension due to the brittleness of the silicon. To lower this stress concentration effectively, we gain understandings from the following equation. The equation is for the stress distribution along a cantilever beam, which is fixed at one end and free at the other. A point force P acts on the free end.

$$\begin{aligned} \sigma(x) &= \frac{M\frac{h}{2}}{I_z} \\ &= 6P\frac{1}{h^2}\left(\frac{x}{w}\right) \qquad (3.3) \\ & \qquad (3.4) \end{aligned}$$

where,

σ	Stress due to the bending motion
x	Distance to the location where the point force is acting
w	Width of the cantilever beam
h	Height of the cantilever beam

From the equation above, the most effective way of lowering the stress is to increase the height of the overall suspension. This approach results in an increase in the height of the integrated gimbal torsion bar, thus causing the performance of the gimbal structure to degrade. The alternatives are either to increase the width of the hinges or shorten the distance between the leverage and the head assembly. The width of hinges is increased at the expense of excessive PZT actuation force to flex flexures. On the other hand, placing the leverage structure close to the head assembly reduces the displacement-amplification factor, and thus increases the needed PZT stretch. Both of the approaches increase the PZT actuation voltage. However, the latter approach result in a better dual-stage servo scheme from the viewpoint of reducing PES induced by suspension vibration (see the discussion in the section, "Introduction").

In this leverage design, the location is chosen close to the head assembly. The displacement-amplification factor is calculated to be 3.67 with 74.2 degrees for angle α.

3.2.3 Hinge design

In this silicon suspension design, both the PZT actuators and the piezoresistors sensor (will be discussed later) lie behind the leverage structure. Inevitably, the actuation/sensing actions for the the head assembly are transmitted through the leverage structure, making obvious the importance of a proper leverage design to the success of the suspension. Furthermore, the stiffness of the hinges in the in-plane motion is the key factor for a good leverage design. The stiffness needs to be rigid to ensure the high accuracy of the secondary actuation. On the other hand, over-rigidity of the hinge structure consumes the excess of PZT actuation force to bend the flexures. The rule of thumb that the resonance of the hinge structure in the in-plane motion should be 10 times higher than required system response was used in this design. To follow this design rule, the hinge structure was designed to have a resonance close to 20 KHz.

From the stress distribution resulting from the preload, we determined the overall width of the hinge structure. The height of the hinge is the same as that of the rest of the suspension ($h = 80\ \mu$m); the preload of the suspension (P), equals to 2 gram which is the amount of force that keeps the magnetic head in place under 1000 G shocks (1000 * 2 mg = 2 gram); and the location of the hinge structure (x) is 3 mm (as discussed in the previous section). The upper limit of the stress concentration ($\sigma(x)$) is set by the fracture strength of the single crystal silicon along with the safety factor of 10. By applying the stress distribution, Eq. (3.3), and all numbers discussed above, the minimum width (w) of the hinge structure is determined to be approximately 250 μm. The total area 250 μm is then split into 90 μm / 70 μm / 90 μm for the three hinges in the leverage structure.

As described earlier, the leverage structure was implemented to convert the push-pull motion of the PZT strips into an in-plane slider rotation motion. Ideally, we would want this rotation motion to be pivoted at the middle hinge, so that the movement of the magnetic head can be precisely predicted by the linear movement of the PZT strips (where the additional position sensor is located) and the displacement-amplification factor. Unfortunately, this situation only happens in a leverage structure that consists of "ideal hinges", i.e. no moment nor bending motion is allowed at the hinges. In an leverage design, hinges are made of flexible flexures and they direct the motion by the their own bending movement. As a consequence, the bending motion of the hinges offsets the location of the ideal center of rotation, which is presumably stationary in an "ideal hinge" [69]. This motion is particularly important when it takes place at the middle hinge of our leverage structure because this middle hinge is the pivot point of the rotation motion of the magnetic head. The pivot point moves during the PZT actuation and, as a consequence, the in-plane slider motion becomes the composition of rotation and translation, rather than a pure rotation motion. The displacement of the magnetic head cannot be precisely predicted by the movement of the PZT strips, as discussed before. The translation of the pivot point depends on the magnitude of the input stroke. This translation affects the effective displacement-amplification factor of the leverage structure to PZT input stroke, making it slightly nonlinear.

One possible solution to minimize the translation movement of the pivot point is to increase the stiffness of the middle hinge, so that it can hold the pivot point in place. In our design, we choose the length of the hinges to be 200 μm for the hinges located on the two sides of the suspension and 50 μm for the hinge in the middle of the suspension.

The in-plane bending stiffness of the leverage structure was estimated, with the dimensions of hinges discussed above, using simple beam deflection theory. The calculation showed that the in-plane bending stiffness of the leverage structure is around 1×10^7 N/m, resulting in a sway resonant frequency of 400 KHz in an abbreviated system that only consists of a leverage structure and a picoslider. However, our design requirements specified a slightly larger than 20 KHz, as discussed in section 3.2.3, for the sway resonant frequency in that abbreviated system. These simulation results indicate that the dimension of the hinges set the out-of-plane bending stiffness in the range of the requirement (the requirement of the maximum stress concentration due to the preload), but the resulting in-plane bending stiffness is much higher than our design goal.

3.2.4 Hinge design: High-aspect-ratio flexures

Fig. 3.13 illustrates two different cantilever structures that are assumed to have the same width, i.e. the width of the plate (on the left of the picture) equals to the sum of widths in the parallel-flexures structure (on the right of the picture). We will compare bending stiffnesses in Y and Z directions between these two structures.

For a plate subject to a point force at its free end, its deformation can be described by a centerline deflection and a plate warping along its centerline. Moreover, the amount the

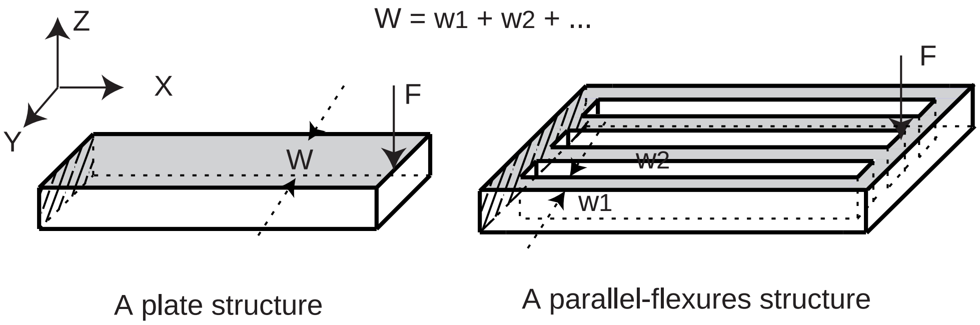

Figure 3.13: Bending stiffnesses of parallel-flexures vs. plate structures

centerline deflection can be predicted accurately by simple beam bending theory [59]. Based on the assertions above, the out-of-plane (z-direction) bending stiffness of two structures in Fig. 3.13 are roughly the same if the sum of the width in a parallel-flexures structure is equal to the width of a plate. Moreover, from beam bending theory, the ratio of in-plane vs. out-of-plane bending stiffnesses is proportional to $(\text{width/height})^2$. Therefore, by using the hinge structures that consist of many high aspect ratio flexures, instead of a wide plate, the overall in-plane bending stiffness is reduced while preserving the same amount of out-of-plane bending stiffness. In our hinge structures design, we spread out the total area 90 μm into 9 flexures, each of them is 10 μm wide. The in-plane bending stiffness is reduced by 81 fold while the out-of-plane bending stiffness stays the same.

There are other advantages of using high aspect ratio flexures instead of a wide plank. Researches have shown that the fracture strength of the micro-machined single crystal silicon depends on the dimensions of its cross-section. According to the references [50] [18], the fracture strength of single crystal silicon approaches its highest value 7 GPa (in the case that there is no defects present in a single crystal silicon) as the cross section of the structure gets smaller.

The dimensions of 3 sets of flexures are listed in Table 3.3.

	Side flexures	Middle flexures	Side flexures
Number of flexures	9	7	9
Length (μm)	200	50	200
Width (μm)	10	10	10
Gap between flexures (μm)	14	14	14
Height (μm)	80	80	80

Table 3.3: Flexures dimensions of the leverage structure

3.3 Stretch Area

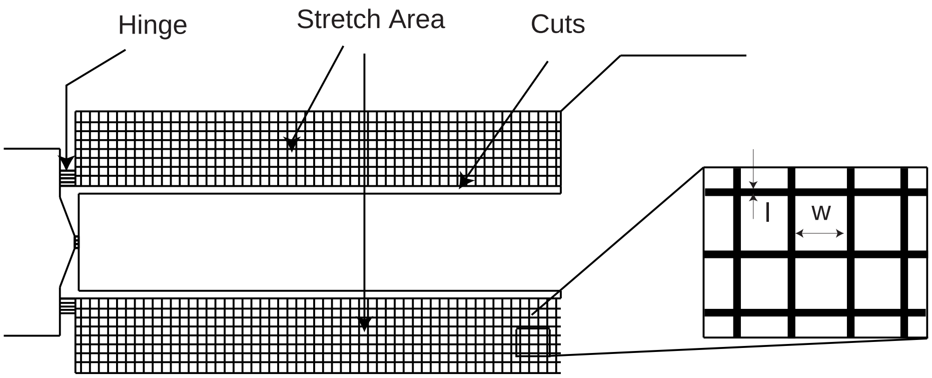

Figure 3.14: The schematic of the stretch area

The stretch area is the location in the suspension where the PZT actuation strips are attached. Deep trenches that cut all the way through the suspension define it. These cuts allow the PZT strips to stretch in a push-pull motion, without twisting the entire suspension. Inside this area, the suspension consists of very sparse grids, as shown in Fig. 3.14. The equivalent Young's modulus of the grid structure is proportional to the ratio of the rib width (l) over the opening width (w) [32]. Thus, by manipulating the ratio l/w, the equivalent Young's modulus of this area can be made less than that of the remaining sections of the silicon suspension. This structure was designed so that driving voltage on the PZT strips can be lowered significantly, without reducing the bending or torsional stiffness of the overall suspension, in order to meet other performance requirements.

As mentioned at the beginning of this chapter, the secondary actuation force is generated by 4 pieces PZT strips, which are glued to the silicon suspension, and then transmitted to the magnetic head through the motion components that were implemented on the silicon suspension. Here, we quantitatively examined the distribution of the actuation force in order to design the "stretch area" on a silicon suspension properly and thus efficiently lower the PZT actuation voltage.

The calculation results indicate that several mini-Newtons of force are needed to produce a ±1 μm oscillatory motion at 2 KHz, of the magnetic head located at the end of the picoslider with a mass of 1.6 mg. Moreover, the force needed to flex the flexures of the leverage structure is on the level of tens of mini-Newtons, and 20 Volts on four pieces of PZT strips can produce a force of about 0.7 Newton. From the calculation results above, it can be seen that the force that is utilized to move the magnetic head and bend the flexures is only a small fraction of the total force generated by PZT actuators. This observation indicates that the major portion of force, that is produced by the applying voltage on PZT strips, is utilized for the deformation of PZT itself and for stretching the material that PZT strips are attached to.

An FEM simulation was done to precisely quantize how the PZT actuation force is transmitted by the "stretch area" and hinge structure into a slider rotation. The structures modeled in this simulation included: four pieces of PZT strips, each 127 μm thick, silicon suspension 80 μm thick, magnetic head (picoslider) and 50 μm of epoxy in between PZT and the silicon suspension. The sandwiched structure of our PZT actuated silicon suspension has been briefly described at the beginning of this chapter and its detailed assembly process can be found in the next chapter. Without losing much accuracy, the "stretch area" on the silicon suspension was modeled as a solid piece of material which had an equivalent Young's modulus and density, instead of modeling it as a grid structure made of silicon. The design variable in the FEM simulation was the various equivalent Young's modulus/density of the "stretch area". The goal of the simulation was to determine the PZT actuation voltage that is required to move the magnetic head 1 μm statically from its equilibrium position. The simulation results were plotted in Fig. 3.15.

In Fig. 3.15, the equivalent Young's modulus of the stretch area is represented as the ratio of the Young's modulus of single crystal silicon to the equivalent Young's modulus of the "stretch area". Note that, the larger number in the horizontal axis in the plot implies that the stretch area is softer. As shown in the plot, the PZT driving voltage decreases as the equivalent Young's modulus of the stretch area decreases. The results in Fig. 3.15 indicate that the PZT driving voltage cannot be lower than 17 Volts, even if the equivalent Young's modulus of the stretch area is smaller than 1/10 of the Young's modulus of single crystal silicon. This saturation indicates that, in this regime, the portion of the PZT actuation force that is utilized to stretch the "stretch area" is negligible and almost all of the 17 Volts of PZT actuation voltage utilized to deform the PZT strips. In the extreme case where the

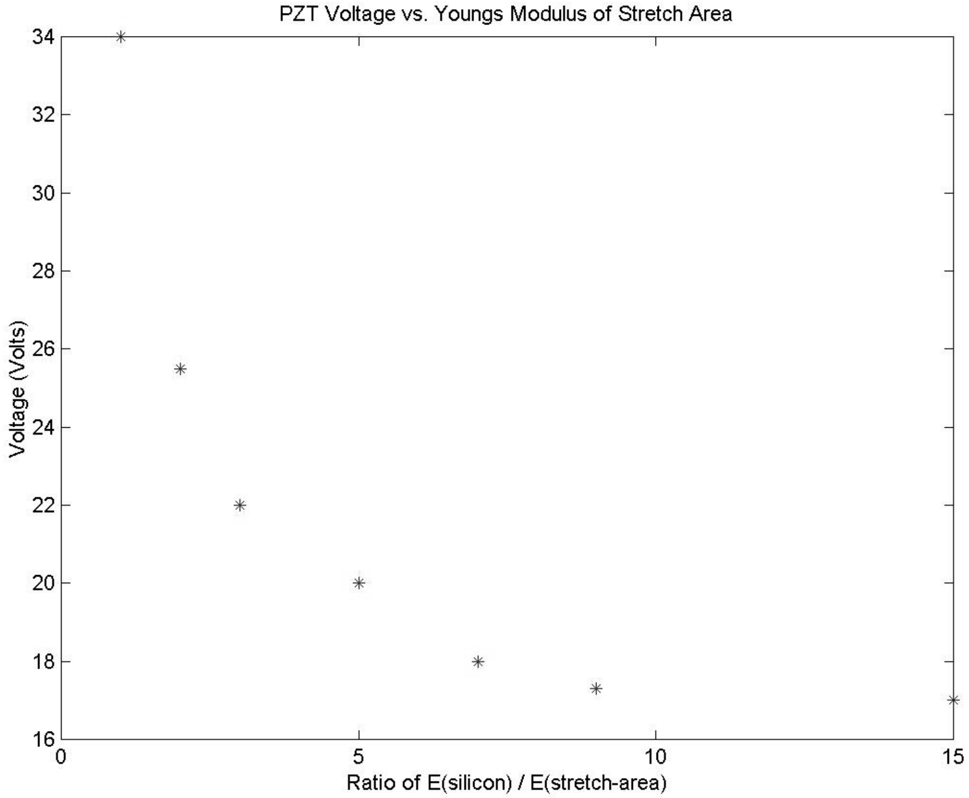

Figure 3.15: PZT driving voltage with different equivalent Young's modulus/density of the stretch area

equivalent Young's modulus of the stretch area is the same as of the single crystal silicon, the PZT actuation voltage that is used to move the head 1 μm is 34 Volts. This observation indicates that, at least, 17 Volts of additional PZT driving voltage would be needed just to deform the suspension if a ”stretch area” design was not implemented on the suspension. These results illustrate the importance of incorporating a ”stretch area” in the suspension design, in order to lower the PZT driving voltage.

The dimensions of the ”stretch area” design in the silicon suspension are 6.5 mm× 1 mm, which are the same as the dimensions of the PZT strips that were attached to the suspension. We designed two types of the grid structure for the ”stretch area”. The l/w

values (as shown in the Fig. 3.14) of these two designs were are 1/5 and 1/3, respectively, and the expected PZT actuation voltage for the 1 μm head displacement is 20 Volts and 22 Volts, respectively.

3.4 Piezoresistive Relative-Position-Error-Signal Sensors

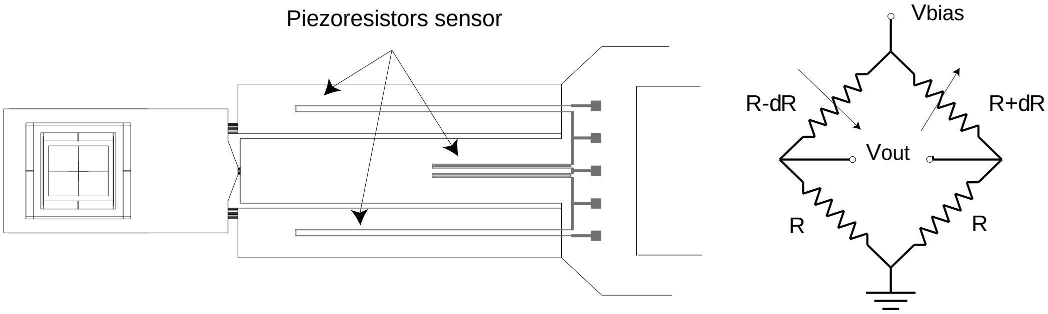

Figure 3.16: The schematic of the piezoresistors sensor

As mentioned in Chapter 1, the relative position error signal can be used to construct an MIMO controller that will damp out the secondary actuator's resonance modes and enhance the overall robustness of the dual-stage servo system. Although the importance of RPES is obvious, it is difficult to incorporate a position sensor on a suspension to attain RPES without interfering with the suspension resonances. Thus no current PZT-actuated suspension designs have the RPES sensing capability. In our silicon suspension design, we utilized a thin piezoresistive film on the suspension which is highly sensitive to the suspension deformation. Currently, this piezoresistive sensor was used to sense the suspension strain, which is generated by the PZT stretch, for attaining RPES. This piezoresistive film may also be utilized for sensing suspension vibration when it is excited by air flow in the HDD system, which has become an important research topic in recent years.

Boron doped polysilicon film was in-situ deposited and patterned both in the "stretch area" and in the center of the suspension, which is not expected to stretch, in order to form a Wheatstone resistor bridge. These four resistors are situated symmetrically along the centerline of the suspension to annul the noise signal generated by the suspension bending and twisting and minimize the temperature effect on the effective gauge factor of piezoresistive sensors. The resistors bridge produces a voltage signal that is primarily linearly proportional to the amount of stretch produced by the PZT strips. Due to the fact that the leverage, which converts the push-pull motion of PZT into the radial displacement of head assembly, is relatively rigid in-plane bending stiffness (its natural frequency is about 50 KHz), the head displacement produced by PZT actuators (RPES) can be obtained using the displacement-amplification factor S in Eqs. (3.2) and the gauge factor K in Eq. (1.1).

$$\begin{aligned} V_{out} &= \frac{\delta R}{2R} V_{bias} \\ &= \frac{K\epsilon}{2} V_{bias} \\ &= \frac{V_{bias}}{2l_{pzt}} \frac{K}{S} \cdot D \end{aligned} \tag{3.5}$$

where l_{pzt} is the length of PZT strip and D is the displacement of the magnetic head. In our design, the factor ($V_{bias}/2l_{pzt} \times K/S$) is predicted to yield a gain of 3.3 mVolts/ μm.

3.4.1 Noise analysis

To predict the resolution of the piezoresistive sensors, two types of noise, Johnson noise and shot noise, were taken into consideration. Both are assumed to be white and Gaussian noise and considered to be the two most significant noise signal in electronic devices. The expressions to calculate these two types of noise can be found in many textbooks [16].

Johnson noise: Any resistor sitting on the table (open-circuit) would generate a voltage across its two terminals. This voltage is known as Johnson noise and it can be estimated by the following equation:

$$V_{n1}(rms) = \sqrt{4KTRB}$$

where V_{n1} has the unit of V/ Hz$^{1/2}$, K is Boltzmann's constant, T is the absolute temperature in degrees Kelvin, B is the bandwidth in hertz and R is the total resistance of the piezoresistors bridge.

Shot noise: An electric current is the flow of discrete electric charges, not a smooth fluid-like flow. From the quantum physics viewpoint, the finiteness of the charge results in the statically fluctuation of the current. This current is estimated by the following equation:

$$\begin{aligned} I_{n2} &= \sqrt{2qI_{dc}B} \\ V_{n2} &= I_{n2} \cdot R \end{aligned}$$

where q is the electron charge, I_{dc} is the current due to the bias voltage of the piezoresistors bridge and V_{n2} is the noise-voltage (V/ Hz$^{1/2}$) due to the current fluctuation.

Therefore, the sensing noise due to the Johnson noise and Shot noise is,

$$V_{noise} = \left(V_{n1}^2 + V_{n2}^2\right)^{1/2}$$

This noise-voltage can be converted into an equivalent magnetic head displacement measurement noise, by applying Eq. (3.5) and the resolution of the sensor can be obtained. A simulation was performed to determine the sensing resolution due to these two types of noise, and the results are shown in Fig. 3.17. The displacement measurement resolution is plotted as a function of the overall resistance of the piezoresistors bridge. The resolution decreases as the resistance of the bridge increases, and the resolution is around 35 nm when the resistance is 150 KΩ.

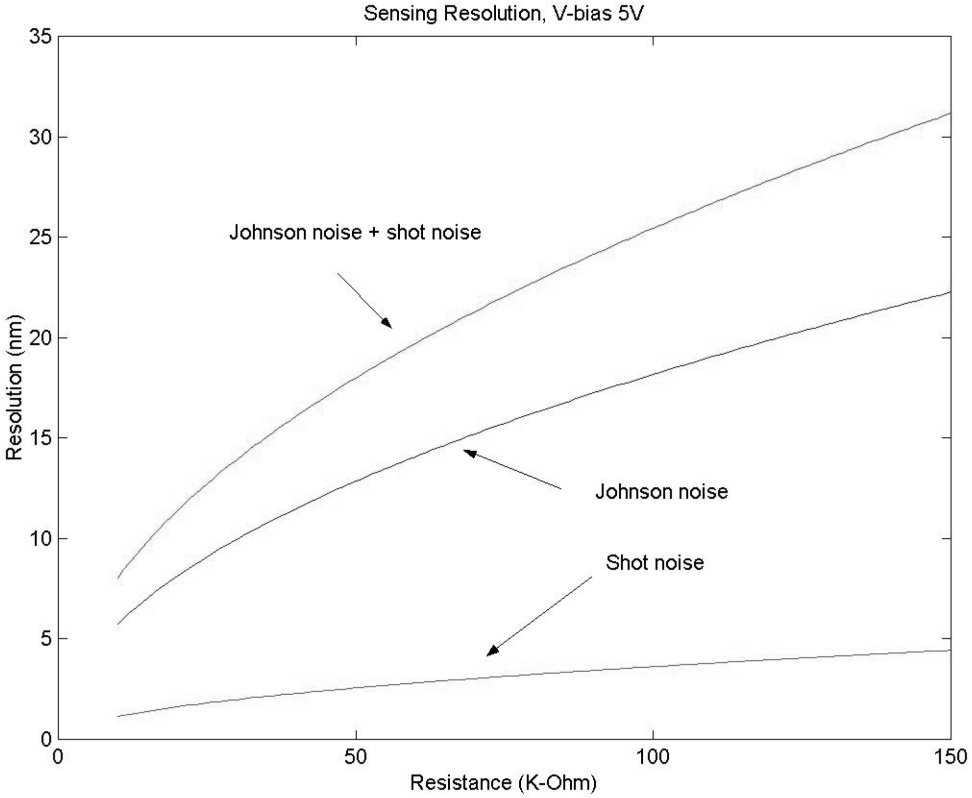

Figure 3.17: The sensing resolution of the piezoresistors sensor

The sensing error induced by the temperature variation, although it is important, was not modeled in the simulation above. The symmetry of the Wheatstone bridge cancels most of the resistance variation due to temperature effect, except for the TCGF (Temperature Coefficient of Gauge Factor). Literature [13] [46] shows that the TCGF of boron doped polysilicon is between –0.1% / $°C$ ∼ –0.2% / $°C$. This gauge factor variation would contribute significantly to the sensing error in the case that the operating temperature in a disk drive varied largely. The observed fact is that although the temperature does increase ($\sim 15°C$) after the drive warms up, it does not fluctuate significantly during its operation. One solution to this problem is to correct this slow-drifting sensing error with the PES in real time.

Each piezoresistor is 11.2 mm long; 10 μm wide and 1.5 μm thick. The resistivity of the boron doped polysilicon film is expected to be $1.65\times10^{-2}\Omega - cm$. The resistance of each piezoresistor, which is same as the overall resistance of the piezoresistors bridge, is 130 KΩ. The sensing resolution of this 130 KΩ piezoresistor sensor is expected to be 30 nm, according to Fig. 3.17.

3.5 Electrical Interconnects

As discussed in Chapter 1, two types of electrical interconnects have been widely utilized in the current HDDs: flexible cable and in-situ patterned metal leads. In our silicon suspension design, we chose the in-situ-metal-leads approach to implement the electrical interconnects.

As shown in Fig. 3.18, four metal leads start from the center coupon of the gimbal structure, passing through the gimbal's torsion bars and suspension's hinge structure, and end close to the base of the suspension.

Current HDD data transfer requirements specify that the electrical interconnects

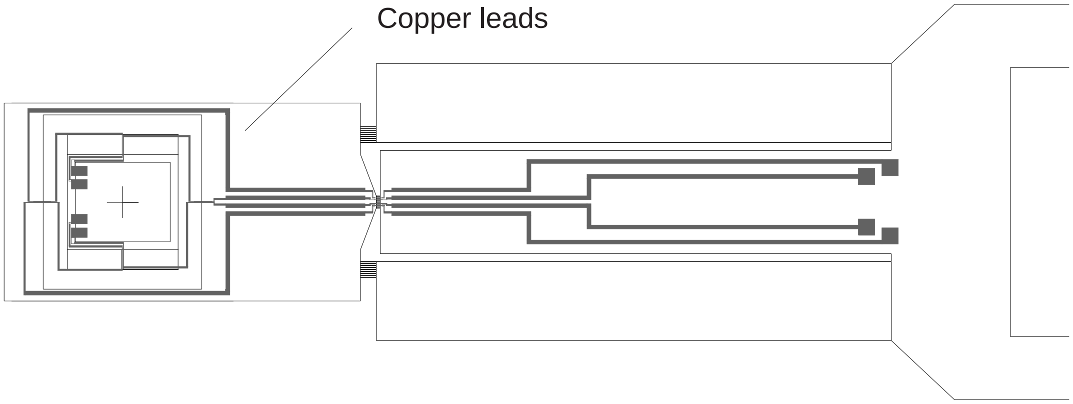

Figure 3.18: The layout of electrical interconnects on the suspension

must be capable of transferring data at relative high speed (for example, several hundred Mbit/s). To achieve this goal, the electronic components that participate in read/write data actions have to be taken into account and analyzed as a whole system. These include the electrical properties of the interconnects, MR head and the differential amplifier [68] [57] [26]. A simplified circuit model that can predict the transmission time for the read/write actions is shown in Fig. 3.19. In the circuit, LL and RL are respectively the inductance and resistance of each metal lead that connects the MR head to the differential amplifier. CLS is the capacitance between metal lead interconnects and the suspension, which acts as the voltage ground of the circuit. CLL is the capacitance between two metal leads. The electrical properties of the MR head are $LH = 45\ nH, CH = 1\ pF, RH = 10\ \Omega$, respectively. More details of this model can be found in reference [26]. Because the transmission time involves parameters other than interconnects on the suspension, the design of the interconnects cannot based on the simulation results of the circuitry shown in Fig. 3.19. Instead, the design goal is to ensure that the transmission delay resulting from interconnects is less than the transition time of the MR head. Due to the fact that the "write" action requires a longer period than the "read" action for the MR head, the design criterion is the current settle-time during the "write" action. The transition time for the current to settle is about 2.15 ns for the MR head. Therefore, the time constant of $(L \cdot C)^{0.5}$ of the electrical interconnects must be designed to be less than 2.15 ns [47]. This requires small capacitances and inductances in the metal leads.

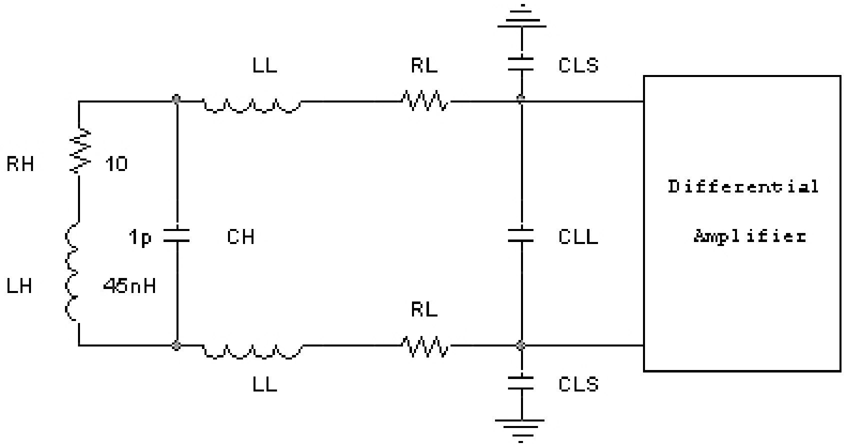

Figure 3.19: Circuit diagram for the data transfer

3.5.1 Resistance, capacitance and inductance

To minimize the overall resistance of the interconnects, copper film was chosen for its high conductivity. The width of the interconnects is also maximized, over the limited space of the suspension structure, as part of the effort in lowering the overall resistance. The metal leads must be inevitably laid through narrowed width areas, such as the gimbal's torsion bars and the suspension's hinge structures, in order to transfer data between the magnetic head and the differential amplifier. These structures are only 10 μm wide. As a consequence, the width of the metal leads, laying on top of these structures, is limited to 4 μm due to limitation in the fabrication process reliability. The resistance of the metal leads at these critical areas takes up 1/3 of the overall resistance of the interconnects. This design constraint hampers the effort in lowering the resistance of interconnects. The thickness of this copper film was determined by achieving a 5 Ω resistance for each interconnect, in order to be compatible with the HTI TSA series suspensions. A simple expression was used to characterize the resistance of metal leads from their dimensions.

$$R = \rho t \frac{l}{w}$$

where R is the resistance, ρ is the resistivity of the material, t, l and w are the thickness, length and width of the metal leads respectively.

The capacitance of the electrical interconnects includes the capacitance from metal leads to the suspension (CLS shown in the Fig. 3.19) and the capacitance between two metal leads (CLL shown in the Fig. 3.19). CLS can be estimated by the simple expression,

$$C = \epsilon \frac{A}{d}$$

where, d is the thickness of isolation layer (silicon nitride, $\epsilon_r = 7.5$), A is the area of the metal leads and ϵ is the permittivity of the isolation layer. In this design case, the thickness of the nitride isolation layer was 0.5 μm and the area of one metal lead was $6.8 \times 10^5 \mu\text{m}^2$. The resultant CLS is estimated to be 90 pF. CLL consists of two major components due to the multiple electron flow paths. The first electron flow path goes vertically: the metal line $\longrightarrow$ isolation layer $\longrightarrow$ suspension $\longrightarrow$ isolation layer $\longrightarrow$ metal line. The capacitance for this electron path was estimated to be $0.5 \times CLS$. The second path goes horizontally: metal line $\longrightarrow$ isolation layer $\longrightarrow$ metal line. The capacitance of the second path strongly depends on the layout of the metal leads, and is thus difficult to estimate. Due to the existence of multiple electron path, CLL was estimated to be larger than $0.5 \times CLS$.

The estimation of the inductance of the metal leads is also difficult. For two wires parallel to each other, the mutual inductance is inversely proportional to the distance between the wires [33]. The inductance of this interconnect design is expected to be much higher than that of the commercial product due to the tiny distance ($\sim 3\ \mu$m) between leads at the gimbal torsion bars and suspension hinges location. The layout of the interconnects in our suspension design can be modeled as parallel wires which have multiple sections of different cross-sectional dimensions. Moreover, the gap in between these two wires also varies from 3 μm to 140 μm, depending on the sections of the suspension where they are laid out. As a consequence, this layout presents the possibility of multiple modes in the data transmission characteristics.

The dimensions for each of the metal lines are: height $t = 2\ \mu$m, length/width $l/w = 670$. The resistivity ρ of the deposited copper film is $1.7 \times 10^{-8}\Omega$-m. The resulting resistance of each interconnect is expected to be 5.7 Ohm. The equivalent CLL and LL were obtained experimentally and the results will be discussed in Section 5.5 of Chapter 5. Detailed dimensions of the metal lines are listed in Table 3.4.

Width / Length	50 μm	40 μm	20 μm	15 μm	10 μm	4 μm
Metal line # 1	11810 μm		3712 μm	275 μm	204 μm	735 μm
Metal line # 2	7917 μm	80 μm	2566 μm		146 μm	698 μm

Table 3.4: Metal lines dimensions for the electrical interconnects

3.6 FEM Simulation

The importance of having a suspension preload to counter act the air bearing lift during the operation of the HDD has been discussed in Chapter 1. Two methods of providing preload in silicon suspensions are possible. The first is to glue the silicon suspension to the pre-cut steel suspension, and the second is to load the suspension directly on the E-block at an angle. As the first approach is easier to implement on current HDDs and is easier to be tested with current testing equipments than the second approach, the first approach was adopted in our suspension design. The second approach, although it is currently harder to be implemented in existing HDDs, is probably the preferred approach, since it has the advantage of reducing the assembly steps during manufacturing. Two silicon suspensions, each of which with a geometry that is suitable for each of the preload configuration, were designed. They were both analyzed by FEM simulation using ANSYS. The simulation results of each design are listed together, along with a commercial product TSA2030, for comparison. To avoid confusion, the discussion on the ”silicon suspension” focuses on/ refers to the suspension with its main body made of silicon and attached to a steel piece, which has a pre-bend, if not otherwise specified.

The materials that were modeled in this simulation include silicon, epoxy, slider, PZT and steel. Their dimensions have been discussed in the previous sections and their corresponding material properties, which utilized in this simulation, are listed in the Table 3.5.

In the ANSYS simulator, the FEM elements solid73 and solid5 were both utilized for modeling the 3D structure. Additionally, solid5 has the capability of modeling piezoelectric material. FEM elements shell93 and shell91 are utilized for modeling the 2D structure;

shell93 is particular useful in modeling the 2D structure that consists of multiple layers.

	Young's Modulus (N/m^2)	Density (Kg/m^3)	FEM element
Silicon	190×10^9	2328	shell93/shell91
Steel	193×10^9	8030	shell93/shell91
PZT	6.2×10^{10}	7800	solid5
Slider	412×10^{10}	4250	solid73
Epoxy	3×10^9	1100	shell91

Table 3.5: Material properties in the FEM simulation

3.6.1 Static response

Due to many sandwiched structures in our silicon suspension design, in this FEM simulation the steel and the main body of the suspension were modeled as shell/multiple-layers shell components, depending on the structure of the suspension, and the PZT strips and slider were modeled as 3D solid components. In some instances, the results of the FEM simulation are not accurate when 3D elements and 2D elements are connected to each other directly. The alternatives to this problem include modeling all structures with 3D elements, and using intermediate elements between 2D and 3D elements. For this simulation, we tried the second approach. The 2D elements and 3D elements were tied together with very rigid 1D beam element. The simulation results obtained in this way closely match the results obtained from the approach of connecting 2D and 3D elements directly. Therefore, in the following simulations, we adopt the approach that connects 2D and 3D elements directly to avoid a large/complicate FEM model.

The boundary conditions set in this model include the 2 gram load on the picoslider and the 20 Volts applied to four pieces of PZT strips. However, the air bearing lift, which acts on the slider when it flies on the disk, was not modeled. The resulting FEM simulations predicted that the magnetic head can be positioned 1 μm statically with 20 Volts applied to the PZT strips. The maximum stress and strain takes place at the hinge structure. The stress is 0.35 GPa calculated by Von-Mises method [3]. The maximum stress is one order of magnitude below the fracture strength of micromachined single crystal silicon (2–7 GPa [50]). The suspension deformation and the location of maximum stress are shown in the Fig. 3.20.

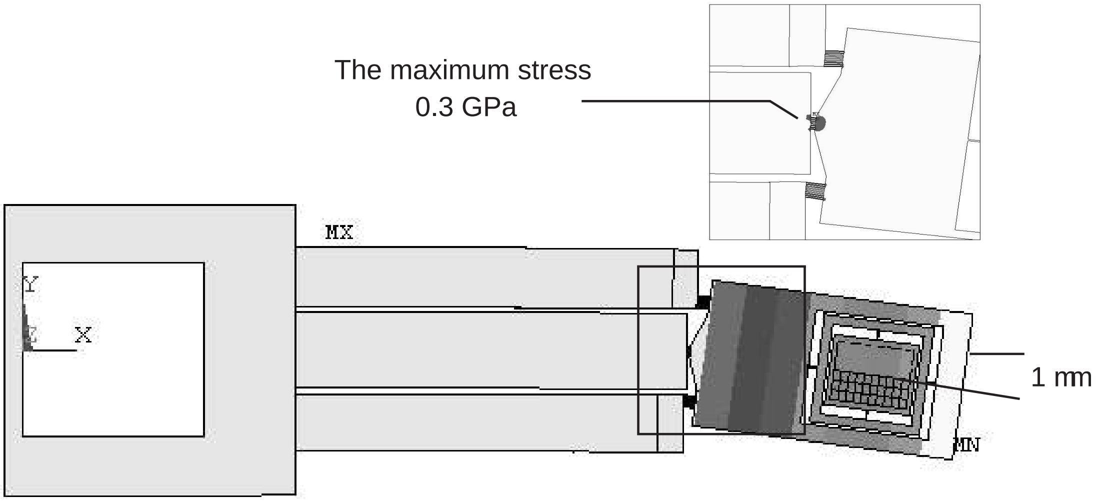

Figure 3.20: FEM simulation: 20 Volts on PZT and 2 gram load on the picoslider

3.6.2 Dynamic response

In this simulation, all the structures are modeled as shell/multiple-layers shell, except for the picoslider. The simulation results of this approach agrees with the results obtained from solid/shell model, and its numerical solution converges faster than the solid/shell model. Therefore, it was adopted to determine the resonant modes of the silicon suspension. Table 3.6 shows the resonant frequencies of the silicon suspension and compares them with a commercial TSA2030 steel suspension. The "silicon-steel suspension" listed in the table is the silicon suspension that was glue to a pre-bent steel suspension, the "all-silicon suspension" doesn't have any steel part and is supposed to be attached, at an angle, directly to the E-block. In this silicon suspension simulation, the gimbal structure, in both of the silicon suspension designs, has double-flexure torsion bar and it has the same dimensions as discussed in the previous sections.

	Silicon-steel suspension	All-silicon suspension	TSA2030
Spring constant (1st Bend)	20 N/m (240 Hz)	18.4 N/m (217 Hz)	14.7 N/m
2nd Bend	2402 Hz	2016 Hz	1640 Hz
3rd Bend	4514 Hz	4224 Hz	
1st Torsion	2638 Hz	1765 Hz	2720 Hz
2nd Torsion	7639 Hz	7525 Hz	6500 Hz
Gimbal Roll	1817 Hz	2019 Hz	0.99 μN m/deg
Gimbal Pitch	2088 Hz	2336 Hz	1.25 μN m/deg
Gimbal In-Plane	9032 Hz	8399 Hz	
1st Sway	10216 Hz	9679 Hz	10900 Hz

Table 3.6: FEM results of silicon suspensions

According to the simulation results, the first torsion resonance of the suspension is due to the slender structure which is located between the PZT strips and the E-block pivot point. For the silicon-steel suspension, this resonant mode is about 2.6 kHz and is expected to be the first resonance encountered by the VCM section of the dual-stage servo. For the all-silicon suspension, it is 1.7 KHz, which is much softer than that of the TSA2030. This is because of the same structure in the all-silicon suspension was designed to match the "spring constant" with the commercial product, thus resulting in a softer torsion stiffness. The 2nd torsion mode is about 7.6 kHz and is due to the two "stretch area" moving up and down with 180° phase difference. The asymmetry of the PZT actuation, due to fabrication/assembly process, produces an out-of-plane bending motion. This bending motion is confined by the push-pull actuation scheme and is likely to excite the 2nd torsion resonance. Therefore, this mode is predicted to be the first resonance of the PZT actuation and may limit the overall bandwidth of the dual-stage servo system. The 2nd resonance for the VCM actuation is the suspension sway motion. It is about 10 KHz, which is similar to that of the commercial product.

The resonance result for gimbal structure in Table 3.6 are different from the results shown in Table 3.2. This is due to the different boundary conditions in the two FEM simulations.

3.6.3 Frequency response

The frequency response of the PZT-actuated silicon suspension were estimated from the FEM in order to determine the influence of each resonance on the motion of the magnetic head. The resulting transfer functions can be used to design the compensators for the dual-stage servo. Two frequency responses were simulated. The first simulates the frequency response of the magnetic head motion to an input force generated by the VCM. The second simulates the response of the head to PZT actuation.

In the simulation for VCM actuation, a unit force along the y-direction (the magnetic head moving direction) is applied at the E-block. At the same location (E-block), displacement constraints were applied to freeze the motion of E-block on the x and z directions. This setup allows only y-direction displacement at E-block due to the unit force, and is utilized to model the VCM actuation. The damping ratio is chosen by experience to be 0.01. The frequency response is plotted as the gain (in dB) and phase (in Degree) of magnetic head displacement over E-block displacement vs. frequency. The results are shown in Fig. 3.21.

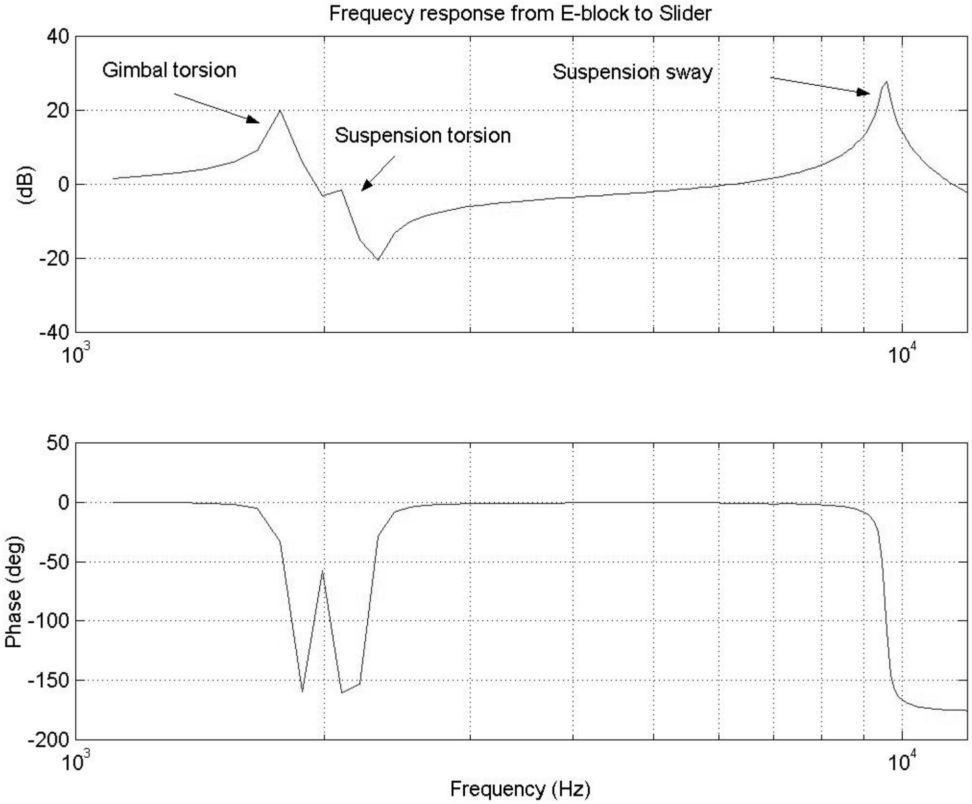

Figure 3.21: Frequency response of the suspension from E-block to the magnetic head

As shown in the plot, the first resonant mode is around 1.77 KHz. This mode is the gimbal-roll motion as confirmed by the FEM simulation results in Table 3.6. The slight frequency shift of the resonance between two simulations, is due to the damping ratio. This gimbal torsion resonance is not expected to appear in an actual disk drive operation, where the combination of preload and air-bearing lift force act on the gimbal structure to constraint its motion. The second resonance is the torsion motion of the suspension (2.1 KHz). The last resonance is the suspension sway mode (9.58 KHz). This resonance is identified as a sway mode by its phase plot. The phase of a sway mode drops at the resonant frequency and stays there, unlike a torsion mode which the phase jumps right back up. The resonant frequencies for the suspension torsion and sway modes obtained in this simulation are not close to the frequencies obtained in the previous simulation. The discrepancy can be attributed to the different boundary condition in the two simulations. A supplementary FEM simulation showed that the resonant frequency drops to 1.8 KHz and 9.6 KHz for the suspension torsion and sway modes, respectively, when the displacement constraint along y-direction is released at E-block.

In the frequency response simulation for the PZT actuation, the E-block is fixed in all directions and 20 Volts are applied to the four pieces of PZT strips. Damping ratio is set to be 0.01. The thickness of PZT strips are 137 μm on the top and 117 μm at the bottom. This setup mimics the asymmetry of PZT actuation in out-of-plane motion. The simulations is performed at every 300 Hz, starting from 1 KHz and ending at 12 KHz. The simulation result is plotted as the magnetic head displacement actuated by PZT driving voltage vs. frequency. The result is shown in Fig. 3.22.

The horizontal line, shown in the gain plot, represents the 1 μm head displacement due to a 20 Volts dc input on the PZT actuators. The second torsion resonance (5.5 KHz) does not appear to be an amplitude spike in the gain plot. This resonance mode can be excited when the PZT actuation forces, generated by four pieces of PZT strips where two pieces were placed on the top of the suspension and the other two pieces were on the bottom of the suspension, are not balanced along out-of-plane direction. As mentioned earlier in this section, we intentionally used different PZT thickness in this simulation in order to emphasize this resonant mode. However, the effect of the second torsion resonance is still

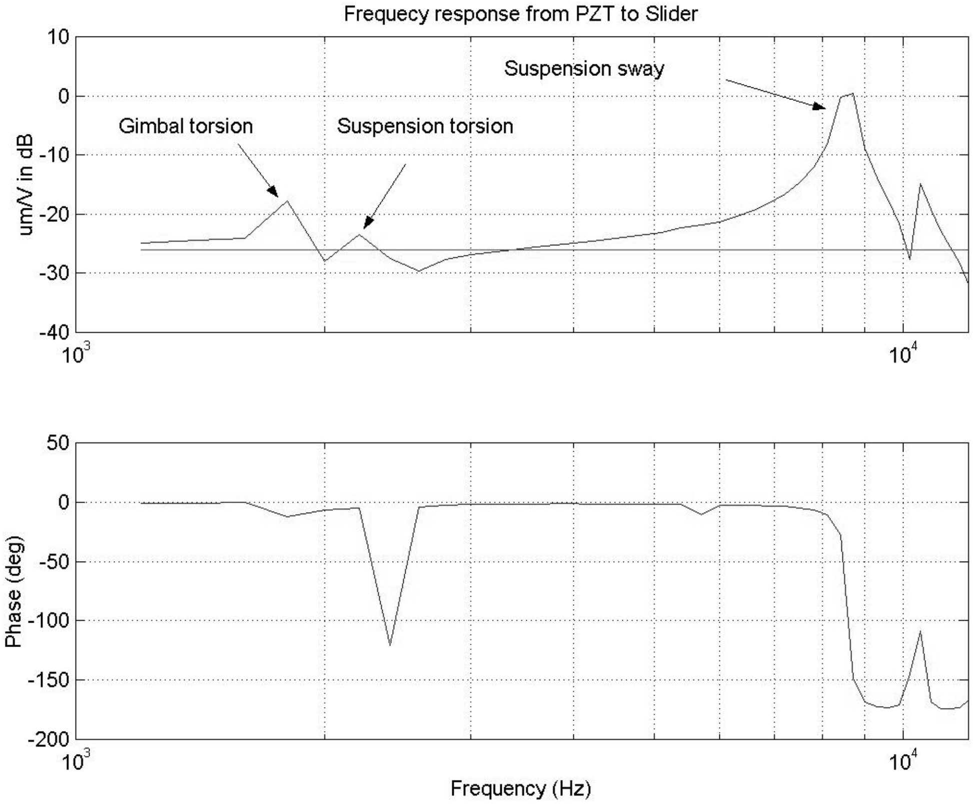

Figure 3.22: Frequency response of the PZT driving voltage to the displacement of the magnetic head

incomprehensible from the simulation results. The possible explanation to this unexpected result could be either not enough of asymmetry in this configuration or a lack of data points (every 300 Hz) in the simulation. The most significant resonance of the PZT actuation is the sway motion from this simulation result.

Chapter 4

Fabrication Process

This chapter discusses the techniques that were utilized to fabricate the silicon suspension described in this dissertation. The fabrication process can be divided into four sections:

1. Piezoresistive film deposition
2. High-aspect-ratio structure micromachining
3. Planarization technique
4. Metallization

Each of these process topics is discussed in detail in the following sections. At the end of this chapter, the complete process flow is listed step by step.

4.1 Piezoresistive Film Deposition

Much research work has been done to study piezoresistivity of polysilicon films [13] [4] [46] [25] [24] [65] [44] [43] [5]. It has been shown that the ”energy band”, grain size and grain boundary are the three key factors in determining the piezoresistivity of a polycrystalline film. Furthermore, large grain size and low trap densities are the key factors to yield high gauge factors in piezoresistive films [13]. These structure properties strongly depend on the film deposition conditions. To yield a high gauge factor in conjunction with a good stability of the piezoresistive polysilicon film, the following process conditions are suggested by references [13] [25] [24].

1. Low LPCVD deposition temperature, $\simeq 560\ ^{\circ}C$
2. Boron implantation, doping concentration $2 \cdot 10^{19} cm^{-3}$
3. RTA (Rapid Thermal Annealing) and high annealing temperature, 1000–1100 $^{\circ}C$

In this film deposition process, undoped polysilicon was deposited at 600 $^{\circ}C$ for 3 hours. The film thickness was measured to be 1.2 μm. Boron atoms were introduced to the film by ion-implantation. The dosage and energy of the ion-implantation were $2.5 \times 10^{15}\ cm^{-2}$ and 150 KeV respectively. 150 KeV of implantation energy injected boron atoms into the silicon subtract up to a depth of 0.5 μm below the surface [21]. After annealing in nitrogen flow at 1050 $^{\circ}C$ for 90 min, the boron doping concentration is expected to be $2 \times 10^{19}\ cm^{-3}$ (dosage/film-thickness $= 2.5 \times 10^{15}/1.2 \times 10^{4}$) throughout the entire film. A high annealing temperature was chosen not only for yielding high gauge factor, but also for increasing the solid solubility of boron doping after the ion-implantation process [39]. The annealing time was determined by the time that the boron atoms can migrate from the surface to the center of the film under the annealing temperature. The resistivity of the film was measured by a 4-point-probe equipment. The resistivity was $1.65\times10^{-2}\Omega$-cm.

Silicon nitride served as the electrical isolation layer between P-type polysilicon film and the N-type single crystal silicon substrate. Typically, thermally grown silicon dioxide has better electrical isolation properties than silicon nitride. In addition, oxide film is more stable and has a very good oxide–silicon interface. As a consequence, it is widely used as a dielectric layer in the IC industry. However, a major drawback is that oxide can't efficiently stop dopants from moving through the film. Dopants from both sides (in this case, phosphorus from the substrate and boron from the polysilicon film) can easily get through the oxide isolation layer and mix with each other during the high temperature annealing process [2] [66] [6] [11] [7] [9]. The second drawback of using silicon dioxide is that the oxide gets etched away quickly by HF (Hydroflouric acid). HF is utilized to release the structure at the end of the fabrication process. Thus it is difficult to incorporate the oxide film in this process. For these reasons, silicon nitride was chosen as the isolation layer material in this process.

4.2 High Aspect Ratio Micromachining

A high aspect ratio structure is the key to the success of the one-piece silicon suspension design. Structures such as the double-flexure torsion bar, hinge structure, etc., are not feasible without a high-aspect ratio fabrication capability. There are many micromachining techniques which can be used to achieve high aspect ratio structure, for example, SOI, HexSil, SCREAM, LIGA and etc. Introductions and comparisons of these techniques can be found in references [38] [23].

As part of this dissertation, a new process was developed to achieve high aspect ratio micromachining. This process is similar to the process based on the use of SOI wafers, but does not require the use of expensive SOI wafers. In this process, the high aspect ratio structure is patterned by the plasma etch on the front side of the silicon. The structure is then released by a KOH etch from the backside of the wafer.

4.2.1 Structure patterning

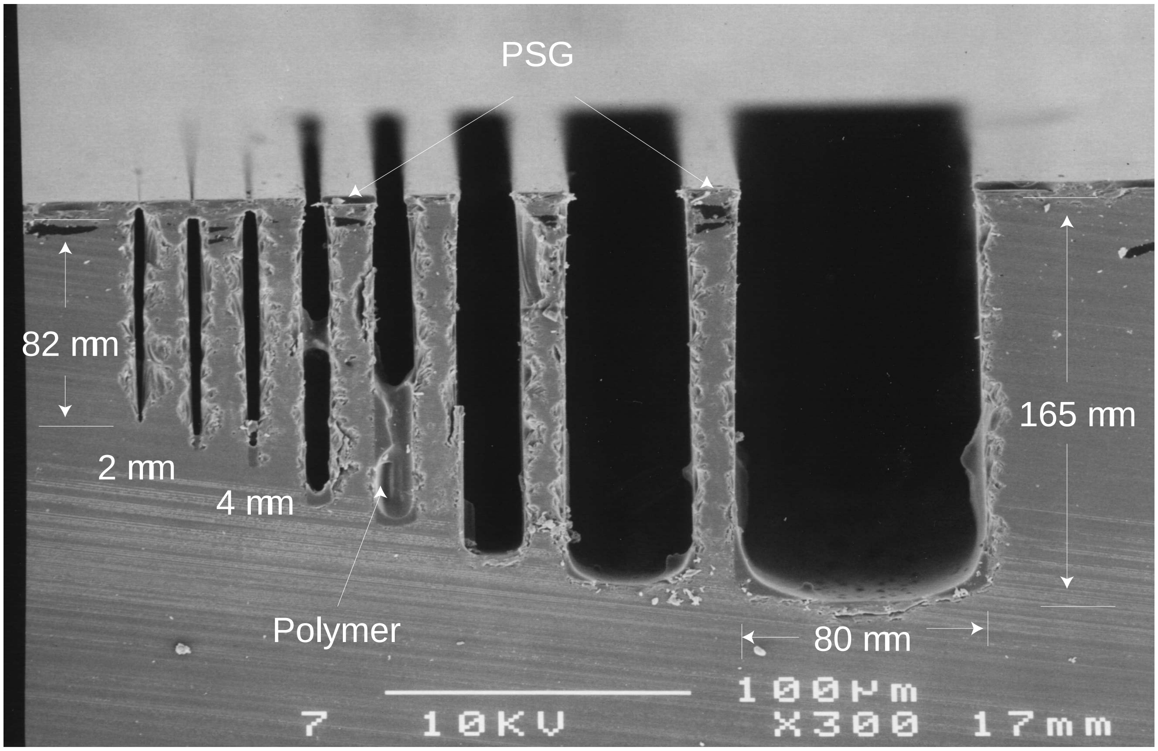

Figure 4.1: STS plasma etch profile. PSG and Polymer in the trenches

The Inductive-Coupled-Plasma (ICP) silicon etcher manufactured by Surface Technology System (STS) was utilized to pattern the high-aspect-ratio structure on the front side of the silicon wafer. The ASE^{TM} process together with an STS machine can easily produce structures with aspect ratio 25 or greater[28] [17].

In the absence of the oxide layer present in SOI wafers, in order to have the same height for the overall structure, all trenches must have the same depth when performing structure patterning etchs. This process objective is not easy to achieve due to the STS machine performance and process limitations. Fig. 4.1 shows the etch profile from STS etch process. In this test, a silicon wafer was first patterned with different sizes of window opening using photoresist, and then exposed to a plasma etch in a STS machine for 45 minutes. Afterwards, a thick layer of PSG (Phosphosilicate Glass) was in-situ deposited and a polymer layer was spun-on subsequently. The PSG layer and polymer layer were deposited for other purposes, which will be explained in Section 4.3. As shown in the figure, the etch depth of the trenches varies from 165 μm to 82 μm, depending on the width of the trenches. In fact, the etch rate not only depends on the size of the opening, but also on the overall area of silicon that is exposed to the etch plasma, although the second factor is not shown in the plot. This is known as "loading effect" [14]. This effect imposes a design requirement for our process that all trench widths on one mask have to be the same, in order to produce the same amount of etch depth and thus the same structure height. This constraint is not necessary in a process that has a buried layer to stop the etch, such as the SOI process. There are other reasons for this design requirement, which will be discussed in the next section.

In the case that different trench width are needed, the procedure shown in Fig. 4.2 can solve this problem, while maintaining the same structure height. In this approach, instead of etching away one big block, narrow trenches are etched along the perimeter of the material that needs to be removed. The middle island will flow away after the structure is released by the back-end etch. By adopting this approach, all different trench widths on the same mask can be converted into one width. As far as the height of the structure is concerned, this perimeter-etch step minimizes the error from "loading effect". However, a

5% etch non-uniformity across the wafer from the etch tool cannot be avoided with this method. This same problem exists in many other high-aspect ratio micromachining methods that have no etch stopper, such as the HexSil process [23] and the SCREAM process [55][29].

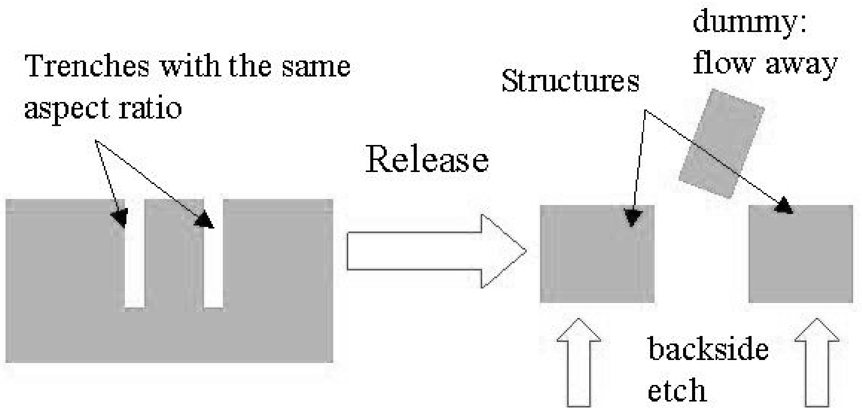

Figure 4.2: Etch scheme, for different trench width.

4.2.2 Structure release

After the front side is patterned, a thin layer of silicon nitride is deposited on the wafer by LPCVD (Low Pressure Chemical Vapor Deposition). LPCVD silicon nitride is conformal and covers steps and sidewalls of deep trenches well; more importantly, it is a very good etch block for KOH. The nitride on the backside of wafer is patterned with windows. The entire wafer is insulated by silicon nitride from KOH attack except for the windows on the backside of the wafer. KOH etches single crystal silicon through the windows roughly at a rate of 1 μm/min. This etch is done when the KOH reaches the bottom of the trenches that were created by plasma etch on the front side of the wafer. Up to this point, the wafer still holds all the structures in one piece by a thin layer of silicon nitride. The final release is done by a concentrated HF solution which etches away the silicon nitride layer, letting the dummy parts flow away.

Due to the non-uniformity of front end trench depth described in Section 4.2.1, the process requires an over-etch by KOH in order to fully release the structure. Because the sidewalls of the trench are protected by silicon nitride, the KOH etch stops at the nitride film and proceeds along the 1-1-1 plane of the single crystal silicon. In the case when a flexure structure is fabricated in the 1-0-0 wafer, where the two sides of the flexure are coated with silicon nitride, the KOH over-etch forms a groove at the bottom of the flexure and stops the etching process, as shown in Fig. 4.3. The angle of the groove is 54.74 °, which is the angle between 1-0-0 plane and 1-1-1 plane of single crystal silicon [49] [53]. Thus, the depth of the groove is determined by the width of the flexure.

4.2.3 Multiple depths

Having a groove pattern on the backside of a structure is not preferred and the presence of grooves should be minimized. However, if grooves can be tolerated, their existence suggests the possibility of doing multiple depths structures using the KOH backside etching technique described above. The devices suitable for this fabrication process should be designed into a special type of structure which comprises of tube-like elements, such as those structures fabricated by HexSil process [23].

As shown in Fig. 4.4, the different heights of the structure are defined by the different trench depths, which can be made by the plasma etch on the front side of the wafer, using either separate etch steps, or different trench widths with one step etch, as

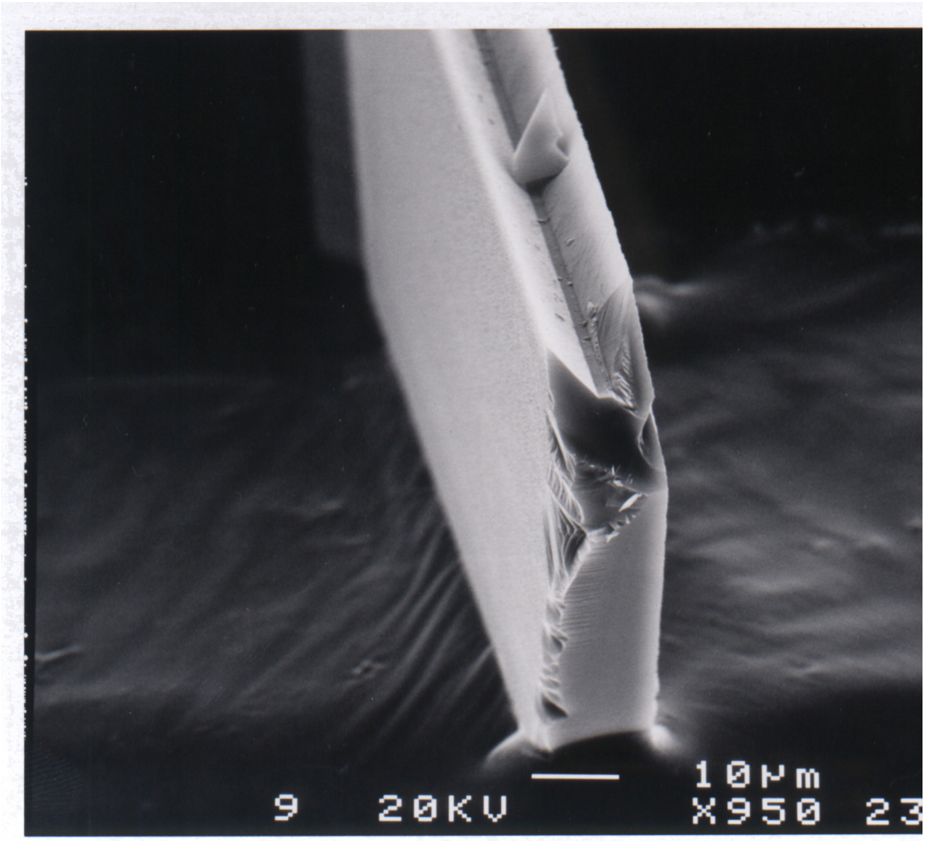

Figure 4.3: KOH release. A photo of a flexure upside-down and the groove is formed by KOH over-etch.

discussed in Section 4.2.1.

During the backside etch process, KOH first reaches the bottoms of the trenches that are adjacent to the taller components in the structure, denoted as "high structure" in Fig. 4.4. Since the bottoms and sidewalls of the trenches are protected by silicon nitride from the KOH etch, KOH stops etching silicon in the "high structure" by forming grooves on the bottom of the "high structure", and thus preserving the taller components in the structure. KOH continues to attack single crystal silicon along 1-1-1 plane in the "transition area", which is the area located between the "high structure" and "low structure", as illustrated in Fig. 4.4. If the designed structure, located in the "transition area", has its height lower

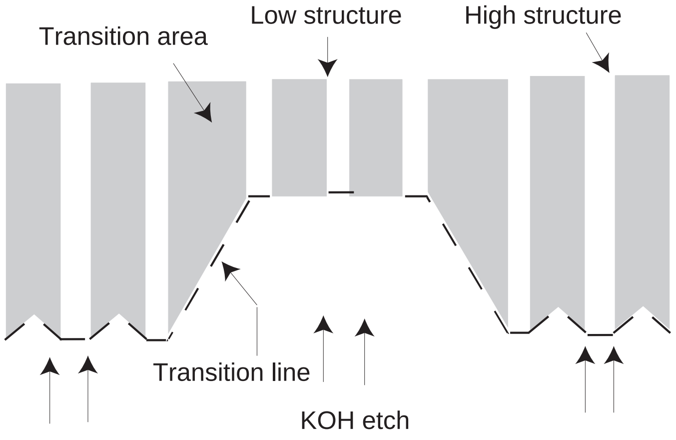

Figure 4.4: Schematics of multiple depth fabrication process

than the transition line set by the adjacent tall-component, the structure will be difficult to release. This imposes design constraints on how suddenly can a structure height occur in a structure.

We have successfully applied this new high-aspect-ratio micromachining technique to fabricate silicon suspensions and other devices such as electrostatic microactuators (Fig. 4.5) and mechanical flip-flops (Fig. 4.6) among others. This process is compatible with most surface micromachining processes. Moreover, it produces high aspect ratio 3D structures, without the necessity of using costly SOI wafers.

4.3 Planarization

In order to minimize equipment contamination, the metallization steps have to be performed after the ICP deep trench etch. However, this arrangement makes fine lithography hard to achieve, due to the bad surface topography that results from the deep trenches

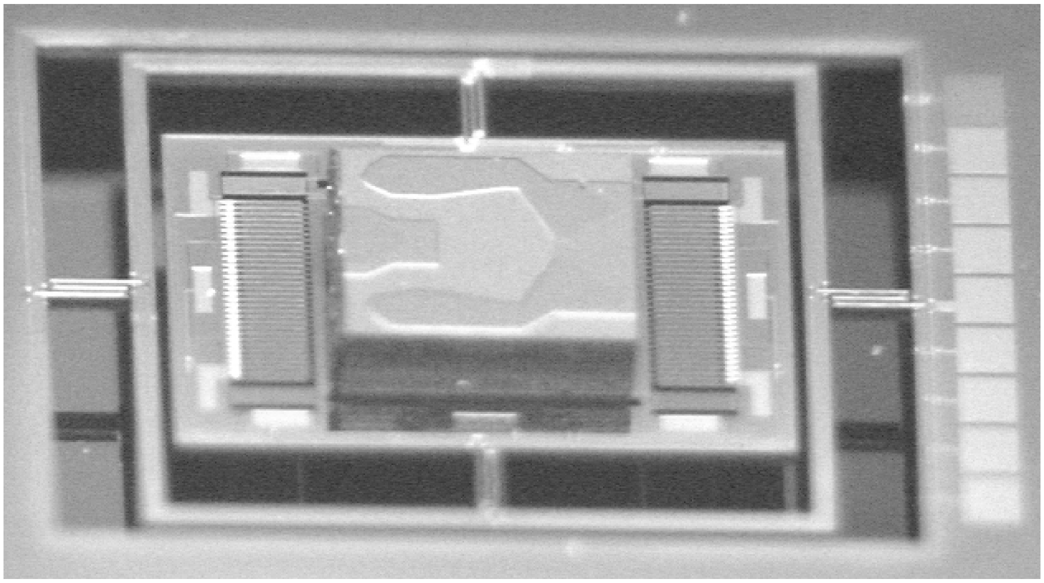

Figure 4.5: Electrostatic microactuator, 80 μm tall, with a picoslider is on top

[70]. A process that can planarize the topography after DRIE needs to be integrated into the suspension making process.

There are many techniques to planarize the surface topography of a wafer. These methods can be characterized in three groups: Sacrificial layer with etch-back, Dielectric deposition and Chemical mechanical polishing [70] [61] [54] [30]. Most of the existing techniques either require delicate deposition equipment (for example, a TEOS system [23] [56]) or have been developed exclusively for the IC (Integrated Circuit) device fabrication. In the IC device fabrication process, the complicated circuitry design requires multiple layers of electrical interconnects. After the first or second layer of electrical interconnects, the formation of narrow trenches appears and degenerates the high resolution lithography. To resume the high lithography quality, the surface needs to be planarized for further process. Typically, the trenches that need to be filled have the dimensions 0.1 μm wide and 1~2 μm deep. This is different from what one encounters in MEMS fabrication. In MEMS fabri-

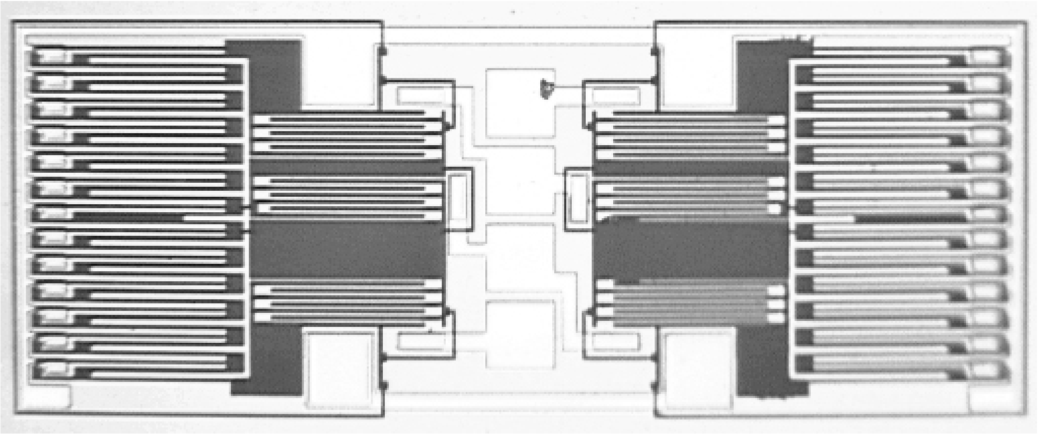

Figure 4.6: Mechanical flip-flop, 80 μm tall

cation process, after performing the deep-trench etch, the trench width varies from several μm to tens of μm and the height varies from tens of μm to hundreds of μm. A few research works have been done for the planarization of MEMS processes [58] [70]. These methods are either complicated or require thick photoresist to planarize the surface topography.

In this project, we demonstrate a simple planarization process that allows post-DRIE (Deep Reactive Ion Etch) lithography. This process works for a topography with various trench widths and depths. The new process was based on the "Sacrificial layer with etch-back" method, which is a well established planarization technique for the IC devices fabrication. As was mentioned before, the topography of MEMS deep-trench process is very different from the topography of the IC fabrication process. In order to adapt the planarization technique from the IC fabrication process, methods that can narrow the opening of deep trenches and make a comparable topography to the IC process have to be performed first. This process is done by performing a perimeter-etch technique and PSG deposition. Afterwards, the spin-on polymer was applied to seal the opening of the trenches, and the "etch-back" process was performed to planarize the surface.

4.3.1 Trench width narrowing

The planarization process starts with a perimeter-etch method. After applying this to the design, all trenches with different sizes of openings and aspect ratios are converted into one width and one aspect ratio. In this case, the trenches are confined to have 4 μm wide openings and 80 μm deep trenches. LPCVD PSG is deposited on the wafer after the deep trenches etches. Due to the low mobility of LPCVD PSG, the resulting film thickness at any given spot varies, depending on the geometry that the vapor phase can transport to that spot. During this deposition, PSG grows 3 μm vertically on the surface but little on the sidewalls. It leaves 1 μm of opening on top of the trenches. Although 1 μm of the trench opening is not as preferred as 0.1 μm opening in the IC process, it is small enough for the spin-on polymer to seal the trenches. In fact, it is difficult to use PSG (or other non-conformal materials) to totally seal the trenches or further scale down the openings of the trenches. The deposition rate of PSG on the sidewalls correlates with the aspect ratio of the trenches [23]. Therefore, the more that PSG grows on the top, the more difficult it is for PSG to get to the sidewalls, thus resulting in a slower deposition rate at sidewalls.

4.3.2 Spin-on polymer

Polymer was spun on the wafer to seal a 1 μm opening. Here we demonstrate two types of spin-on polymers. The first one is OiR897 I-line photoresist. The second is ACCUFLO 413EL (from Allied Signal Inc.). I-line is a high resolution photoresist, while 413EL is a spin-on polymer engineered especially for the planarization/isolation of multiple-layers structure of electrical interconnects in IC devices. Because of its excellent re-flow property, 413EL was able to fill in the 0.1 μm gaps and smooth out the topography in the

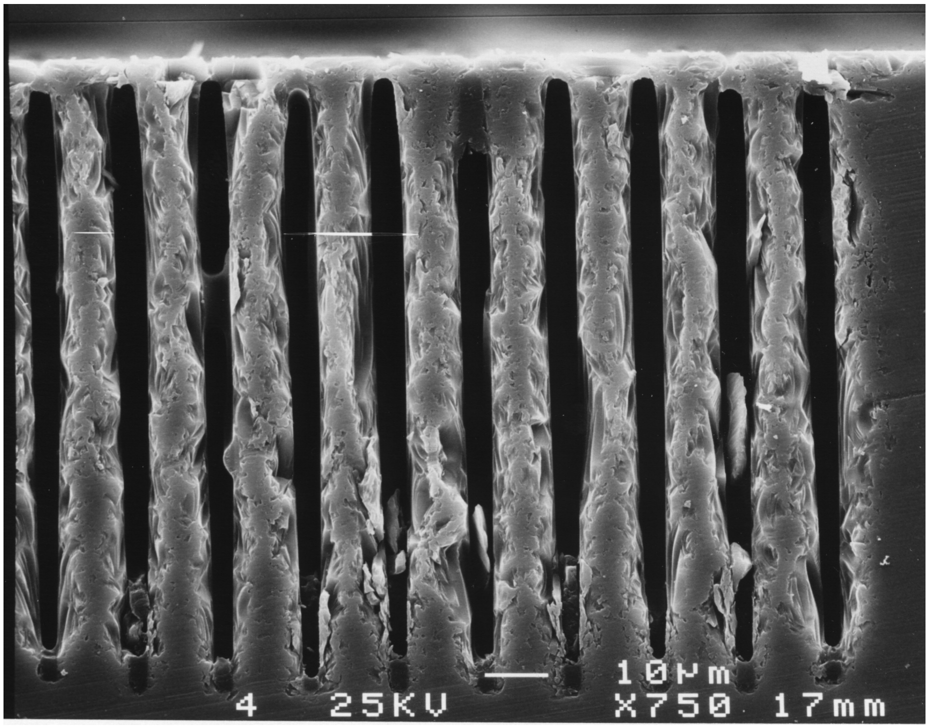

Figure 4.7: 4 μm trenches are sealed by PSG and 413EL spin-on polymer

IC fabrication, after it was spun-on the wafer. Furthermore, 413EL can be etched away by conventional plasma oxide etchers. The advantage of this will be discussed later. In this experiment, I-line was spun on the wafer rotating at 1300 RPM with an expected film thickness 2.0 μm. 413EL was spun on at 2000 RPM with an expected film thickness 0.5 μm.

SEM photos of the resulting spin-on polymer sealing of trenches are shown in the Fig. 4.7 and Fig. 4.8, where 413EL and I-line are used respectively. The trench-profile shown in the photos has trenches that are 4 μm wide and 10 μm apart and were created by STS plasma etch. For this trench profile, PSG deposition narrowed the trench gap but left a small opening. I-line and 413EL were spun on two wafers. As shown in the photos, neither I-line nor 413EL filled the trench gaps completely. Instead both were trapped at the bottleneck of the trenches and sealed the trenches. This result can be attributed to the fact

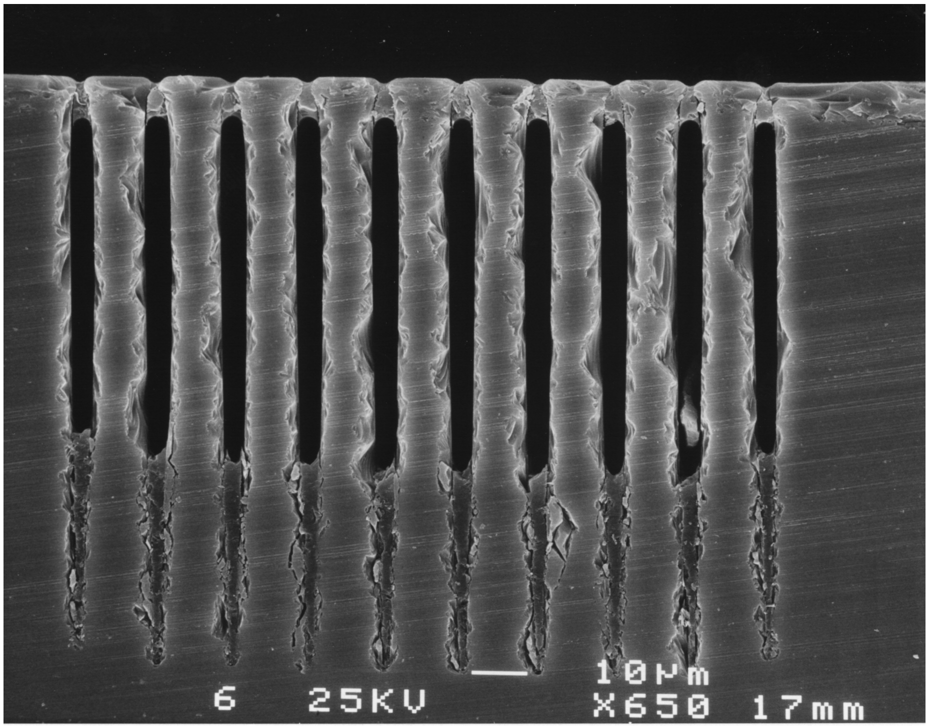

Figure 4.8: 4 μm trenches are sealed by PSG and I-line spin-on polymer

that the polymer film utilized in this process is lacking viscosity, and cannot maintain the necessary film thickness to completely fill the trenches. Most of the polymer was spun out of the trenches and a small portion remained at the bottlenecks due to the narrow channel width. However if a more viscous film is utilized in this experiment, the polymer film may fill the trenches completely. However, on the wafer surface, it may produce a wavier top surface than the less viscous film.

Fig. 4.9 shows the result of performing a 413EL spin-on process on a trench profile with different trench gaps. The trench widths shown in the photograph, after an STS plasma etch, are, from left to the right, 2 μm, 3 μm, 4 μm and 8 μm respectively. After performing 3 μm of PSG deposition and the 413EL spin-on process, 413EL was able to seal the trenches that had a width of up to 4 μm. However, it was not able to seal trenches with

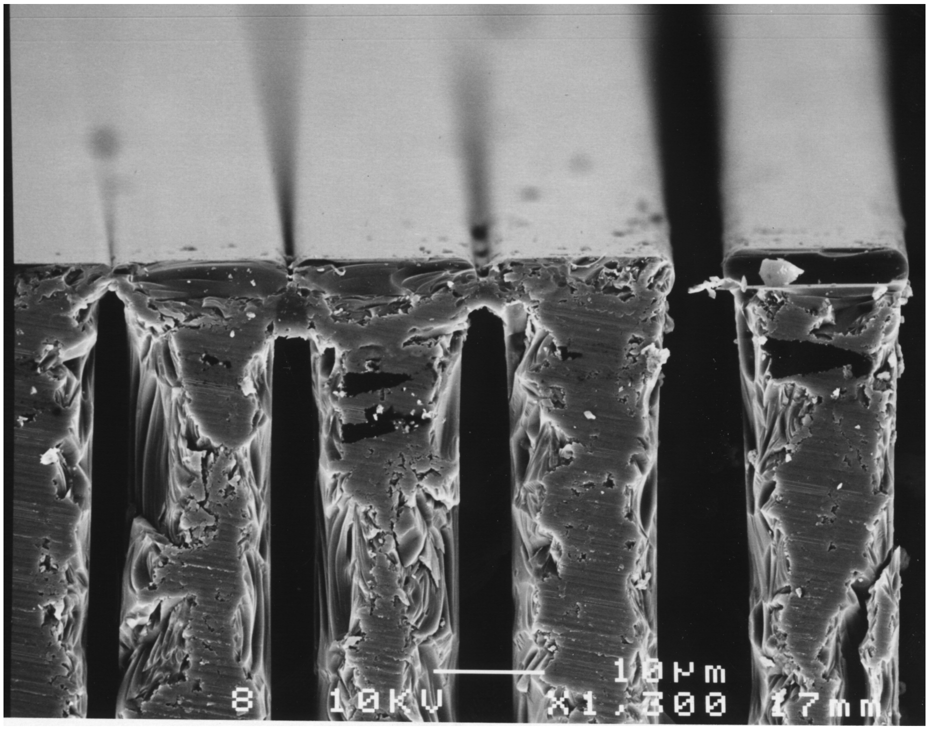

Figure 4.9: 8 μm trenches are not sealed by PSG and 413EL spin-on polymer

a larger width. This result illustrates the importance of incorporating perimeter-etch steps in this planarization process.

Although both of the spin-on polymers tested sealed the trenches, neither of them produced a smooth topography on the top surface of wafers after they (polymers) were spun on wafers. Fig. 4.10 is a closeup of Fig. 4.7. It shows that a groove pattern was formed after the trench were sealed by the polymer. The 413EL was not able to entirely smooth out the topography, which is different from the result obtained in IC fabrication processes. A possible answer to this phenomenon is that, only a scarce amount of 413EL were remained around the trench gaps after the spun-on process, and this insufficient polymer were not able to form a continuous film around trench gaps. Therefore, even 413EL has an excellent re-flow property, it still failed in planarizing the surface due to a discontinues film. The insufficient amount of polymer film around the trench gaps could be due to the proximity of the trench's location, deep trenches, etc., but more experiments are needed to confirm the speculation.

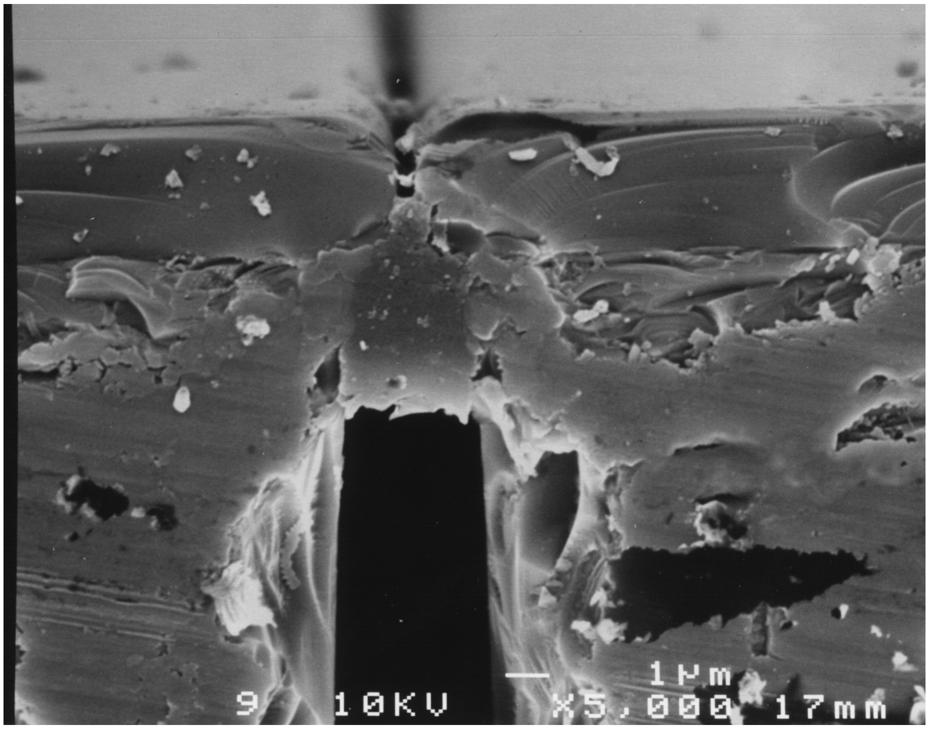

Figure 4.10: Trench profile, trench was sealed by PSG and 413EL polymer

When I-line was applied to seal the gaps, the I-line polymer went inside the trenches and was able to cover the area that is away from the trenches, but none was found on the narrow islands located between trench gaps, as shown in Fig. 4.11.

4.3.3 Etch-back

The topography is planarized by removing the polymer and the sacrificial layer PSG from the surface. Both polymer and PSG can be selectively etched away by oxygen plasma and buffered HF, respectively. Typically, the polymer etch rate in oxygen plasma at

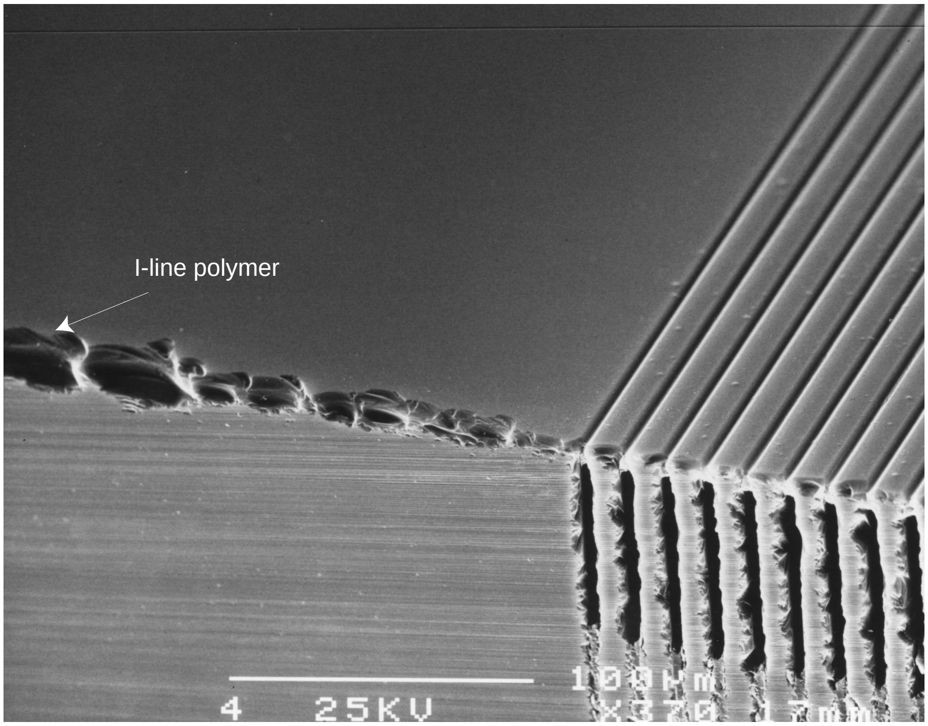

Figure 4.11: Non-uniformity of I-line spin on

200W is around 3000 A/min; while the PSG etch rate in 5:1 buffer HF solution is around 5000 A/min. By alternating on the polymer etch and PSG etch steps, a planarized surface can be obtained. The purpose of alternating between polymer etch and PSG etch is to measure PSG film thickness during the etch process. If the PSG etch is overdone, not only will it clear of the PSG film on the top surface but also will gradually etch away the PSG film on the sidewalls of the trenches. Moreover, If the PSG etch goes deeper than the root of the trapped polymer film, the polymer film will have nothing to hang on to and would be expelled out of the trenches. The alternative to the wet etch process discussed above is to do a dry etch on the polymer and PSG film. As was mentioned before, the 413EL can be etched in a conventional oxide plasma etchers, and the parallel etch of 413EL and PSG results in a smooth topography on the top surface. The etch selectivity of 413EL and PSG in the oxide etcher can be adjusted by the flow ratio of oxygen and CF_4/CHF_3.

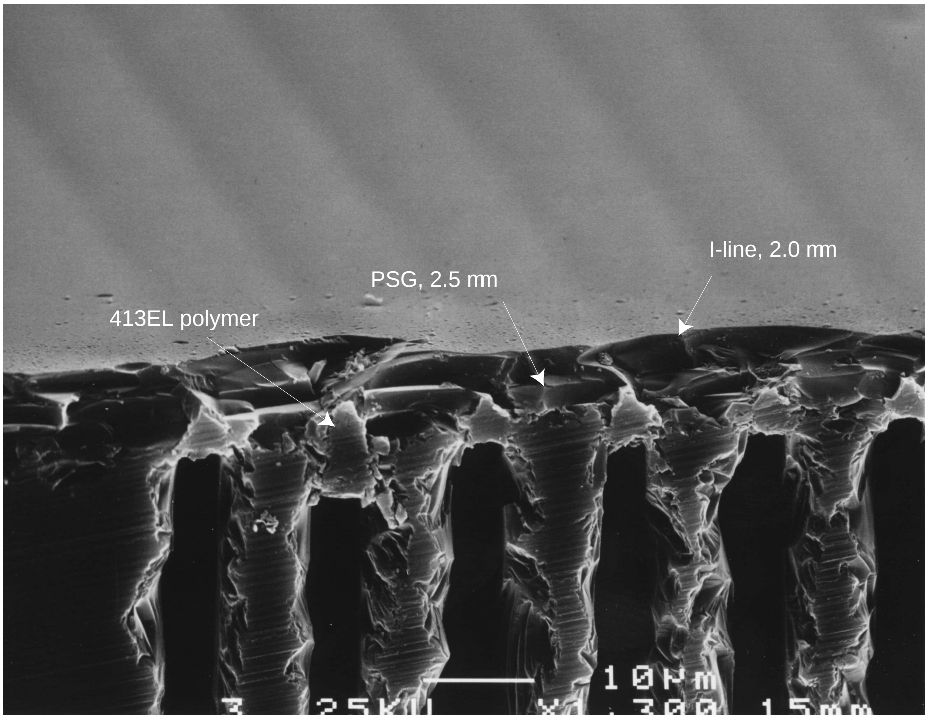

Figure 4.12: SEM for 2 μm of photoresist on the planarized surface

Fig. 4.12 shows the case when 413EL was applied to the surface and subsequently etched back down to the PSG surface. The PSG was partially etched back to 2.5 μm to achieve a planarized topography. Subsequently, 2 μm of I-line was spun onto the surface. As a result, the surface of the photoresist was smooth and the grooves on the topography, as shown in the Fig. 4.12, were measured to be $0.1 \sim 0.2$ μm.

This planarization technique is still in the early stage of the process development. More experiments are needed to validate the conjectures made in this section.

4.4 Metallization

As stated in Section 4.2, the release process involves both a KOH etch and a concentrated HF etch, the candidate of the metallization material must not be attack by either of the two solutions. Copper was chosen as the material for metallization both for this reason and due to its high conductivity. There are few things that need to be taken into consideration when adapting the copper film in the metallization process. They are discussed below.

Although copper film is not significantly attacked by the KOH solution, KOH can permeate through the copper film and slowly etched away the silicon structure underneath. Therefore, it is important that the silicon structure underneath the copper film, as well as the silicon structure exposed to the KOH, be protected by a material that can block the KOH etch.

The standard metallization process requires a thin chrome film to be deposited prior to the designated metal film. The purpose of this process step is to increase the adhesion between the silicon substrate and the designated metal film. It is crucial that all the native oxide is removed from the surface of the wafer prior to the chrome film deposition. If there exists a thin native oxide on the surface, oxide would be attacked by HF and peeling of metal layer would take place during the release process steps [14]. Furthermore, the thin chrome layer oxidizes over time and reacts with HF, thus resulting in peeling off the metal layer as well. The following process steps are suggested by Muller [38] to prevent the metal film from peeling off. (1) The wafer was dipped in Buffered HF for a few seconds before the metal deposition, to eliminate native oxide on the surface. (2) In the chrome film deposition, a thicker than required film thickness was utilized to elongate the lifetime of chrome layer from oxidation.

The copper film formed by thermal evaporation processes tends to have lower electrical conductivity than bulk copper. The resistivity of the deposited film can be predicted by the electron mean-free-path, and two major factors that effect the mean-free-path in the thin film are the thickness of the film and the presence of inert gas during the film formation [51] [67]. In a process where no inert gas is presence, the electron mean-free-path was found to be $410 \pm 100\mathring{A}$. Because of this range of the mean-free-path, the resistivity of the copper film decreases as the film thickness increases. Furthermore, the resistivity stays close to the value of bulk copper, $1.6 \times 10^{-6}\Omega - cm$, where the film has a thickness of 1200 $\mathring{A}$ or higher. In a process where the copper film deposition takes place in the presence of argon at a pressure between 10^{-6} to 10^{-5} torr, argon atoms incorporate into the film and thus decrease significantly the mean-free-path of the film, resulting in 50% increase in resistivity. Increasing the argon pressure to 10^{-4} or higher did not result in a further increase in film resistivity.

As part of this metallization process, a "lift-off" was performed to simplify the overall fabrication process. A thin layer of chrome film ($\sim$ 200 $\mathring{A}$) was deposited by thermal evaporation prior to the copper film and the copper film ($\sim$ 0.5 μm) was evaporated subsequently. The resistivity of the resulting copper film was measured to be $2.65 \cdot 10^{-6}\Omega$ -cm, which was about twice as high as of bulk copper.

4.5 Fabrication Process Flow and Assembly

4.5.1 Fabrication process flow

The complete four mask overall fabrication process flow is shown in the Fig. 4.13. The process is broken down into 5 steps: (1) Piezoresistors patterning, (2) Structure patterning, (3) Planarization, (4) Metallization and (5) Release. The major fabrication work performed in each of the process step, along with the process parameters, is itemized below.

1. Piezoresistors patterning
    (a) LPCVD silicon nitride, 0.5 μm.
    (b) LPCVD undoped polysilicon, 1.2 μm.
    (c) Boron ion-implantation, dosage = $2.5 \cdot 10^{15}\ cm^{-2}$, energy = 150 KeV.
    (d) Post ion-implantation anneal, annealing temperature = $1050\ ^{\circ}C$, time = 90 min.
    (e) Lithography for "PZR" mask: pattern the piezoresistors.
    (f) Polysilicon dry etch: clear the major portion of polysilicon.
    (g) Polysilicon wet etch: 30 sec, clear the polysilicon residue from the process of polysilicon dry etch.
    (h) Dip in 50:1 buffered HF, 40 sec, clear the polymer residue from the process of polysilicon dry etch.
    (i) Silicon nitride dry etch, stop on the silicon substrate.
    (j) LPCVD silicon nitride, 0.5 μm.

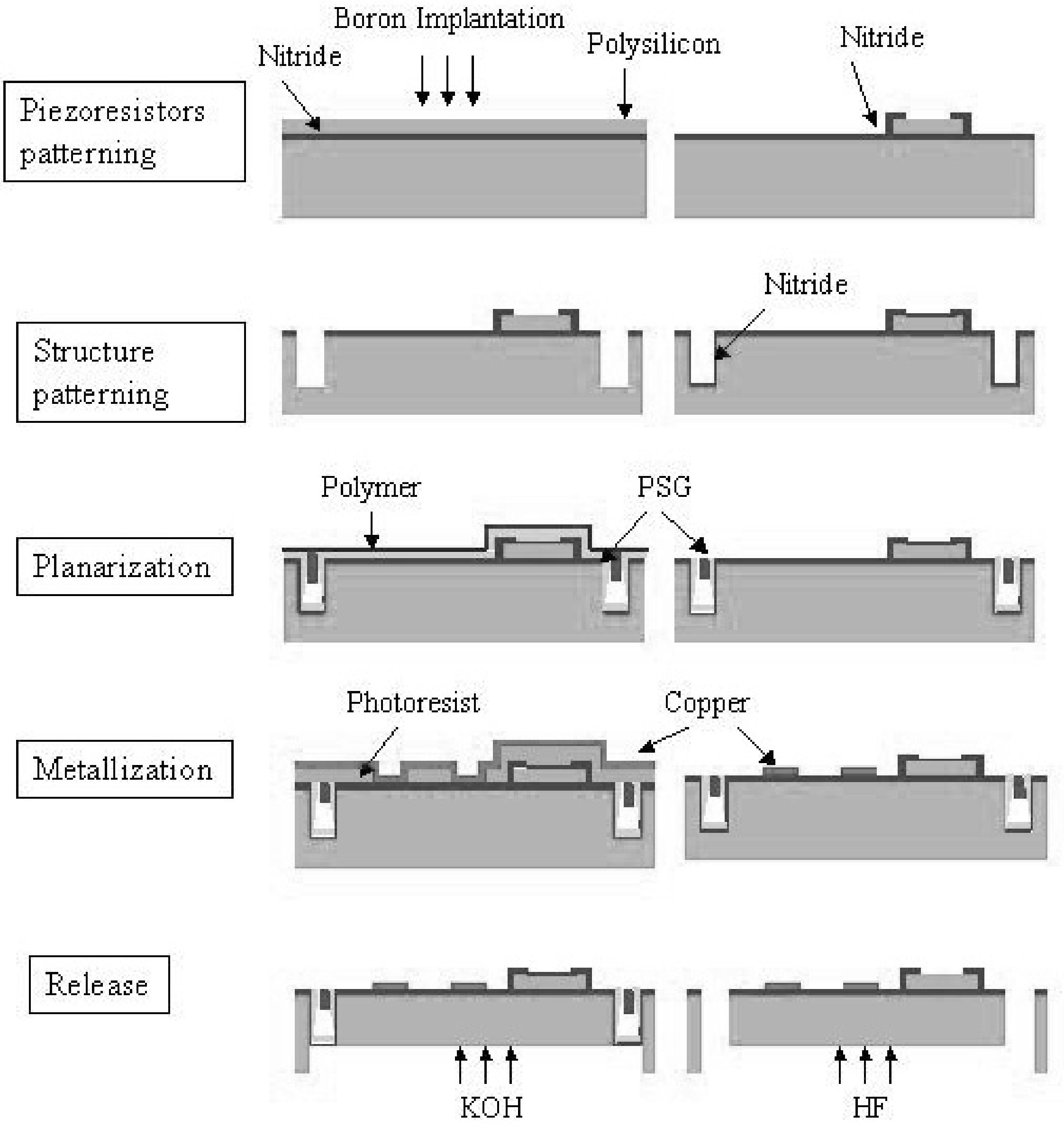

Figure 4.13: Process flow for the silicon suspension

   (k) Lithography for ”CONTACT” mask: open contact windows for the piezoresistors and silicon substrate

2. Structure patterning
   (a) Lithography for ”DRIE” mask: pattern the structure of the silicon suspension.
   (b) STS silicon plasma etch, 80 μm.
   (c) Oxygen plasma, 300W, 10 min
   (d) LPCVD silicon nitride, 0.1 μm.
3. Planarization
   (a) LPCVD PSG, 3 μm.
   (b) Backside etch: clear PSG, nitride, polysilicon on the backside of the wafer.
   (c) Spin-on 413EL polymer, speed = 2000 RPM, time = 1 min, film baking temperature = 220 $^\circ C$, 15 min
   (d) Polymer etch: oxygen plasma, 200W, time ~5 min, until no polymer appears on the surface
   (e) PSG etch: 5:1 buffered HF, 75 sec, little PSG on the surface
   (f) Polymer etch: oxygen plasma, 200W, time = 3 min
   (g) PSG etch: 5:1 buffered HF, 75 sec
4. Metallization
   (a) Lithography for ”METAL” mask: pattern the electrical interconnects, photoresist thickness = 3.3 μm.

   (b) Oxide dry etch, 1 min

   (c) Chrome evaporation, 200 Å.

   (d) Copper evaporation, 5000 Å.

   (e) Lift off process: PRS3000, 90 °C, until the photoresist is dissolved.

5. Release

   (a) KOH etch, 80 °C, time $\sim$ 7 hours, until the bottom of the trenches appear.

   (b) Concentrated HF etch, time $\sim$ 20 min, until the structure is released.

The silicon suspension is thus finished. A photo of the resulting silicon suspension is shown in Fig. 4.14.

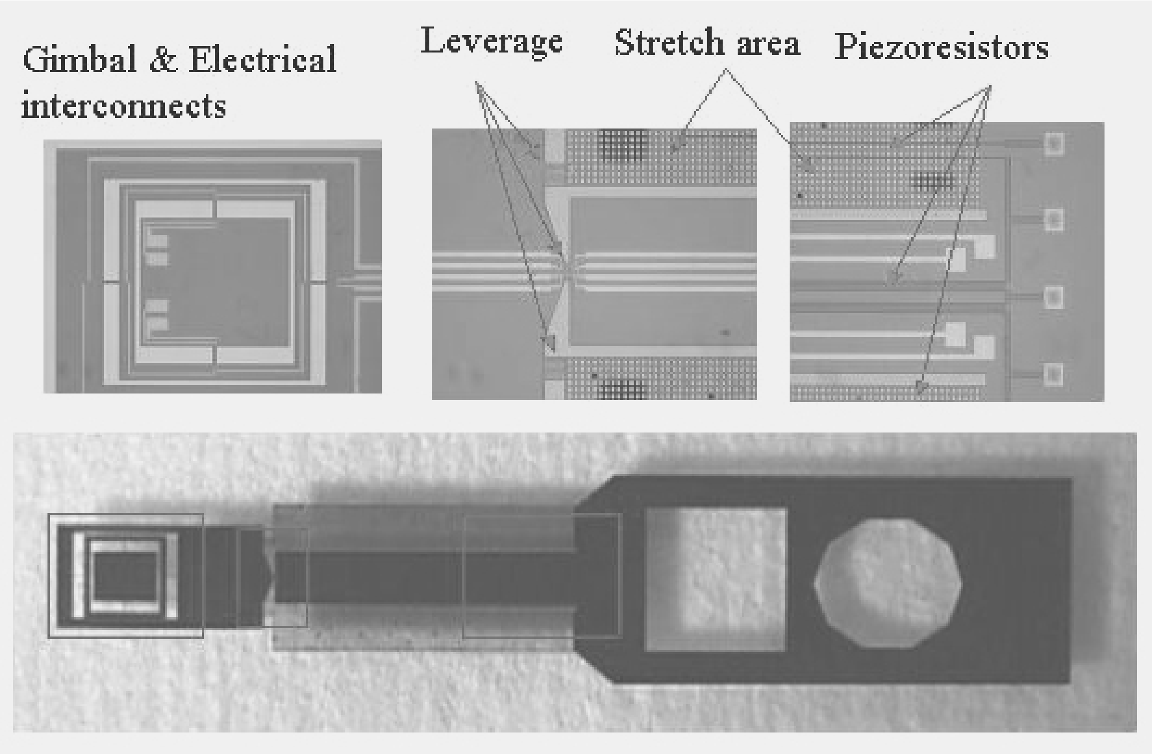

Figure 4.14: Silicon suspension

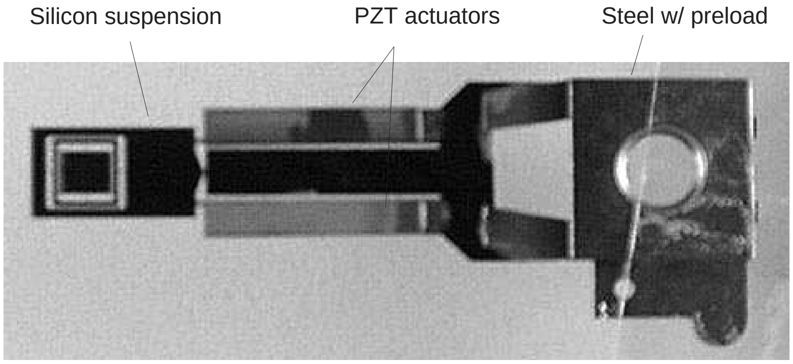

Figure 4.15: The prototype of the PZT-actuated silicon suspension

4.5.2 PZT-actuated suspension assembly

The PZT strips were obtained by dicing a large PZT square. Due to the fact that the PZT piece is thin (127 μm, in this application) and brittle, the vibration induced by the cutting process usually shatters the PZT square. Thus additional steps have been taken in the dicing process to prevent the PZT from shattering. The process is done by bonding the PZT to a dummy wafer firmly with 4 μm of photoresist and cutting the whole assembly at relatively low speed. After being trimmed into the required dimensions (6.5 mm×1 mm), the PZT strips are released from the dummy wafer with acetone and cleaned with water. 4 pieces of the PZT strips were glued to the silicon suspension with the conductive epoxy, two at the top of the suspension and two at the bottom of the suspension. Subsequently, the silicon suspension is cut at a slender area located between the E-block and the end of the PZT strips. The whole PZT–silicon suspension assembly is then glued to a steel suspension that has a pre-bend on it. The resulting assembled suspension is shown in Fig. 4.15

Chapter 5

Experimental Results and Discussion

Various experiments were performed to examine the feasibility of implementing a dual-stage-servo system using the fabricated PZT-actuated silicon suspension. These experiments included: (1) Measuring the structural resonances of the suspension. (2) Performing a slider fly test on a spin stand. (3) Evaluating the dynamic response of the suspension under PZT actuation. (4) Evaluating the sensitivity of the piezoresistive sensors. (5) Determining the transmission speed of the electrical interconnects. The experimental setups used to perform these tests and the corresponding test results are discussed in each of the following sections.

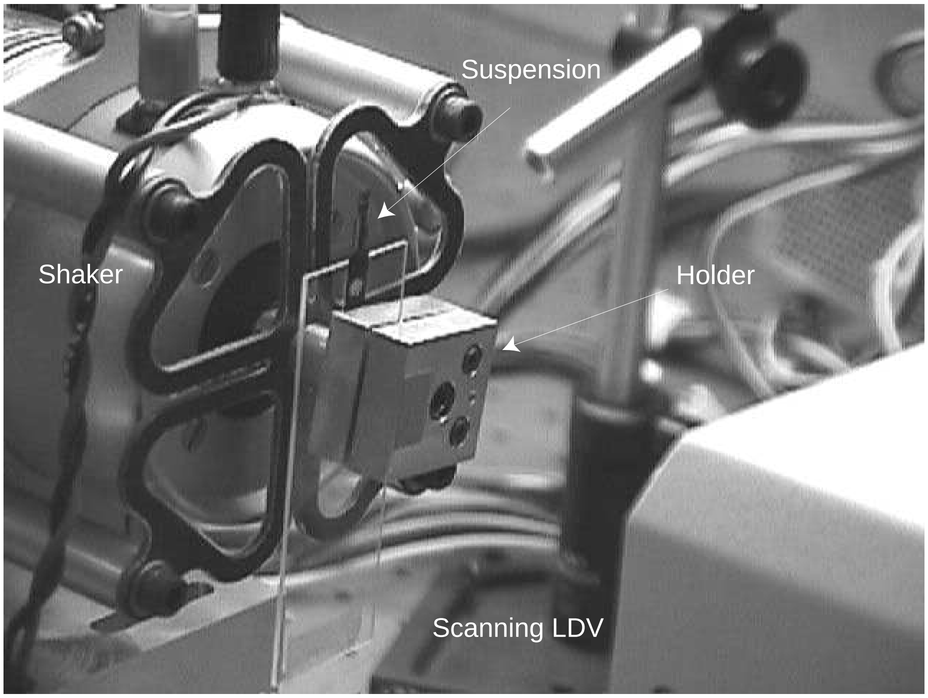

Figure 5.1: Experiment setup for the Scanning LDV testing

5.1 Measuring the Structural Resonances of the Suspension

5.1.1 Scanning LDV setup

A scanning LDV (Laser Doppler Vibrometer) was utilized to determine the structural resonant frequencies and corresponding mode shapes of the suspension. In this test, the suspension was loaded on a suspension holder that was actuated by a shaker. The laser beam was targeted at the suspension and aligned along the particular direction of motion which needed to be examined. The motion of the targeted point on the suspension was automatically detected by the LDV apparatus. Moreover, the multiple target point locations can be pre-programmed in advance. When the shaker sweeps a frequency range, the motion of the suspension at each laser targeted point is recorded and analyzed. Resonant frequencies in that range are identified and their associated mode shape are constructed. The scanning LDV setup is shown in Fig. 5.1.

To find out the resonant frequency of each dominant mode, the experiments were peformed with 3 different setup arrangements. In the first arrangement, the suspension was loaded and it was facing the LDV apparatus. The laser aiming spots spread out the overall suspension at 90 different locations. This arrangement can locate the resonance modes for bending motion and torsion motion of the overall suspension. In the second arrangement, the suspension was loaded in the same position as the previous case but with the laser aiming spots focused on the gimbal structure only. This was intended to pick up the resonance modes associated with relatively small motion of the gimbal structure. The motion of 128 different locations on the gimbal structure was recorded. This setup not only revealed the gimbal motion but also provided more motion information, in conjunction with the first setup, to identify the resonance modes of the overall suspension. In the last arrangement, the suspension was loaded in such a way that its sidewall faced the LDV apparatus. The laser aiming spots were focused on the sidewall of the picoslider. This position could reveal the sway motion of the suspension, or any type of motion that contributes to the off-track-error for the suspension. In all three tests, the sweeping frequency was from 6.25 Hz to 12 KHz.

5.1.2 Resonant Frequency Identification

The testing results of the experiments described above are shown in Fig. 5.2. In the plot, the significant resonant frequencies are marked with an ”x”. These three plots are not drawn to scale. For the y-axis in the upper plot, 0 dB = 100×10^{-6} (m/s)^2; in the middle and the lower plot, they are 0 dB = 625×10^{-6} $(m/s)^2$. Although many of the abandoned resonant modes in the plot have a relatively high resonant amplitude, they are mostly associated with the suspension holder of the shaker, and thus are not relevant. The mode shapes associated with each of the resonance modes, that were marked with an "x" in Fig. 5.2, are shown in Fig. 5.3.

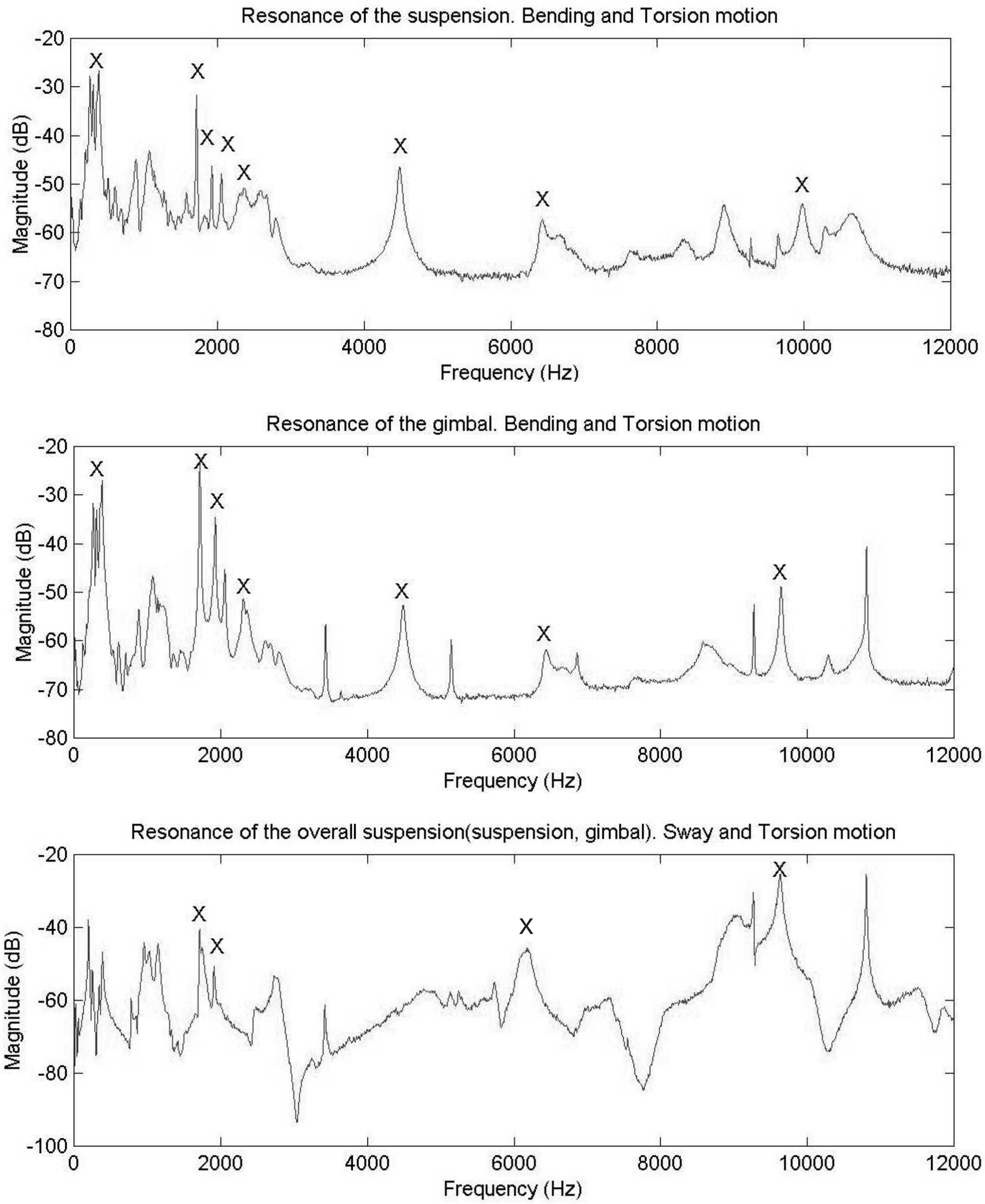
Resonance of the suspension. Bending and Torsion motion

Resonance of the gimbal. Bending and Torsion motion

Resonance of the overall suspension(suspension, gimbal). Sway and Torsion motion

Figure 5.2: Vibration spectrum of the silicon suspension from Scanning LDV

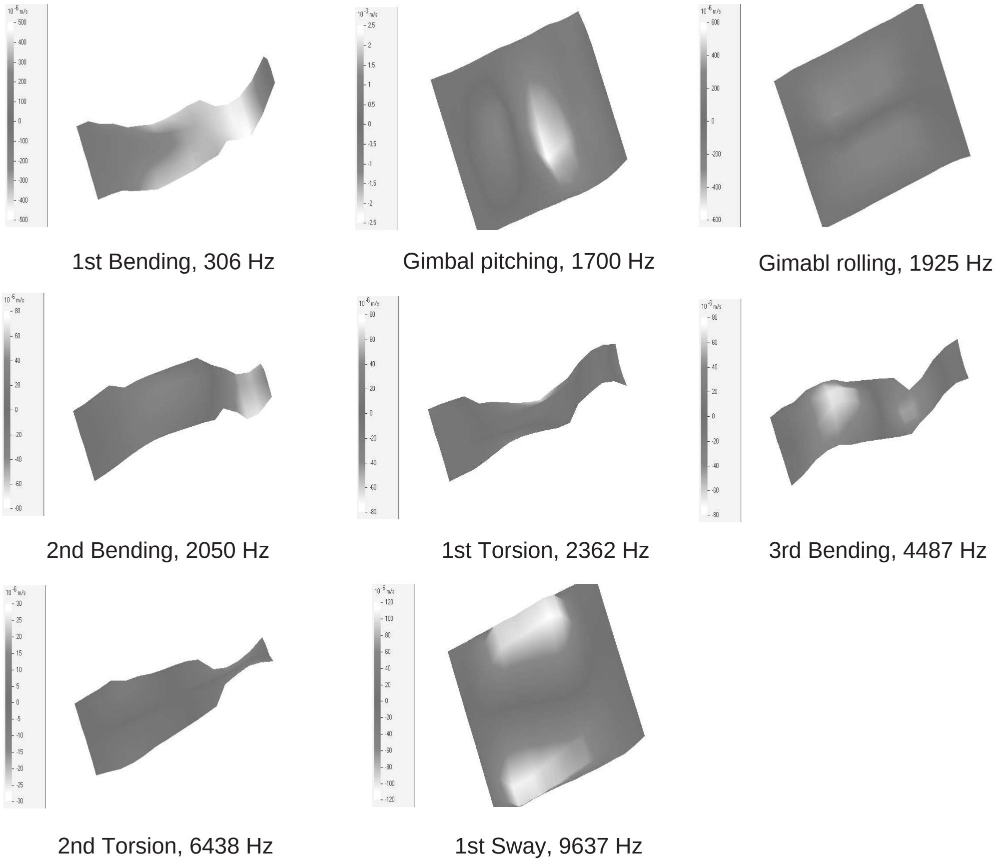
1st Bending, 306 Hz
Gimbal pitching, 1700 Hz
Gimabl rolling, 1925 Hz
2nd Bending, 2050 Hz
1st Torsion, 2362 Hz
3rd Bending, 4487 Hz
2nd Torsion, 6438 Hz
1st Sway, 9637 Hz

Figure 5.3: Mode shape of the resonance from scanning LDV

Due to the fact that the slider was not flying in these tests, the air bearing restoring force was not present. As a consequence, a gimbal-roll motion appears in the off-track-error. This mode is not expected to contribute to the off-track-error during a normal mode of operation in real HDDs. Frequencies of the identified resonance modes in the experiment, along with results obtained from FEM simulation presented in Chapter 3, are listed in Table. 5.1, for the comparison purpose. As shown in Table. 5.1, the resonances modes of the fabricated suspension are generally lower than the simulation results obtained from FEM simulation. This may be due to either the height of the fabricated suspension (measured to be about 75 μm) is less than the designed value (80 μm), or too much epoxy was dispensed to glue the picoslider to the gimbal structure. The first bending stiffness is exceptionally higher than the value obtained from FEM simulation. A reasonable speculation is that during the assembly of the silicon suspension and a steel E-block, the overlap area for gluing two pieces together, which is the key design parameters for adjusting bending stiffness, is larger than what was modeled in the FEM simulation. Thus the frequency of the first bending resonance mode is larger than the expected value. The resonance frequency of the gimbal pitching motion is also higher than the expected value. We are still investigating this discrepancy and have not reached a conclusive answer yet.

	Steel–Silicon suspension	FEM results
1st Bending (spring constant)	306 Hz	240 Hz
Gimbal torsion bar pitching	1700 Hz	2088 Hz
Gimbal torsion bar rolling	1925 Hz	1817 Hz
2nd Bending	2050 Hz	2402 Hz
1st Torsion (off-track resonance)	2362 Hz	2638 Hz
3rd Bending	4487 Hz	4514 Hz
2nd Torsion (off-track resonance)	6438 Hz	7639 Hz
Sway (off-track resonance)	9637 Hz	10216 Hz

Table 5.1: Resonance frequencies of the steel–silicon suspension

5.2 Fly-ability Test

Flying the slider on a spin-stand constitutes an ultimate test to determine the feasibility of eventually utilizing the suspension and gimbal design presented in this dissertation in an actual HDD. When the disk is rotating, the air bearing lifts the picoslider, against the preload from the suspension. With an accurate suspension and gimbal design, the picoslider should be able to follow the terrain on the rotating disk smoothly. Two tests were done to characterize the flying capability of the overall suspension, gimbal and slider system: (1) Measurement of the friction force between the slider and disk. If the friction is too large, the magnetic head will not be able to be accurately positioned, even worse, the slider may stick to the disk. (2) Measurement of impact on the slider due to sporadic contact between the slider and the disk. The slider can bounce up and down while hitting bumps on the disk topography. If this impact happens too often, the slider may scratch the disk and result in an un-recoverable damage.

5.2.1 Experimental setup

The experimental setup is shown in Fig. 5.4. The suspension was loaded on the holder and lowered down to the glass disk of the spin stand by calipers, until it reached the desired ”z-height”. The disk spinning speed and VCM actuation can be programmed for different operating conditions. On the upper part of the suspension holder, both a friction sensor and an AE (Accoustic Emission) sensor were placed. The friction sensor consists of four strain gauges which compose a Wheatstone bridge for voltage readout. The AE sensor is made of a piezoelectric transducer which detects high frequency elastic waves. A sharp bandpass filter was utilized to differentiate signals of actual head/disk contacts from signals generated by air bearing lift force fluctuation. This was necessary because the signals produced by air-bearing force are typically 20 to 30 dB larger than the signal generated by actual head/disk contacts.

In this experiment, the suspension was lowered onto the disk while the disk was spinning at 12000 RPM. The experiment started with disk spinning at 12000 RPM and it

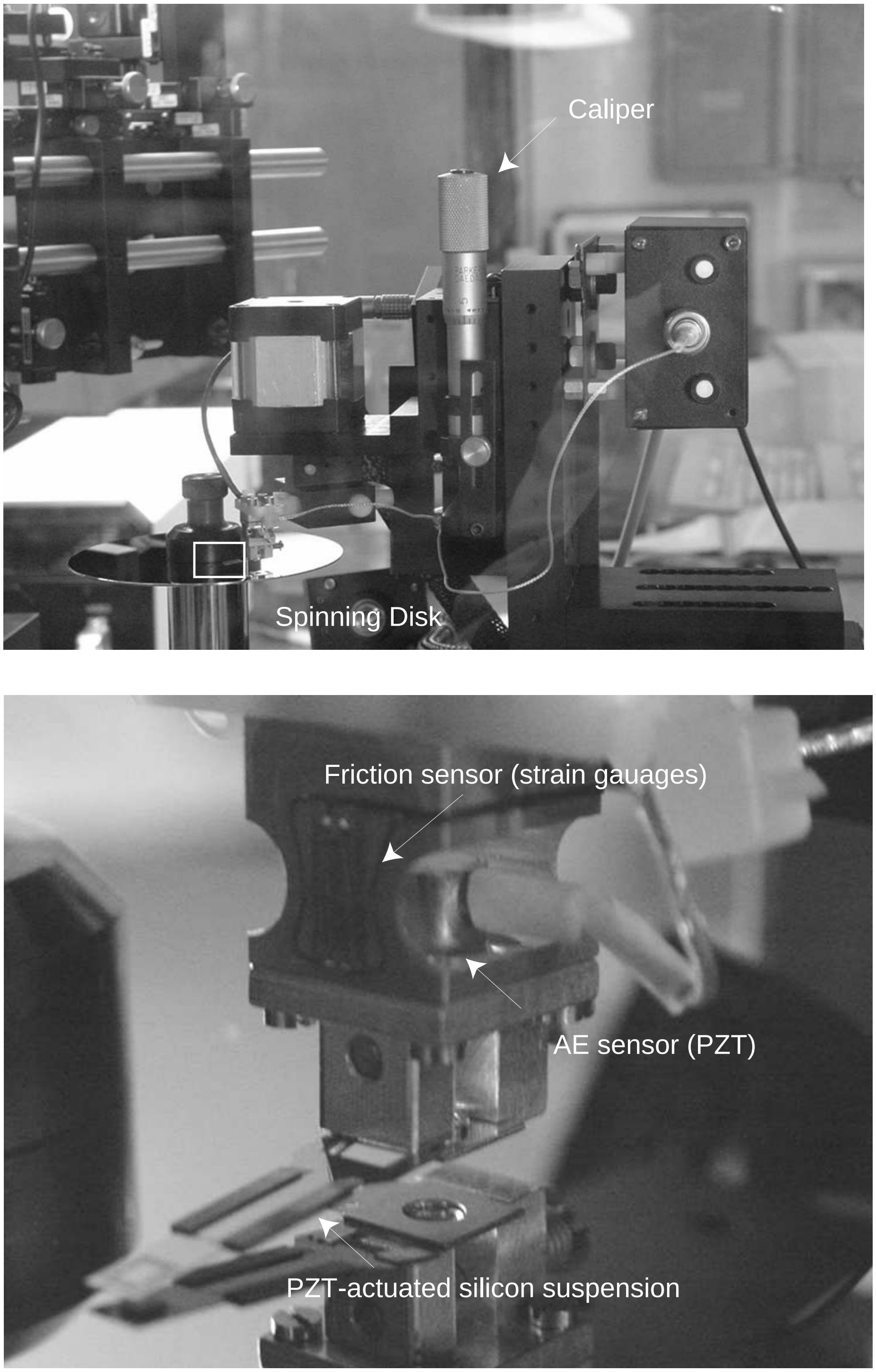

Figure 5.4: Experiment setup for the fly test

was slowly decelerated to 7200 RPM for the purpose of exaggerating the friction and impact effects, which may take place between the disk and the picoslider. When contacts between the slider and the disk occur, the monitored friction force increases and the signal from AE sensors jumps up.

5.2.2 Testing results

The recorded friction force between disk and slider, along with the disk spin-speed profile, is shown in the upper plot of Fig. 5.5. The AE signal is shown in the lower plot. From Fig. 5.5, it can be concluded that one collision took place at the 30 sec time, because the accoustic emission spikes up significantly at that time. However, there is no obvious increase in friction at that instance of time in the friction plot. One possible explanation for this apparent discrepancy is that the friction signal is noisy, and therefore it is difficult to distinguish a small amount in friction increase due to a slider collision with the disk, while the thrust of friction is reduced due to deceleration of the disk spin speed. More collisions should have been observed at the lower disk rotation speed regime due to the reduction of fly height. We suspect that some particles were trapped on the Air Bearing Surface (ABS) of picoslider, which produced a kind of shock absorber that attenuated the collision. The torsion bars for the integrated gimbal structure remained undamaged at a friction force level of around 3 grams and eventually broke when the friction force level reached 13 grams.

The testing results indicate that the proposed silicon suspension has the required mechanical properties to fly a picoslider on a rotating disk. Furthermore, it partially confirms the feasibility of using silicon suspensions in actual HDDs. The testing results also suggest the necessity of utilizing a load/unload mechanism for this suspension, in oder to prevent excessive friction forces, which can damage the gimbal, when the HDD is turned on/off. Such mechanisms are currently used by most manufactures. More fly-ability experiments are needed to further evaluate the performance of this suspension-slider assembly.

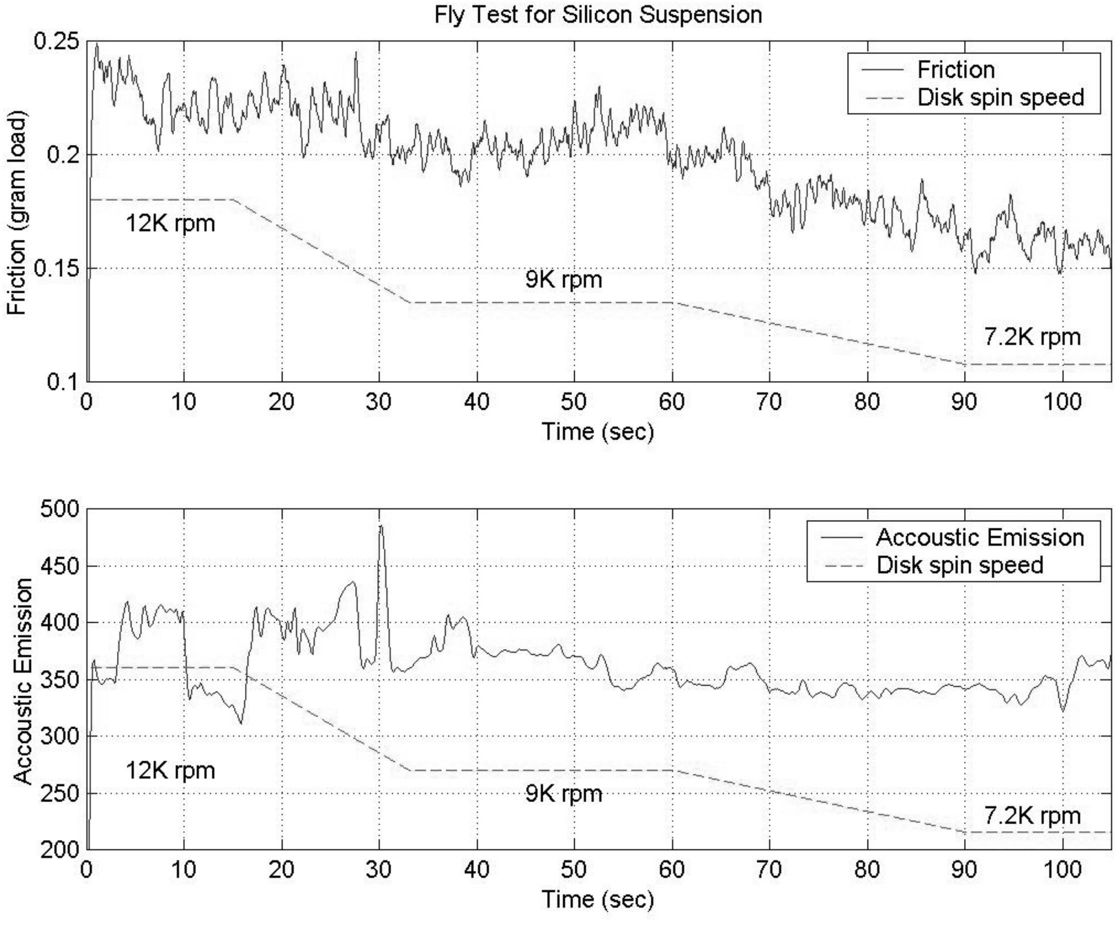

Figure 5.5: Fly capability test with steel-silicon suspension

5.3 Experimental Testing of the PZT Actuation

In this test, voltage was applied to the four pieces of PZT strips and the resulting motion of the actuated magnetic head and/or tip of the PZT strip were measured with an LDV apparatus. By measuring the time-domain response of these displacements, it is possible to characterize the PZT actuation, the response of the hinge structure and the overall frequency response of the slider subjected to the PZT actuation.

5.3.1 Time-domain response

In this experiment, sinusoidal input voltage signals, with amplitudes of 30 Volts/ 10 Volts and a frequency of 2 KHz, were applied to the PZT actuators while both the magnetic head displacement and PZT stretch were measured. The upper plot in Fig. 5.6 shows that, under a 30 Volts sinusoidal input voltage, the amplitude of the magnetic head displacement was 1.33 μm, while the amplitude of the PZT stretch was 0.38 μm. The lower plot shows that, under a 10 Volts sinusoidal input voltage, the resulting magnetic head displacement amplitude was 0.28 μm, while that of the PZT stretch was 0.1 μm. This PZT driving capability is close to the value predicted by FEM simulation (PZT driving voltage $\pm$20 Volts, magnetic head displacement $\pm$1 μm).

The linearity of the PZT actuation is shown in Fig. 5.7. In the upper plot, the head displacement motion is shown when the PZT actuators were driven by the 30 Volts/ 10 Volts sinusoidals at 2 KHz respectively. The resulting amplitude of the motion are 1.33 μm and 0.28 μm, respectively. The ratio of these two signal is 4.75 (1.33 μm / 0.28 μm = 4.75), instead of 3 (30 Volts / 10 Volts = 3). This observation indicates that the amplitude of the head displacement may not be linearly related to the PZT driving voltage. The lower plot shows the stretch amplitude of the PZT strips as a function of the voltage amplitude on the PZT actuators. The voltage input amplitude varied from 5 Volts to 20 Volts while the driving frequency was kept at 1 KHz. A linear regression was utilized to model the

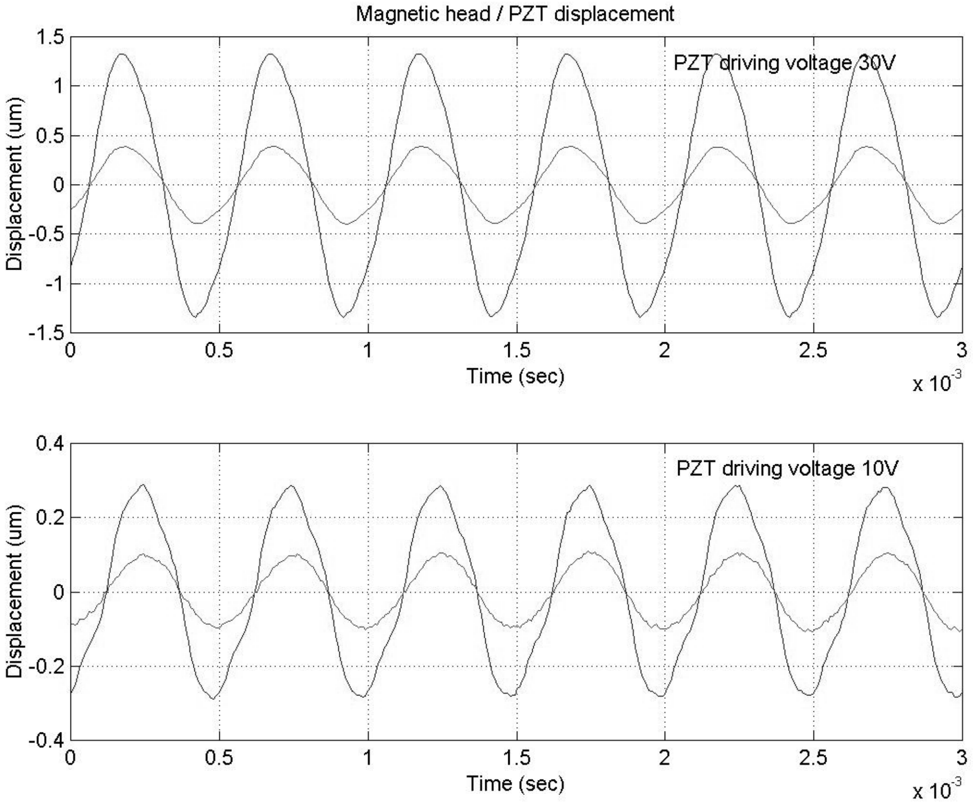

Figure 5.6: PZT actuation capability

relation between the PZT driving voltage and its deformation. As shown in the plot, the slope of the linear regression is $8.57 \times 10^{-3}\mu$m/Volts, while the biggest discrepancy between the data point and the linear regression was about 4.5 %. The recorded nonlinearity in head movement could be due to an LDV measurement error, the nonlinearity of the PZT movement, and/or the nonlinearity of the leverage structure. For the LDV measurement error, as was mentioned before, the in-plane PZT actuation excites the out-of-plane bending motion of the "stretch area". This motion produces a torsional motion of the magnetic head that results in the lost of traction of the LDV laser aiming spot on the magnetic head. The linearity of the PZT movement has been discussed above and the nonlinearity of the leverage

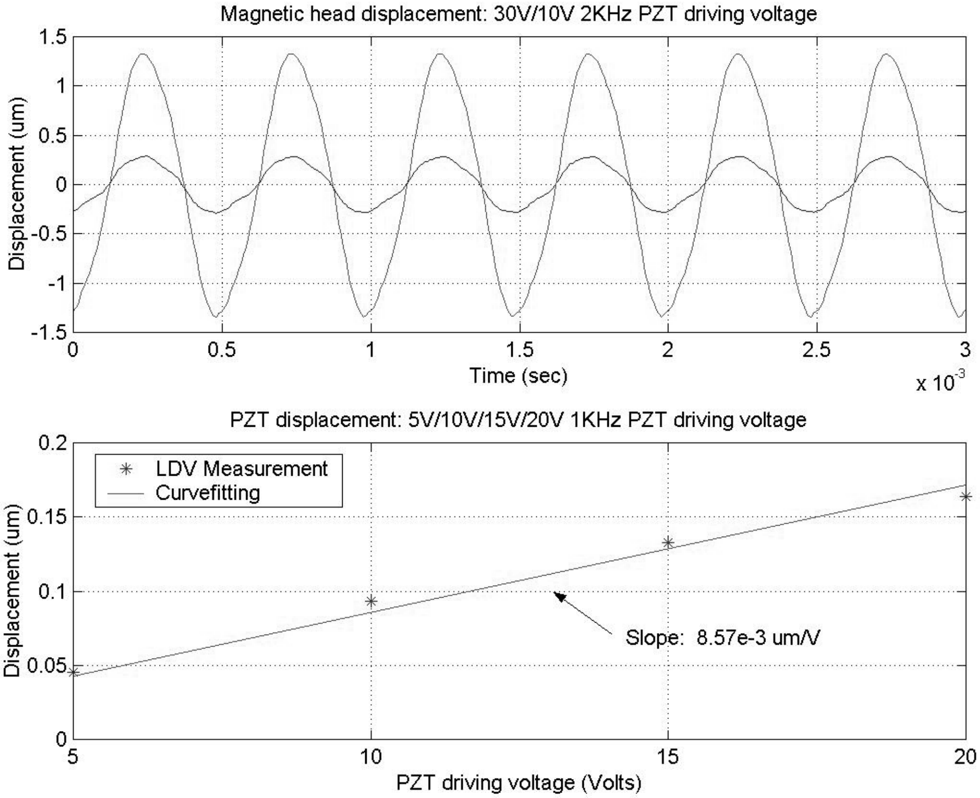

Figure 5.7: Characteristic of PZT actuation

structure will be discussed subsequently.

Although the data points associated with the PZT driving voltage amplitude of 30 Volts do not appear in the lower plot of Fig. 5.7, it is believed that the relationship is fairly linear at that amplitude. This speculation was confirmed by the experimental results shown in Fig. 5.8.

In Fig. 5.8, the head displacement vs. PZT driving voltage and PZT stretch vs. PZT driving voltage are plotted together, for comparison purpose. Under a 30 Volts sinusoidal signal input, the PZT stretch displays a hysteresis phenomenon of about 0.12 μm at zero Volts, but no obvious saturation seems to occur at +/- 30 Volts. The nonlinear

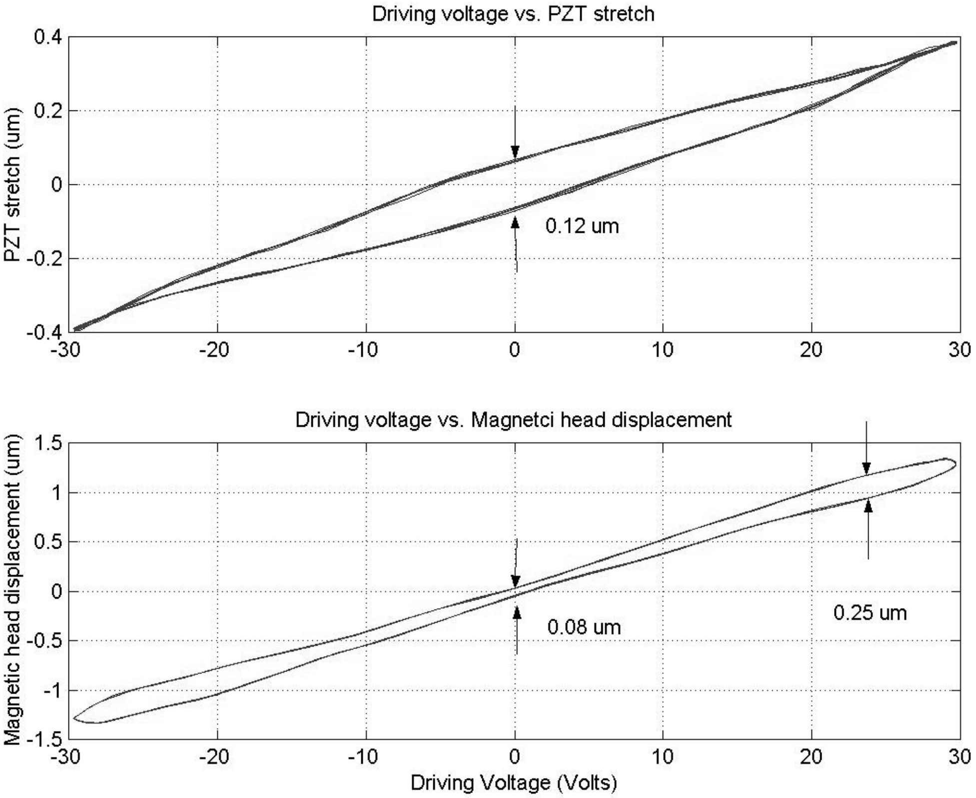

Figure 5.8: Characteristics of PZT actuation

phenomenon for the head displacement, shown in the left of Fig. 5.8, is the combined outcome of the hysteresis of the PZT actuation, the push-pull actuation scheme, and the characteristics of the leverage structure. At the small driving voltage regime, the nonlinear effect is 0.08 μm, smaller than the 0.12 μm value presented in the hysteresis of each PZT strip. It is believed that the symmetry of the PZT push-pull actuation scheme counteracts most of the hysteresis behavior of each PZT strip.

5.3.2 Displacement-amplification factor

The displacement-amplification factor of the hinge structure can be calculated from the data above. In the case of the 30 Volts PZT driving voltage, the head displacement is 1.33 μm and the PZT stretch is 0.38 μm. The displacement-amplification factor is calculated to be 3.5. In the case of 10 Volts PZT driving voltage, the head displacement is 0.28 μm and the PZT stretch is 0.1 μm. The displacement-amplification factor for the 10 Volts input excitation is 2.8, which is smaller than the case when the PZT driving voltage is 30 Volts. This nonlinear behavior of the leverage structure could be a result of the hinge structure design and/or the LDV measurement error. A hinge structure design that can transform the linear motion into radial motion with the better conversion precision can be found in the reference [69].

Since the piezoresistive RPES sensors of this silicon suspension relies on the leverage structure to obtain the position of the magnetic head, the existence of varying displacement-amplification factor suggests that calibration of the displacement-amplification factor and a corresponding look-up table are needed to ensure sensing accuracy.

5.3.3 Frequency response

The frequency response of the PZT actuation was performed with the LDV measurement. The measurement was taken over a frequency range between 100 Hz and 12 KHz. The result is showsn in Fig. 5.9. The resonance mode of the gimbal-roll motion has a frequency of 1.945 KHz. However, it only has little effect along the off-track error direction. The amplitude, at that frequency, rises up 0.15 dB, which is equivalent to 23 % increase in magnitude. The first significant structural resonant mode for the PZT actuation is observed

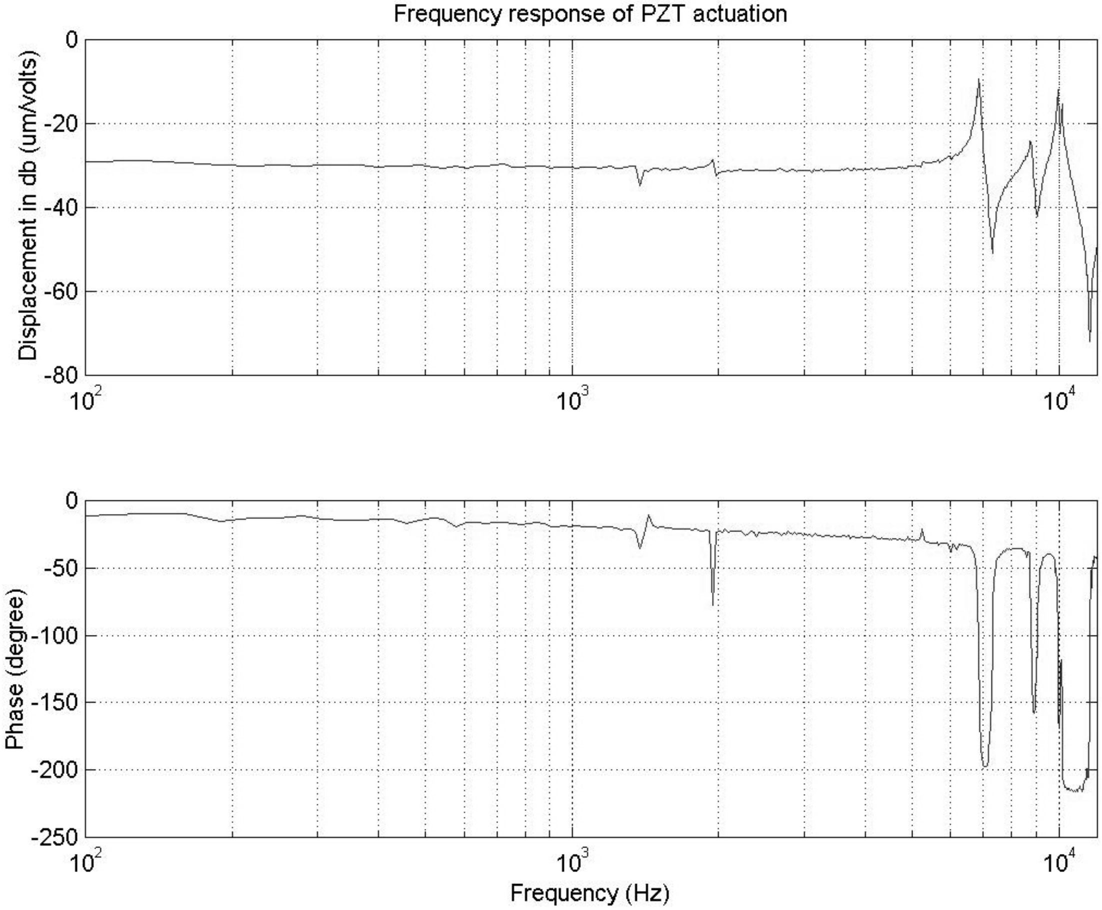

Figure 5.9: Frequency response of the PZT actuation. The first resonant frequency is 6.85 KHz

to be at about 6.85 KHz, while the second resonance mode is at about 9.9 KHz. The amplitude increases by about 20 dB in both cases. The first resonance is due to the suspension torsional motion while the second resonance is due to the suspension's sway motion, as indicated by their respective phase characteristics, shown in the lower plot of Fig. 5.9. At 6.85 KHz, the phase drops but jumps right back. However, at 9.9 KHz, it drops and it does not come back right away. This experimental result agrees with FEM simulation and the scanning LDV testing.

5.4 Piezoresistive Sensors Characterization

In order to characterize the piezoresistive sensor on the silicon suspension, a differential amplifier was implemented to read out the voltage produced by piezoresistors Wheatstone bridge. The differential amplifier has a unity differential gain, a bandwidth of 30 KHz and an input resistance of 2 MΩ. In the experiment, voltage was applied to the four pieces of PZT actuator and the output was either measured at the output terminal of the differential amplifier or at the terminal of each individual piezoresistor.

5.4.1 Static test

In this test, the PZT driving voltage was kept constant or changed slowly. The resulting resistance variation of the piezoresistive film, due to the stretch of the PZT strips, is plotted in the upper plot of Fig. 5.10, while the voltage output of the piezoresistor bridge is plotted in the lower plot. For this piezoresistive film, the experimental data shows a linear relation between stretch and resistance variation. Furthermore, the sensitivity, extracted from the slope of the plot, is 1.81 KΩ/ μm. This corresponds to a Gauge factor of 30 for the piezoresistive film. The output of the Wheatstone resistor bridge was 12.13 mV/ μm under a bridge dc bias voltage of 5 Volts.

5.4.2 Dynamic test

In this test, a sinusoidal voltage was applied to the PZT actuators. A large feedthrough from the input voltage, applied at the PZT actuators, to the output of the piezoresistors bridge was observed during the experiment. To understand the nature of this problem, a supplemental experiment was done to determine the feedthrough from PZT

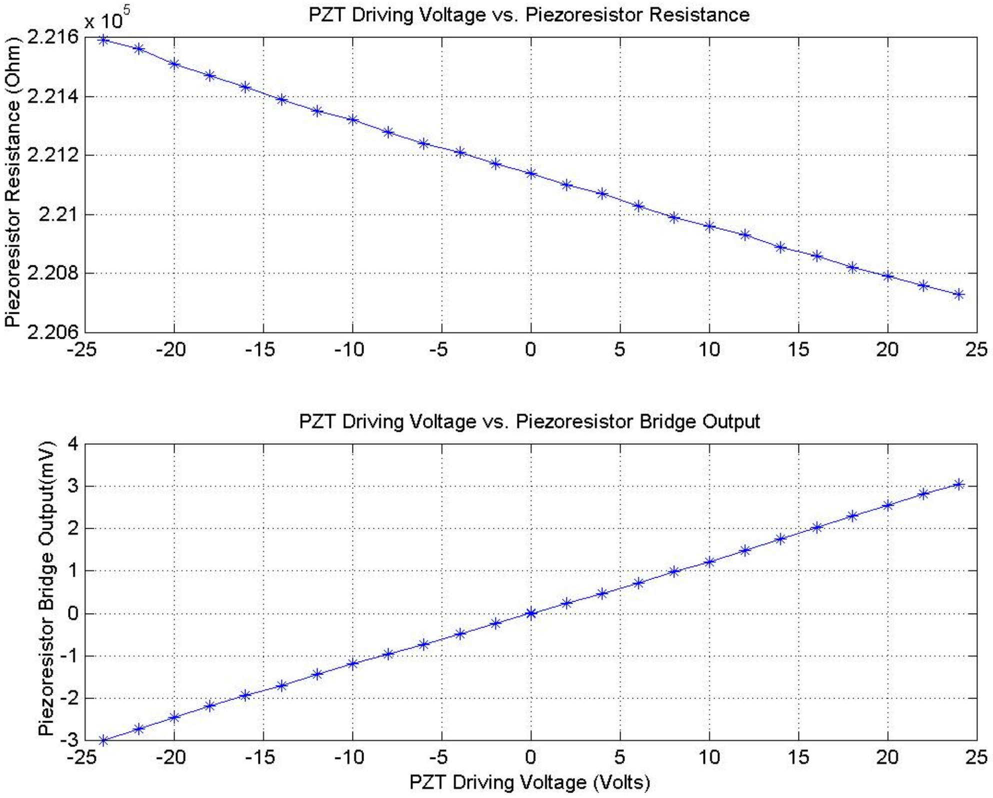

Figure 5.10: Characteristics of Piezoresistors sensor

driving voltage to each individual piezoresistor. Fig. 5.11 shows a caricature of the "stretch area", depicted to illuminate the electron flow path that results in the feedthrough effect, and its equivalent resistance-capacitance circuit diagram. Based on this circuit diagram, and neglecting the high frequency resonance modes, the transfer function of the feedthrough was derived as follows.

$$\frac{V_{PZT}}{V_{out}} = \frac{s\frac{C_{eq}}{C_2+C_{eq}}}{s+\frac{1}{R_L(C_{eq}+C_2)}}$$

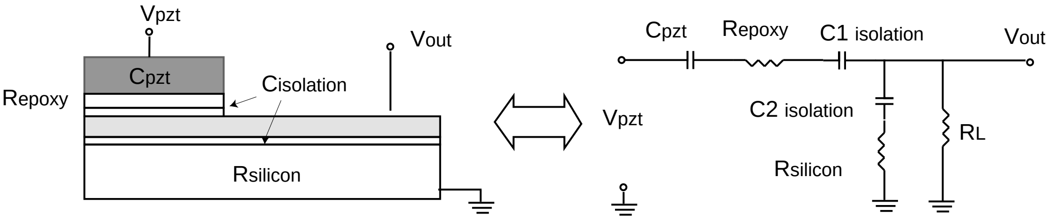

Figure 5.11: Feedthrough path from PZT to the piezoresistor

Where, $C_{eq} = C_1 \cdot C_{pzt}/(C_1 + C_{pzt})$ and R_L is the input resistance of the differential amplifier. The equivalent capacitance from PZT to the silicon suspension (C_{eq} in series with C_2) and the input resistance R_L were both measured using a multi-meter to be 200 pF and 2 MΩ, respectively. These numbers sets the corner frequency, $1/(R_L(C_{eq} + C_2))$ in the equation above, to about 400 Hz. The frequency response of the feedthrough, from PZT driving voltage to two individual piezoresistors located at different locations, was measured with a Spectrum Analyzer, and the result is shown in the Fig. 5.12. As shown in the plot, the feedthrough to two individual piezoresistors (one piezoresistor is located in "stretch area" and the second one is located at the middle of the suspension), both have a corner frequency of about 500 Hz. Moreover, the feedthrough to these two piezoresistors is almost the same at the low frequency region.

Fig. 5.13 shows the feedthrough from the PZT driving voltage to the output of the piezoresistors bridge. Due to the symmetry of the four resistors and the fact that roughly the same amount of feedthrough takes place at the low frequency region in each of the piezoresistors, the feedthrough effect cancels itself to a certain extent at the bridge output.

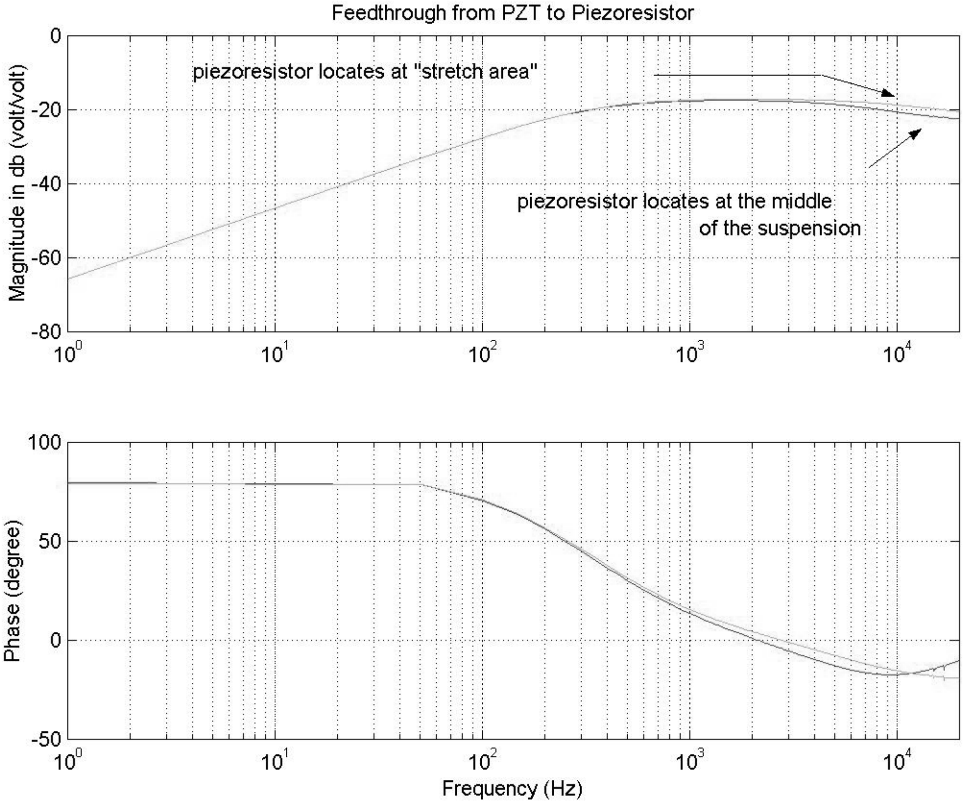

Figure 5.12: Feedthrough: from PZT to the individual piezoresistor

This reduction is up to 40 dB at the low frequency range. However, the feedthrough at high frequency does not cancel significantly. The feedthrough at 20KHz has only a 6 dB improvement as compared to the feedthrough of an individual piezoresistor.

5.4.3 Reducing the feedthrough

Due to the fact that input resistance and capacitance coupling govern the characteristics of the feedthrough in this sensing scheme, in order to reduce the feedthrough at the high frequency region, either the input resistance of the differential amplifier or the capacitance between the PZT actuators and piezoresistors needs to be decreased. The large

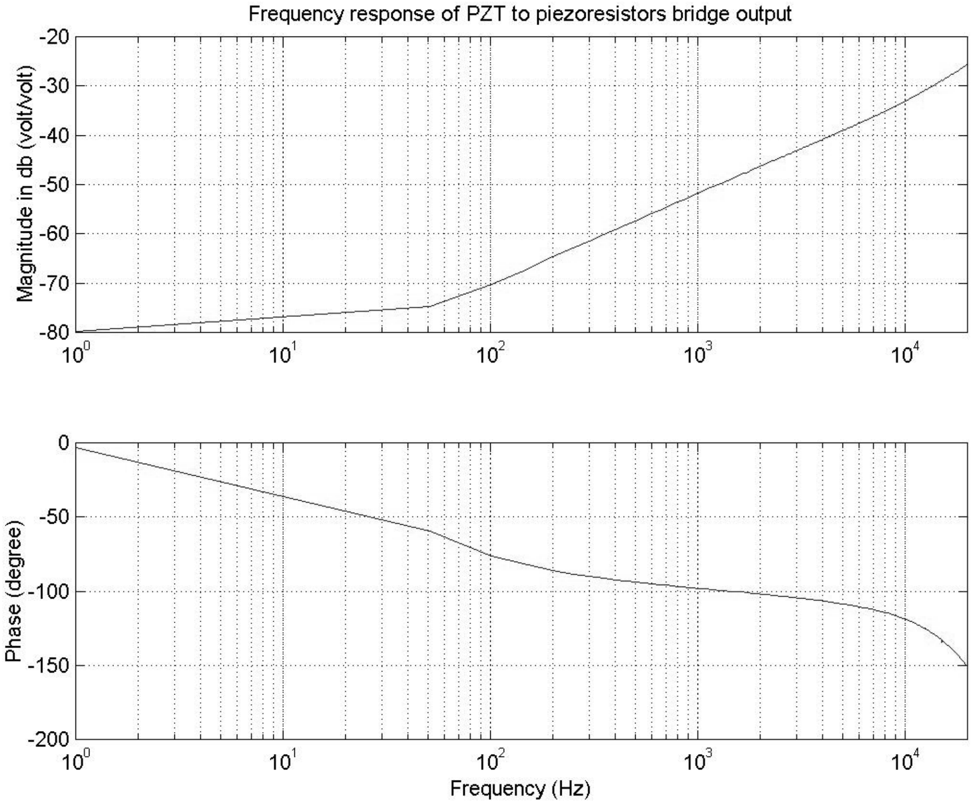

Figure 5.13: Feedthrough: from PZT to the output of the piezoresistors bridge

capacitance coupling is due to the thin isolation layer made of silicon nitride. To reduce the capacitance, without altering significantly the fabrication process, the thickness of the silicon nitride would need to be increased. However, silicon nitride is a very stressy material. Thus, increasing the thickness of the nitride film would result in a constant stretch imposed on the piezoresistive film.

On the other hand, reducing the input resistance of the differential amplifier, results in a decrease in the SNR (Signal-Noise-Ratio) of the piezoresistor sensor signal. This is due to the fact that the sensing signal from the piezoresistor sensor is attenuated by the low input resistance of the differential amplifier, while the noise of the differential amplifier, due to its electronic components, remains constant. This can be illustrated as follows:

In this piezoresistive-sensor sensing scheme, the 50 nm of sensing resolution was achieved by a voltage measurement of 0.1 mV at the output node of the piezoresistors bridge, while roughly 1 Volt was applied to the PZT actuators. This translates into a 80 dB difference between these two signals. To ensure the success of feedback control, the feedthrough from the PZT actuators to the piezoresistors sensor should stay less than –80 dB in a frequency range of up to 20 KHz. This specification requires that the corner frequency of the high pass filter, shown in Fig. 5.12, be moved from 500 Hz to 20 MHz, based on a 20 dB/decade slope. Assuming that the capacitance remains the same, this requires that the input resistance must be reduced 4×10^4 folds, to achieve the corner frequency at 20 MHz. That implies that the input resistance of the differential amplifier must be of 50 Ω or lower. In our piezoresistive sensors design, the output resistance of the piezoresistors bridge is about 150 KΩ. With the 50 Ω of the input resistance of the differential amplifier, the sensitivity 12.13 mV/ μm of the piezoresistor (data obtained in the previous section) would be greatly attenuated to 4 μV/ μm ($12.3 \times 50/(50 + 150 \times 10^3)$) at the input node of the differential amplifier. The input-noise-voltage-density of the differential amplifier is about 10 nV/$\sqrt{Hz}$ (the input noise of the operation amplifier OP07 from Analog Device). Given a required differential amplifier bandwidth of 30 KHz, this results in 1.7 μV of input noise. This input-voltage-noise can be converted into an equivalent displacement of 0.4 μm by the sensing sensitivity 4 μV/ μm. The resulting SNR is 2.5 (1 μm/0.4 μm) at the differential amplifier. To sum up the discussion, the 50 nm resolution at the output node of the piezoresistors bridge is seriously deteriorated to 0.4 μm at the differential amplifier.

5.4.4 Modulation scheme

The difficulty of reducing feedthrough has been discussed in the previous section. An alternative solution to the feedthrough problem is to apply a frequency modulation technique to this piezoresistors bridge. A simple frequency modulation scheme was successfully implemented with the silicon suspension. As shown in Fig. 5.14, PZT stretches the piezoresistor at the frequency w_2. Thus the change of resistance is varying at the same frequency w_2. Meanwhile, the piezoresistor bridge is biased at a voltage that has the frequency w_1. The formula for the piezoresistors bridge voltage output was extended from Eq. (3.5).

$$\begin{aligned} V_{out} &= \frac{(\delta R \cos w_2 t)}{2R}(V_{bias} \cos w_1 t) \\ &= \frac{\delta R}{R} V_{bias} \left(\cos(w_1 + w_2)t + \cos(w_1 - w_2)t\right) \end{aligned}$$

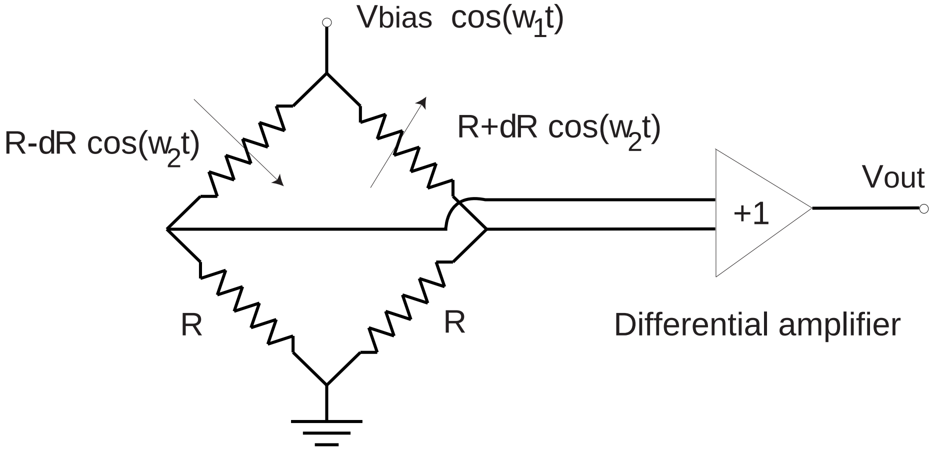

Figure 5.14: Modulation scheme for the piezoresistors bridge sensing

In this experiment, the PZT driving voltage is a sinusoidal with an amplitude of

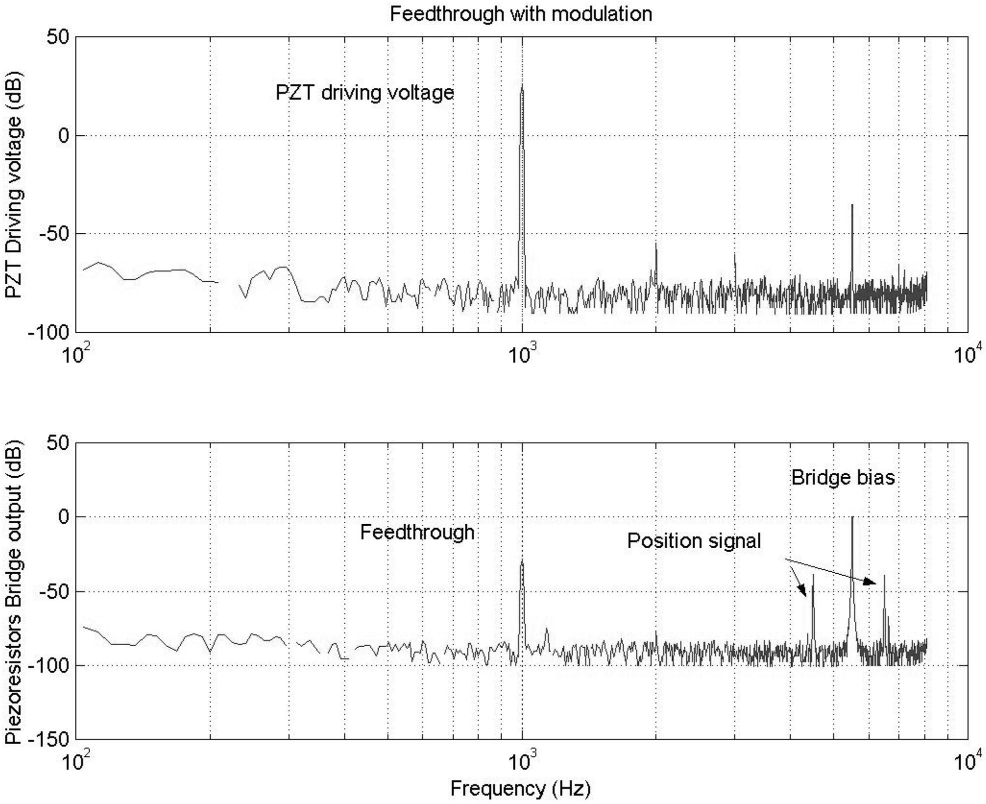

Figure 5.15: Modulation for the piezoresistors sensing bridge

20 Volts and a frequency of 1 KHz (w_2 in the equation), while the bias voltage for the piezoresistors bridge has an amplitude of 10 Volts and a frequency of 5.5 KHz (w_1 in the equation). The resulting experimental results are shown in Fig. 5.15. The upper plot is the voltage measured at the PZT strips and the lower plot is the voltage measured at the output node of the piezoresistors bridge. The position signal of the PZT displacement, produced by the piezoresistors bridge, appeared both at 4.5 KHz and 6.5 KHz frequencies. Although the magnitude of the feedthrough is still larger than the position signal, the feedthrough takes place at 1 KHz, and has been successfully separated from the position signal.

5.5 Electrical Interconnects Transmission Time

As discussed in Section 3.5, the electrical interconnects of the proposed silicon suspension were implemented by in-situ copper deposition and subsequently patterned into four metal leads, which start from the center coupon of the gimbal structure, passing through the gimbal's torsion bars and suspension's hinge structure, and end close to the base of the suspension. The resistance of the four metal leads were measured to be, $21\Omega/16\Omega/16\Omega/21\Omega$, respectively. These resistance were 4 times higher than their expected designed value. The major reasons that cause the resistance to be higher than expected are: (1) The thickness of the copper film was only 1/3 of the designed value. (2) The resistivity of the deposited thin film was two times higher than the value of bulk copper. Both of these deficiencies can be corrected with minor modifications in the fabrication process.

In order to predict the transmission time for these electrical interconnects, the parameters, shown in Fig. 3.19 of Section 3.5, need to be determined. The capacitance between metal leads and the silicon suspension (as CLS in Fig.3.19 in Section 3.5) was measured with a multi-meter. It's value was 50 pF, which is close to the estimated value of 45 pF. The capacitance between the two metal leads and the equivalent inductance can not be measured directly with a multi-meter. Instead, they were obtained by a supplemental experiment. In this experiment, an input voltage was applied across one line and an output voltage was measured at the two terminals of the other line. Fig. 5.16 shows the testing setup and the simplified equivalent circuit diagram.

Measurement were taken in the frequency range between 100 KHz to 30 MHz, and the results are shown in Fig. 5.17. The frequency response contains multiple resonances and it is believed that the irregularity of the interconnect layout contributes to most of this

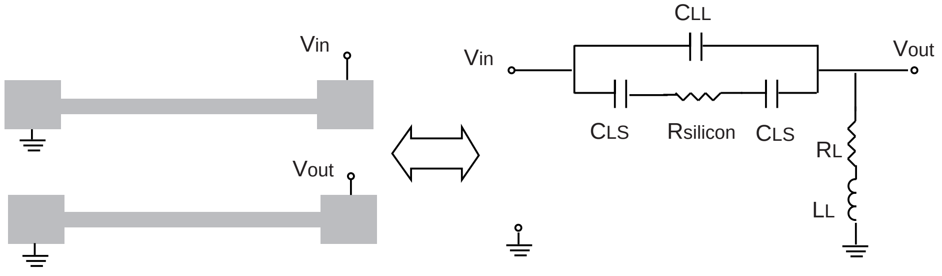

Figure 5.16: Schematic of cross-talk testing

effect.

To find out the equivalent capacitance and inductance, the transfer function from V_{in} to V_{out} in Fig. 5.16 was derived.

$$\frac{V_{out}}{V_{in}} = \frac{s(s+\frac{R_L}{L_L})(s+\frac{2}{R_{sil}C_{LS}}+\frac{1}{R_{sil}C_{LL}})}{s^3+s^2(\frac{2}{R_{sil}C_{LS}}+\frac{1}{R_{sil}C_{LL}}+\frac{R_L}{L_L})+s(\frac{2R_L}{C_{LS}R_{sil}L_L}+\frac{R_L}{C_{LL}R_{sil}L_L}+\frac{1}{C_{LL}L_L})+\frac{2}{C_{LS}C_{LL}R_{sil}L_L}}$$

As discussed in the Section 3.5, $C_{LL} \geq C_{LS}/2$. Applying this relation between C_{LL} and C_{LS} and neglecting the less significant modes in the equation above, the transfer function can be greatly simplified as follows.

$$\frac{V_{out}}{V_{in}} = \frac{s(s+\frac{R_L}{L_L})}{s^2+s\frac{R_L}{L_L}+\frac{1}{L_L C_{LL}}}$$

To find out the equivalent inductance L_L and equivalent capacitance C_{LL}, the "zero" at 9 MHz, the "complex poles" at 10.5 MHz are utilized, and all the less significant resonance modes are ignored. The resonance mode (a "zero" in the transfer function) at 9 MHz is related to the R_L/L_L, while the resonance at 10.5 MHz is related to

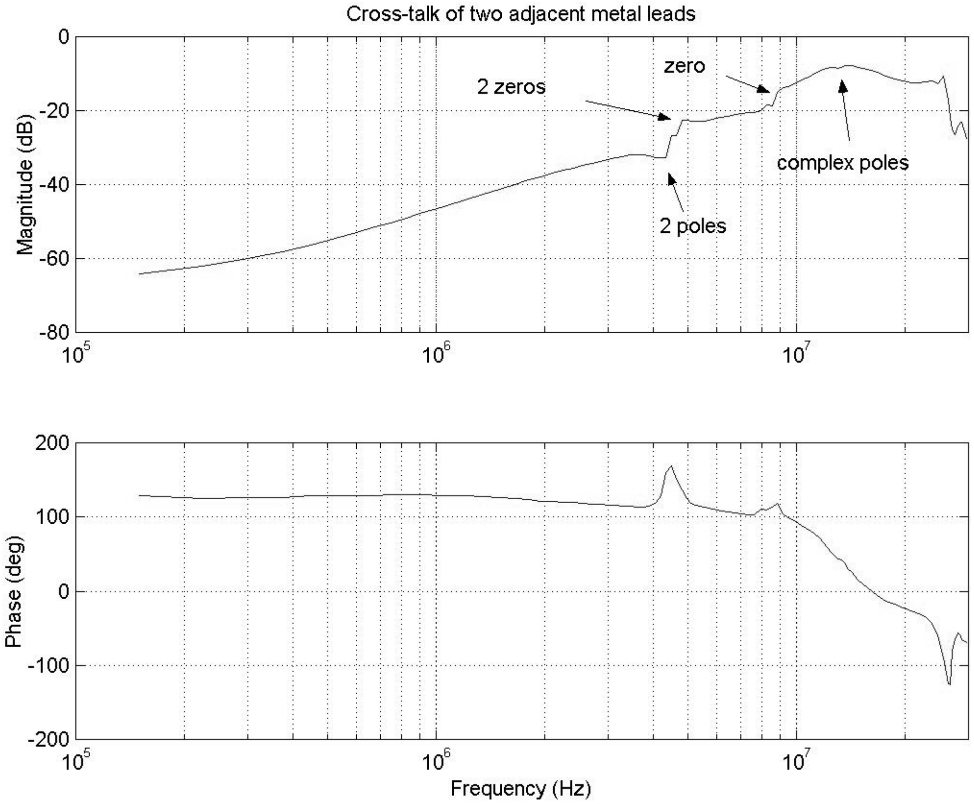

Figure 5.17: Frequency response of the cross-talk testing

$(1/(L_L C_{LL}))^{0.5}$. Therefore, the equivalent capacitance was found to be 370 pF, while the equivalent inductance was found to be 360 nH. The resulting time constant, obtained from $(LC)^{1/2}$, is 11 ns. This value is larger than the transition time (2.15 ns) of the MR head.

The $(LC)^{1/2}$ constant of the electrical interconnects on the proposed silicon suspension is obviously too high and will be the limiting factor on the data transmission rate. An immediate task to solve this problem should be a new process development that can reduce the capacitance coupling between wires.

Chapter 6

Conclusions

A one-piece silicon suspension was designed, fabricated and tested, which can be flexed by piezoelectric PZT strips and used as a second-stage actuator in a dual-stage servo system. The PZT actuation was able to drive the magnetic head +/- 1.3 μm with +/- 30 Volts applied on the PZT strips. The first significant structural resonant mode for PZT actuation was observed to be at about 6.85 KHz and the second resonance was at 9.9 KHz. The first resonance was due to suspension torsional mode, while the second resonance was due to suspension sway mode.

The technical contributions of this dissertation may be subdivided into three areas: the design of silicon suspensions, the formulation of analytical solutions for analyzing the torsional stiffness of a rectangular bar and the development of a new microfabrication process. The work accomplished on each topic is described below.

6.1 Silicon suspension design

Among three configurations (Actuated suspensions, Actuated sliders and Actuated heads) of integrating secondary actuation in magnetic HDDs, the PZT-actuated suspension is expected to be the first scheme to be deployed in commercial HDDs. As mentioned in the Chapter 1, the major drawback of this approach is that the system is still susceptible to instabilities due to the excitation of suspension resonance modes, and this may limit the performance of the dual-stage servo system. The proposed silicon suspension design presented in this dissertation incorporates an in-situ deposited piezoresistive film which can be utilized as an RPES sensor, to improve servo performance. The deposited piezoresistive film may also be utilized for sensing suspension vibration excited by air flow in the HDD system, which can be used for subsequent feedforward, or active damping compensation.

The implemented piezoresistive RPES sensing scheme has a fairly linear response and a high sensitivity. However, a large feedthrough from driving signal to sensing signal has been observed. The feedthrough has the nature of a high pass filter with the corner frequency at about 500 Hz. This corner frequency is determined by the input resistance of the sensing circuitry, as well as the capacitance developed from the isolation layer (silicon nitride) in the silicon suspension. It is difficult to reduce the resistance–capacitance coupling without significantly changing the current silicon-suspension fabrication process. A solution to the feedthrough problem is to apply a frequency modulation technique to the sensing scheme. The feasibility of frequency modulation was demonstrated by experimental data.

Current steel suspension assembly in the HDD use two pieces of steel (one for the suspension and one for gimbal structure) to meet dynamic performance requirements. A high performance disk drive system requires extremely tight dimensions for the gimbal structure, and a precise assembly of the gimbal structure on the suspension. As the dimensions of suspension keep scaling down, it becomes more and more challenging to achieve these requirements. In the proposed silicon suspension design, we were able to fabricate a gimbal structure with very precise dimensions, and to integrate this structure with suspension in one piece of silicon. The performance of the suspension assembly was ensured by its precise dimensions and the minimized assembly work. However, as mentioned in Chapter 3, the main challenge of an integrated gimbal design is the soft in-plane and out-of-plane stiffnesses due to very limited design parameter space. The proposed double-flexure torsion bars design was proven useful in solving this problem.

6.2 Torsional stiffness: End plane non-warping

Rectangular bars have been widely used in MEMS devices to provide compliant torsional stiffness. In most of the applications, a rectangular bar is stretched in a way such that one of its end plane is twisted but not warped. This particular boundary condition could significantly increase the torsional stiffness of the bar, depending on the dimensions of the rectangular bar, and an unbearable computational error may result when one applies currently used formulas to calculate the torsional stiffness of a bar. In this dissertation, a new formula was derived for calculating the torsional stiffness of rectangular bars, which is significantly more accurate than prior formulas. As shown in FEM simulations, under extreme loading conditions, the torsional stiffness calculated by the new formula is 20 times more accurate than the formula published by Timoshenko in 1934. However, this new formula is much more complicated than Timoshenko's.

6.3 Fabrication process

Ever since silicon reactive ion etch processes, which are capable of fabricating three-dimensional high-aspect-ratio structures, became widely available, many new MEMS devices have been designed and fabricated, which were not feasible before. In this silicon suspension design, we were able to take advantage of the silicon DRIE process development to fabricate high aspect ratio structures such as, double-flexure torsion bars, hinge structures, etc., which are key components in the proposed silicon suspension design. Due to the unique mechanical properties of high-aspect-ratio structures, it can be expected that more and more MEMS devices will be designed based on these structural properties.

A simple and reliable process has been developed to fabricate this new silicon suspension. This newly developed process includes four major process steps, which successfully implemented features for the proposed silicon suspension design: (1) piezoresistive film deposition (with gauge factor of 30). (2) high-aspect-ratio structures micromachining (with structure aspect ratio of 20). (3) planarization (with post-DRIE lithography accuracy of 3 μm) (4) metallization (a copper thin film deposition). This process is similar to the process based on the use of SOI wafers, but does not require the use of expensive SOI wafers.

During the testing of the fabricated silicon suspension, we noticed that the resonance modes of the fabricated suspension are generally lower than the values predicted by finite element analysis. A further investigation showed that, for planar features (i.e., width and length) of structures, the discrepancy between the designed and fabricated values is generally within 1 μm, while it may be as high as 5 to 10 μ for the structures heights across wafer. The fabrication process presented in this dissertation uses KOH backside etch to release the structure , in order to avoid the use of costly SOI wafers. One major drawback of this approach is the difficulty in controlling the structure height, due to STS etch-rate uniformity problems and the KOH overetch. Therefore, this process may not be suitable for applications where a precise structure height is required.

Another important aspect of the proposed fabrication process is the post-DRIE lithography. In this process, we first used a LPCVD PSG deposition to reform the surface topography caused by deep-trench etches, into a new topography which is similar to the topography encountered during IC fabrication. Subsequently, we planarized the surface of a wafer by implementing a polymer sacrificial layer and an ”etch-back” process, which was a well established planarization technique for IC devices fabrication. Although we successfully demonstrated a 3 μm lithography precision on a surface that contained deep trenches with a trench aspect ratio of 20, many questions need to be answered to validate this planarization process such as the effect of the viscosity of the applied polymer on the resulting topography, and the further characterization of parameters in the spin-on process.

Bibliography

[1] Satya Arya, Yau-Shing Lee, Wei-Min Liu, Markus Staudenmann and Mike Hatchett. Piezo-Based Milliactuator on a Partially Etched Suspension. *IEEE Trans. on Magnetics.* **Vol. 37, No. 2**, pp 934–939, 2001.

[2] Takayuki Aoyama, Hiroko Tashiro and Kunihiro Suzuki. Diffusion of Boron, Phosphorus, Arsenic and Antimony in Thermally Grown Silicon Dioxide. *Journal of Electrochemical Society*, **Vol. 146, No. 5**, pp 1879–1883, 1999.

[3] Ferdinand P. Beer and E. Russell Johnston, JR. *Mechanics of Materials*, second edition, McGraw-Hill, 1992.

[4] M. Le Berre, P. Kleimann, B. Semmache, D. Barbier, P. Pinard. Electrical and Piezoresistive Characterization of Boron-doped LPCVD Polycrystalline Silicon under Rapid Thermal Annealing. *Sensors and Actuators A.* **Vol. 54**, pp 700–703, 1996.

[5] K. N. Bhat, M. C. Ramesh, P. R. S. Rao and B. Ganesh. Polysilicon Technology. *IETE Journal of Research*, **Vol. 43, Nos 2 / 3**, March–June, pp 143–154, 1997

[6] A. D. Buonaquisti, W. Carter and P. H. Holloway. Diffusion Characteristics of Boron

and Phosphorus in Polycrystalline Silicon. *Thin Solid Film.* **Vol. 100**, pp 235–248, 1983.

[7] Min Cao, Paul Vande Voorde, Mike Cox and Wayne Greene. Boron Diffuision and Penetration in Ultrathin Oxide with Poly-Si Gate. *IEEE Electron Letters*,**Vol. 19, No. 8**, pp 291–293, 1998.

[8] Cheung, P., Horowitz, R. and Howe, R. Design, Fabrication, Position Sensing and Control of an Electrostatically-driven Polysilicon Microactuator. *IEEE Transactions on Magnetics*,**Vol. 32, No. 1**, pp 122–128, 1996

[9] Samir Chaudhry and Mark E. Law. The Stress Assisted Evolution of Point and Extend Defects in Silicon. *J. Appl. Phys*,**Vol. 82, No. 3**, pp 1138–1146, 1997.

[10] R. B. Evans, J. S. Griesbach and W. C. Messner. Piezoelectric Microactuator for Dual Stage Control. *IEEE Trans. on Magnetics*, **Vol. 35 No. 2**, pp 977–982, 1999.

[11] Richard B. Fair. Modeling Boron Diffuision in Ultrathin Nitride Oxide P+ Si Gate Techonogy. *IEEE Electron Device Letters*, **Vol. 18 No. 6**, pp 244–247, 1997.

[12] L. S. Fan, H. H. Ottesen, T. C. Reiley and Roger W. Wood. Magnetic Recording Head Positioning at Very High Track Densities Using a Microactuator-based Two-stage Servo System. *IEEE Trans. on Industrial Electronics*, **Vol, 42, No. 3**, pp 222–233, 1995.

[13] P. J. French and A. G. R. Evens. Piezoresistance In Polysilicon and its Applications to Strain Gauges. *Solid-State Electronics*, **Vol, 32, No. 1**, pp 1–10, 1989

[14] David Horsley, Ph.D. Dissertation, University of California at Berkeley, pp. 66-85, 1998.

[15] T. Howell, R. Ehrlick and M. Lippman. TPI Growth is Key to Delaying Superparamagnetism's Arrical. *Data Storage Magazine*, pp 21–30, September, 1999.

[16] Paul Horowitz, Winfield Hill. *The Art of Electronics*, second edition, Cambridge, 1989.

[17] A. M. Hynes, H. Ashraf, J. K. Bhardwaj, J. Hopkins, I. Johnston and J. H. Stepherd. Recent Advances in Silicon Etching for MEMS Using the ASE^{TM} Process. *Sensors and Actuators*, **Vol, 74**, pp 13–17, 1999.

[18] S. M. Hu. Critical Stress in Silicon Brittle Fracture, and Effect of Ion Implantation and other Surface Treatments. *J. Appl. Phys.*, **Vol, 53, No 5**, pp 3576–3580, 1982

[19] Takahiro Imamura, Takao Koshikawa and Masaki Katayama. Transverse Mode Electrostatic Microactuator For MEM-Based HDD Slider. *Proc. IEEE MEMS Workshop*, pp 216–221, 1996

[20] Takahiro Imamura, Masaki Katayama, Yukinori Ikegawa, Takeshi Ohwe, Ryosuke Koishi and Takao Koshikawa. MEMS-Based Integrated Head/Actuator/Slider for Hard Disk Drives. *IEEE/ASME Trans. on mechatronics*, **Vol, 3, No 3**, pp 166–174, 1998

[21] Richard C. Jaeger. *Introduction to microelectronic fabrication*, second edition, Addison-Wesley, 1988.

[22] John D. Leighton, Sally Doherty and Carl Elliott. Design Considerations for Hight Data-Rate Pre-Amplifiers for Use in a Disk-Drive. *IEEE Transactions on Magnetics*, **Vol. 37, No. 2**, pp 627–632, March, 2001.

[23] Christopher Guild Keller. Ph.D. Dissertation, University of California at Berkeley, Spring 1998.

[24] P. Kleimann, M. Le Berre, D. Barbier, P. Pinard. Application of Rapid Thermal Annealing on LPCVD Polysilicon Films for Piezoresistivity. *Mat. Res. Soc. Symp. Proc.*, **Vol. 403**, pp 399–404, 1996.

[25] P. Kleimann, B. Semmache, M. Le Berre, D. Barbier. Influence of the Structural Parameteres of Polysilicon Films on the Piezoresistive Properties at High Temperature. *Mat. Res. Soc. Symp. Proc.*, **Vol. 444**, pp 131–136, 1997.

[26] Klass B. Klaassen and Richard G. Hirko. Writing and Reading at High Data Rate. *IEEE Transactions on Megnetics*, **Vol. 32, No. 1**, pp 90–96, 1996.

[27] Shinji Koganezawa, Kazuhiko Takaishi, Yoshifunmi Mizoshita, Yukihiro Uematsu and Tomoyoshi Yamada. Development of Integrated Piggyback Milli-Actuator for High Density Magnetic Recording. *International Conference on Micromechatronics for Information and Precision Equipment.* Tokyo, July, pp 20–23, 1997

[28] Karl Kuhl, Stefan Vogel, Ulrich Schaber, Rainer Schafflik and Bernd Hillerich. Advanced Silicon Trench Etching in MEMS Applications. *SPIE Conference on Micromachining and Microfabrication Process.* **Vol. 3511**, pp 97–105, 1998

[29] Chris Seung-Bok Lee, Sejin Han and Noel C. MacDonald. Multiple Depth, Single Crystal Silicon Microactuators For Large Displacement Fabricated by Deep Reative Ion Etching. *Solid State Senosrs and Actuators Workshop.* June, 1998. Hilton Head, South Carolina, USA.

[30] Ming-Kwei Lee, Ching-Nan Yang and Ching-Hsing Lin. Conformal Step Coverage and Trench Filling of Liquid Phase Oxide Deposition. *J. Appl. Phys.*, **Vol. 38**, pp 5048–5049, 1999.

[31] Yungfeng Li and Roberto Horowitz. Track-Following Controller Design of MEMS Based Dual-Stage Servos in Magnetic Hard Disk Drives. *International Conference on Robotics and Automations*. April, 2000. San Francisco, USA.

[32] Lorna J., Gibson (1988). Cellular Solids. pp 114–115. Oxford, New York: Pergamon Press.

[33] Paul Lorrain, Dale R. Corson and Francois Lorrain. Electromagnetic Fields and Waves. 3rd edition, W. H. Freeman and Company, New York. 1988.

[34] M. Mallary. Magnetic Recording Technology for 10 Gb/sq" and beyond. *Proceedings of the Fifth International Symposium on Magnetic Materials, Processes, and Devices Applications to Storage and Microelectromechanical Systems (MEMS)*. pp 19–32, 1998.

[35] Denny K. Miu and Yu-Chong Tai. Silicon Micromachined SCALED Technology. *IEEE Trans. on Industrial Electronics*. **Vol. 42, No. 3**, pp 234–239, 1995.

[36] K. Mori, T. Munemoto, H. Otsuki, Y. Yamaguchi, K. Akagi. A Dual-Stage Magnetic Disk Drive Actuator Using a Piezoelectric Device for a High Track Density. *IEEE Trans. on Magnetics*. **Vol. 27, No. 6**, pp 5298–5300, 1991.

[37] Muller, L., Heck, J. M., Howe, R. T. and Pisano, A. P. (2000). Electrical Isolation Process For Molded, High Aspect Ratio Polysilicon Microstructures. *Proceedings of IEEE Workshop on Micro Electro Mechanical Systems (MEMS2000)*, pp 590–595.

[38] Lilac Muller, Ph.D. Dissertation, University of California at Berkeley, Spring 2000.

[39] Richard S. Muller and Theodore I. Kamins. *Device Electrionics for Integrated Circuits*, second edition, John Wiley & Sons, 1986.

[40] S. Nakamura, K. Suzuki, M. Ataka and H. Fujita. An Electrostatic Micro Actuator for a Magnetic Head Tracking System of Hard Disk Drives. *Transducers '97*, Chicago, June, pp 1081–1084, 1997.

[41] I. Naniwa, S. Nakamura, S. Saegusa and K. Sato. Low Voltage Driven Piggy-Back Actuator of Hard Disk Drives. *MEMS '99*, pp 49–52, 1999.

[42] M. Narbutovskih, L. Field, G. Clifford, D. Henze, D. Burriesci, J. Williams, P. Beck. A Silicon Microsuspension for Disk Drive Application. *TRANSDUCERS '97*, Chicago, pp 221–224, 1997.

[43] T. Nishimoto, S. Shoji and M. Esashi. Buried piezoresistive sensors by means of MeV Ion Implantation. *Sensors and Actuators.* **A, Vol. 43**, pp 249–253, 1994.

[44] T. Nishimoto, S. Shoji, K Minami and M. Esashi. Temperature Compensated Piezoresistor Fabricated by High Energy Ion Implantation. *IEEE Trans. Electron.*. **Vol. 78**, pp 152–155, 1995.

[45] Yimin Niu, Wei Guo, Guoxiao Guo, Eng Hong Ong, K. K. Sivadasan and Tony Huang. A PZT Micro-Actuated Suspension for High TPI Hard Disk Servo Systems. *IEEE Trans. on Magnetics.*. **Vol. 36, No. 5**, pp 2241–2243, 2001.

[46] E. Obermeier and Kopystynski. Polysilicon as a Material for Microsensor Applications. *Sensors and Actuators.* **A, Vol. 30**, pp 149–155, 1992.

[47] T. Ohwe, T. Watanabe, S. Yoneoka and Y. Mizoshita. A New Integrated Suspension for Pico-Sliders (PICO-CAPS). *IEEE Transactions on Megnetics*, **Vol. 32, No. 5**, pp 3648–3650, 1996.

[48] T. Ohwe, T. Watanabe, and S. Yoneoka. An Investigation of Wireless Suspensions. *IEEE Transactions on Megnetics*, **Vol. 34, No. 4**, pp 1759–1761, 1998.

[49] Kurt E. Petersen. Silicon as a Mechanical Material. *Proceedings of the IEEE*, **Vol. 70, No. 5**, pp 420–457.

[50] G. L. Peason, W. T. Read and W. L. Feldmann. Deformation and Fracture of Small Silion Crystals. *ACTA METALLURGICA*, **Vol. 5**, April, pp 181–191.

[51] V.V.R. Narasimha Rao, S. Mohan and P. Jayarama Reddy. Electrical Resistivity, TCR and Thermoelectric Power of Annealed Thin Copper Films. *J. Phys. D: Appl., Phys.*, **Vol. 9**, pp 89–94, 1976.

[52] Roberto Oboe, A. B. and Murari, B. (1999). Modelling and Control of a dual stage actuator hard disk drive with piezoelectric secondary actuator. *International Conference on Advanced Intelligent Mechatronics*, September, Atlanta, USA, pp 138–143.

[53] H. Seidel, L. Csepregi, A. Heuberger, H. Baumgartel. Anisotropic Etching of Crystalline Silicon in Alkaline Soultions. *J. Electrochem. Soc.*, **Vol. 137, No. 11**, November, pp 3612–3626, 1990

[54] Darrell L. Simpson, Robert T. Croswell, Arnold Reisman, Dorota Temple and C. Kenneth Williams. Planarization Processes and Applications. *Jounral of The Electrochemical Society*, **Vol. 146, No. 10**, pp 3860–3871, 1999.

[55] Kevin A. Shaw, Z. Lisa Liang and Noel C. MacDonald. SCREAM I: A Single Mask, Single Crystal Silicon, Reactive Ion Etching Process for Microelectromechanical Structures. *Sensors and Actuators*, **A40**, pp 63–70, 1994.

[56] Chee Burn Shin and Gyeong Soon Hwang. A Main Facotr Determining the Uniform Step Coverage in Chemical Vapor Deposition. *Mat. Res. Soc. Symp. Proc.*, **Vol. 514**, pp 369–374, 1998

[57] Masashi Shiraishi. Chip on Suspension MR Head. *IEMT/IMC Proceedings*, pp 333–336, 1998.

[58] Vincent L. Spiering, J. W. Berenschot, Miko Elwenspoek and Jan H. J. Fluitman. Sacrificial Wafer Bonding for Planarization After Very Deep Etching. *Journal of Microelectromechanical Systems.*, **Vol. 4, No. 3**, pp 151–157, 1995

[59] S. Timoshenko, *Theory of Elasticity*, 2nd edition, McGRAW-HILL, 1934.

[60] S. Timoshenko, *The Collected Papers of STEPHEN P. TIMOSHENKO*, McGRAW-HILL, 1953.

[61] C. Y. Ting, V. J. Vivalda and H. G. Schaefer.Study of Planarized Sputter-Deposited SiO_2. *Journal of Vacuum Science and Technology*, **Vol. 40, No. 3**, pp 1105–1112, 1978.

[62] Takaishi, K., Imamura, T. Mizoshita, Y., Hasegawa, S., Ueno, T. and Yamada, T. (1996). Microactuator Control For Disk Drive. *IEEE Transaction on Magnetics*, **Vol. 32, No. 3**, pp 1863–1866.

[63] Kenji Uchino, *Piezoelectric actuators and ultrasonic motors*, Boston: Kluwer Acadmic Publishers, 1997.

[64] Shuyun Wu, Viktoria Temesvary, Yu-Chong Tai and D. K. Miu. Silicon micromachined

integrated suspension systems for magnetic disk drives. *Sensors and Actuators*, **A55**, pp 195–200.

[65] W. L. Wang, X. Jiang, K. Taube and C. P. Klages. Piezoresistivity of Polycrystalline p-Type Diamond Films of Various Doping Levels at Different Temperatures. *J. Appl. Phys.*, **Vol. 82, No. 2**, pp 729–732, 1997.

[66] J. S. Williams. Ion implantation of semiconductors. *Materials Science and Engineering*, **A253**, pp 8–15, 1998.

[67] G. W. Wilson and B. P. Sinha. The effect of Absorbed Argon on the Eelectrical Properties of Thin Copper Films. *Thin Solid Films*, **Vol. 8**, pp 207–211, 1971.

[68] Roger Wood, Mason Williams and John Hong. Considerations for High Data Rate Recording with Thin Film Heads. *IEEE Transactions on Magnetics*, **Vol. 26, No. 6**, pp 2954–2959, 1990.

[69] W Xu and T. G. King. Mechanical Amplifier Design for Piezo-actuator Applications. *The intstitution of Electrical Engineers*, pp 1–5, 1995.

[70] Jun-Bo Yoon, Gilbert Y. Oh, Chul-Hi Han, Euisik Yoon and Choong-KI Kim. Planarization and trench filling on severe surface topography with thick photoresist for MEMS. *SPIE conference on Micromachining and Microfabrication Process Technology IV*, **Vol. 3511**, pp 297–306, 1998.

[71] Warren C. Young, *Roark's Formulas for Stress and Strain*, 6th edition, McGRAW-HILL, 1989.

[72] W. Zhu, K. Yao and Z. Zhang. Design and Fabrication of a Novel Piezoelectric Multiplayer Actuator by Thick-Film Screen Printing Technology. *Sensors and Actuators*, **Vol. 86**, pp 149–153, 2000

Appendix A

Torsion Stiffness for Double-Flexured Structure

In this appendix, the calculation for the torsion stiffness of the structure that has two adjacent rectangular bars for torsional motion is presented. The result of this derivation is applied to the integrated gimbal design. A simplified schematic of this structure is shown in Fig. A.1. The structure has a middle block and 2 rectangular bars on each side. The middle block is assumed to have a Young's modulus which is 1000 times higher than that of the rectangular bars on each side. Therefore, its deformation can be neglected in the computation of the stiffness of the overall structure.

Due to the symmetry of the structure, the analysis is conducted on 1/2 of the structure. When the overall structure is subjected to a torsional motion, the two rectangular bars, on the left to the middle block, twist with an angle θ and move along Y and Z direction. This motion is exaggeratedly depicted in the "a-a cross section" in the Fig. A.1. The motion consists of bending in Y direction, bending in Z direction and torsion in X

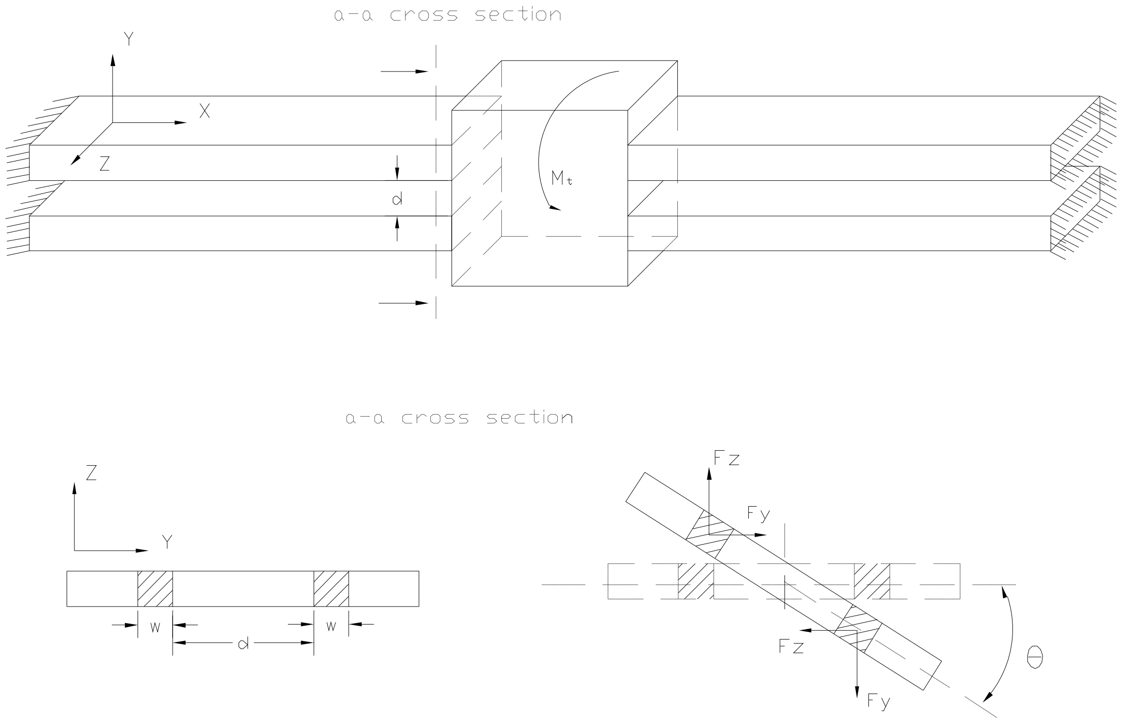

Figure A.1: The schematic of double-flexure torsion bar structure

direction. Assuming that the angle θ is small, this composite motion can be analyzed by the superposition of the individual motions.

For the bending motion in Z-direction,

$$F_z = K_z \frac{d+w}{2} \sin\theta$$

$$\begin{aligned} M_{tz} &= 2F_z \frac{d+w}{2} \cos\theta \\ &= K_z \frac{(d+w)^2}{2} \sin\theta \cos\theta \end{aligned} \tag{A.1}$$

An analogous result can be drawn for the bending in Y-direction,

$$F_y = K_y \frac{d+w}{2} \sin\theta \tan\theta$$

$$\begin{aligned} M_{ty} &= 2F_y \frac{d+w}{2} \sin\theta \\ &= K_y \frac{(d+w)^2}{2} \sin^2\theta \tan\theta \end{aligned} \tag{A.2}$$

For each rectangular bar subjected to a torsion along X-direction, we obtain

$$M_{tr} = K_{tr}\theta \tag{A.3}$$

where

M_{tz}	Moment due to F_z
M_{ty}	Moment due to F_y
M_{tr}	Moment due to rotation of each rectangular bar
K_z	Bending stiffness along Z-direction for one rectangular bar
K_y	Bending stiffness along Y-direction for one rectangular bar
K_{tr}	Rotating stiffness of a rectangular bar
d	Gap between two adjacent bars
w	Width of the rectangular bar
θ	Rotation angle of the overall structure

Based on the small angle assumption, we let $\sin\theta \simeq \theta$ and $\cos\theta \simeq 1$ in Eq. (A.1) and Eq. (A.2). M_t is the torque that is apply to the whole structure.

$$\begin{aligned} M_t &= 2\left(2M_{tr} + M_{tz} + M_{ty}\right) \\ &= 2\left(2K_{tr}\theta + K_z \tfrac{(d+w)^2}{2}\theta + K_y \tfrac{(d+w)^2}{2}\theta^3\right) \end{aligned}$$

Without losing much accuracy, it is possible to ignore the high order terms of θ. Therefore, we can estimate the overall torsional stiffness K_t for the whole structure to be,

$$\begin{aligned} K_t &= \frac{M_t}{\theta} \\ &= 4K_{tr} + K_z(d+w)^2 \end{aligned} \tag{A.4}$$

Due to the symmetry of the overall structure, the rectangular bar curves in a way to make its gradient at the junction with the middle block equal to zero. Moreover, it rotates in a way that its end plane twists but not warps. The expression for the bending stiffness can be obtained from Section 2.1 in Chapter 2. The expression for the torsion stiffness can be obtained from Eq. (2.24). For convenience, we listed these expressions here.

$$K_z = \frac{Ehw^3}{l(l^2 + 3(1+\nu)w^2)}$$

$$K_{tr} = \frac{1}{3}G\theta^2(2a)(2b)^3(1-\sqrt{\frac{2}{5}\frac{b}{a}})\left[l - a^2\left(\frac{8}{15} - \frac{1}{6(1-\sqrt{\frac{2}{5}\frac{b}{a}})}\right)\sqrt{\frac{(1+\nu)(5-16\frac{b^2}{a^2})(1-\sqrt{\frac{2}{5}\frac{b}{a}})}{a^2+b^2}}\right]^{-1}$$

where

E	Young's modulus
G	Shear modulus
ν	Poisson's ratio
a	1/2 of the height of the rectangular bar
b	1/2 of the width of the rectangular bar
l	Length of the rectangular bar